

## COMPARISON OF NUMERICALLY SIMULATED AND MEASURED DOSE RATES FOR GAMMA-IRRADIATION FACILITY †

 Volodymyr Morgunov<sup>a\*</sup>, Imre Madar<sup>b</sup>,  Serhii Lytovchenko<sup>a</sup>,  
 Volodymyr Chyshkala<sup>a</sup>,  Bohdan Mazilin<sup>a</sup>

<sup>a</sup>V.N. Karazin Kharkiv National University, 4 Svobody Sq., Kharkiv, 61022, Ukraine

<sup>b</sup>Institute of Isotopes CO. LTD., Konkoly-Thege Mikl'os 'ut 29-33., 1121 Budapest, Hungary

\*Corresponding Author: [v.morgunov@karazin.ua](mailto:v.morgunov@karazin.ua)

Received March 7, 2022; revised March 21, 2022; accepted April 22, 2022

The article provides a description of steps which were made to make comparison between numerically simulated and measured dose rates in Izotop gamma-irradiation facility (Budapest, Hungary) Numerical simulation was carried out with the help of software toolkit GEANT4. Dose measurement were made by ethanol-chlorobenzene (ECB) dosimeters. The comparison shows a good agreement between simulated and measured values. Worst accuracy was 17.08%.

**Keywords:** absorbed dose, dose rate, numerical simulation, ECB.

**PACS:** 06.20.-f; 29.40.Vj; 29.40.Wk

Radiation treatment are widely used for decision of big number of tasks which are important for the human life:

- sterilisation of medical goods and devices [1];
- food hygienization [2];
- flue gas purification from gaseous pollutants [3];
- sewage and sludge clean up [4];
- wire and plastic treatment [5];
- cultural heritage disinfestation, preservation and conservation [6];
- and many others.

Measurement of absorbed doses and dose rates is an important and indispensable task in radiation processing operations. The absorbed dose and dose rates are the main criteria for assessing the degree of radiation processing of materials [7].

This article provides a sequence of actions which were made to compare the numerically simulated and measured dose rates values.

### DESCRIPTION OF THE NUMERICAL SIMULATION

In the course of this work, we used software toolkit GEANT4, a toolkit for the simulation of the passage of particles through matter. Its areas of application include high energy, nuclear and accelerator physics, as well as studies in medical and space science [8–10].

To use GEANT4 the following aspects should be defined:

- the geometry of the system;
- the materials involved;
- the fundamental particles of interest;
- the physical processes of interest;
- the generation of primary events;
- the response of sensitive detector components.

#### The geometry of the system

The geometry of the systems involves the dimensions of the objects and their location. The geometry of the system consists of the following items

- the maze and building of the gamma facilities;
- the <sup>60</sup>Co sources;
- the cover of the gamma sources;
- other constructional elements;
- dosimeters;
- conveyor system (if exists).

The above-mentioned items are shown on Fig. 1,2,3.

† **Cite as:** V. Morgunov, I. Madar, S. Lytovchenko, V. Chyshkala, and B. Mazilin, East Eur. J. Phys. 2, 118 (2022), <https://doi.org/10.26565/2312-4334-2022-2-15>.

© V. Morgunov, I. Madar, S. Lytovchenko, V. Chyshkala, B. Mazilin, 2022

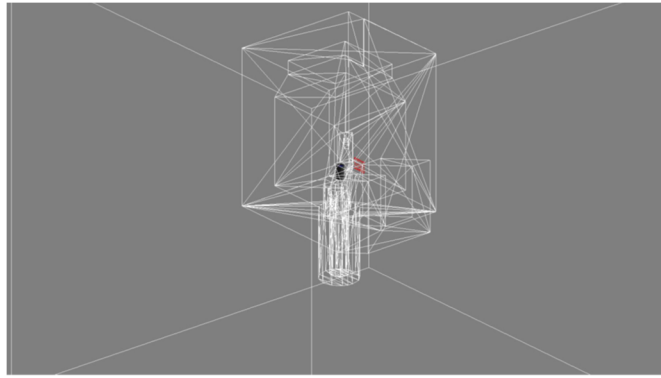


**Figure 1.** Building of gamma facility, Izotop (Budapest, Hungary)

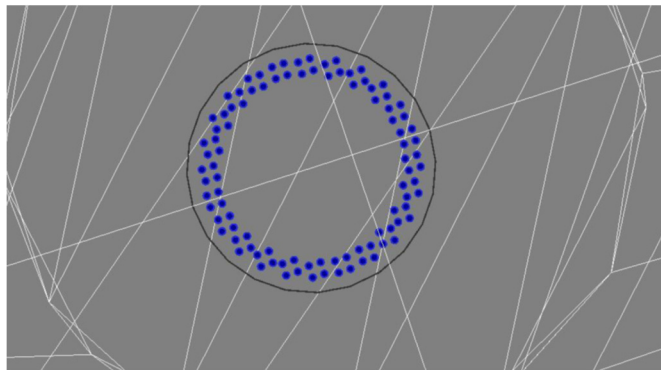


**Figure 2.** Gamma sources

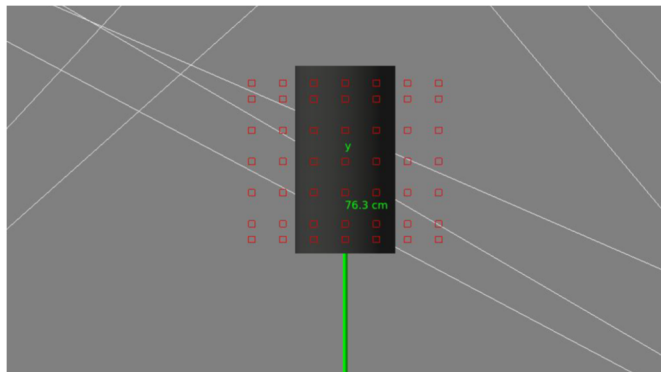


**Figure 3.** Array of dosimeters and cover of gamma sources

All geometrical objects are made as “.stl” files and were imported into simulations. Total view of facility geometry in simulation is given on Fig. 4.

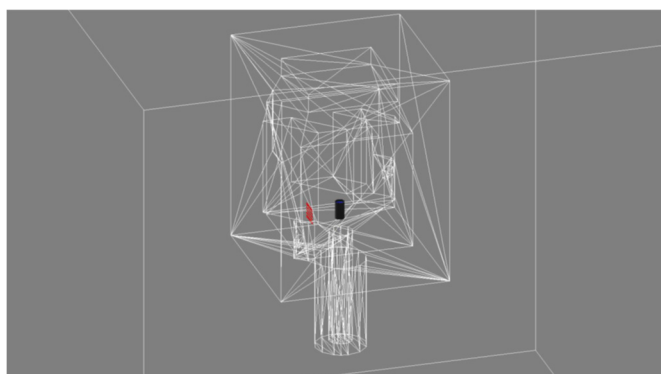


**Figure 4.** Total view of facility geometry in the simulation

### The materials involved

The following materials are involved into the simulation:

- concrete;
- stainless steel;
- water (materials of doisemters);
- air.

These materials are standards ones and their composition can be found GEANT4 table of materials.

### The fundamental particles of interest

According to the physical laws during gamma irradiation following elementary particles take part:

- gamma rays;
- X rays;
- electrons;
- positrons;
- anti-neutrinos.

Anti-neutrinos are not included into simulation because these particles can pass through the matter without any collisions with the matter.

### The physical processes of interest

Seven major categories of processes are provided by GEANT4:

1. electromagnetic;
2. hadronic;
3. decay;
4. photolepton-hadron;
5. optical;
6. parameterization;
7. transportation.

In the simulation, the 1st, 3d and 7th processes were chosen.

### The generation of primary events

Generation of initial gamma rays are generated from  $^{60}\text{Co}$  isotropically (i.e. uniformly in all orientations) and along gamma sources (so-called "pencil"). Built-in GEANT4 General Particle Source (GPS) class is used for this purpose.

Data concerning activity of the gamma sources can be read from .csv file (one of the Excel formats).

Developed code arrange these gamma sources properly (See Fig. 2).

Also, the decay of gamma sources are taken into the account in the simulation.

### The response of sensitive detector components

To record and output data from simulations, a process called "scoring", must be implemented, specifying what should be measured and where.

In the simulation array of dosimeters were used as shown on Fig. 3. The array of dosimeters consists of 49 dosimeters. All values of absorbed dose is referenced to the water.

## SHORT DESCRIPTION OF GAMMA IRRADIATION FACILITY

The gamma-facility has following characteristics and parameters [11]. The  $\gamma$ -irradiation facility (Institute Izotop Co, Budapest, Hungary) is a  $^{60}\text{Co}$  facility of SLL-01 type. The maximum amount of activity which can be loaded into the facility is 120 kCi.

The Co-60 gamma irradiator is a Category IV facility. It normally contains 20 Co-60 source capsules (so called torpedoes) each of them can be loaded with 4  $^{60}\text{Co}$  sources (type CoS-43 HH) of diameter 11 mm, height 451 mm, or other sources of the same size.

The Co-60 sources are stored in an underground water pool when not in use. The inner lining of the pool is made of 5-mm thick stainless steel. In storage position the radiation sources are kept (in fully shielded condition) in the source-cage. In this case there is 4.2-m water over the upper level of the sources, which gives adequate radiation protection in the direction of the irradiation chamber.

In order to reach the irradiation, position the torpedoes must be lifted from the storage position to the irradiation position. The sources in the cage are cylindrically arranged on a pitch-circle of 280-mm diameter.

The design of the tubes holding the sources allows after-loading of the sources. The torpedoes in the cage can be lifted up to irradiation position from the storage position by a hoist mechanism. In the irradiation position the symmetry level of the sources is 80 cm over the floor of the irradiation room.

The size of the irradiation chamber is  $4 \times 4 \times 4$  m; it is surrounded by walls made of 1.7 m normal concrete. Safe entrance to the irradiation chamber is ensured by a shielded maze with several turnings (breaks). The entrance door of the maze is made of steel. Access of personnel and transport of products are controlled by safety rules and technology to

prevent accidental exposure of personnel or visitors. The irradiation process can be monitored from the control desk in the control room adjacent to the irradiation chamber. The irradiator is operated fully automatically, controlled by an electronic control unit. Irradiation during daytime-operation is performed in the presence of operators by manual or automatic control.

The radiation sources can be lifted to the irradiation position as required by the experimental or pilot-plant radiation treatment. The number of sources appropriate for the program can be manually chosen; the time required for irradiation can automatically be ensured. The goods, to be irradiated, can be placed either in the cylinder of 215-mm dia located in the middle of the cage irradiation position (inner irradiation field), or around the source-cage in the irradiation room (outer irradiation field).



Figure 5. Co-60 Gamma Irradiation Chamber

The distance of the horizontal plane of symmetry of the sources from the floor is 80 cm. This height makes it possible for regular pilot-scale radiation treatment of products placed in  $40 \times 60 \times 75$ -cm boxes and also at larger distances from the sources. The radiation treatment of various products placed in aluminium containers ( $80 \times 60 \times 130$  cm) of  $0.5 \text{ m}^3$  volume can be carried out as well. In the space near the cage radiation treatment can be performed in small size e.g.  $40 \times 40 \times 35$ -cm boxes (see the Fig 5).

The high dose intensity space within the cage can be regularly used for the radiation treatment of max. 9 litre samples ( $\varnothing 1180 \times 360$ ). Owing to the relatively large volume of the irradiation chamber, up to 1.6 m height of the useful radiation field, products can be irradiated at very wide dose rates.

The irradiator is equipped with devices for water purification and exhaust air filters. The goods to be irradiated - before and after treatment - are transported into and out of the irradiation chamber through the maze manually or with the help of carriages made for this purpose.

## RESULTS OF CALCULATION AND COMPARISON WITH ABSORBED DOSE MEASUREMENTS IN SITU

The dose measurements were performed by the ECB dosimeters according to "Practice for use of the ethanol-chlorobenzene dosimetry system" [12].

The dosimetry system at Institute of Izotop can be described as follows [11]. The ethanol-chlorobenzene dosimeter uses the hydrochloric acid formation. Dose range: 0.1 kGy – 1 MGy. The ethanol-chlorobenzene dosimeter (ECB) has got wide-spread application in gamma radiation processing and at (linear) electron accelerators. Its reliable performance was proved in a number of international and bilateral intercomparison programs, including the IAEA and several National Institutes of Standards. The method is in routine use in more than twenty countries.

The basic radiation chemical process, used for dosimetry, is the formation of HCl upon irradiation. Its concentration is a linear function of the dose absorbed in the solution in a wide dose range of 0.1 – 100 kGy. At higher doses the reactions become more complicated.

The absorbed dose is determined by measuring the concentration of HCl(cHCl) formed during irradiation. Oscillometric titration is the most frequently used method. The irradiated dosimeter can be re-evaluated many times [13,14].

Calculations were performed on personal computer equipped with AMD Ryzen™9 3900xt (24 threads, 12 cores) processor, 48 GB RAM.

Amount of simulated events was  $10^9$ . Calculation time was approximately about 72 hours. The results of absorbed dose rate measurement in situ, numerical calculations, and their comparison is given in the Tables 1, 2, 3 for distance 570, 820, 1700 mm from the center of  $\gamma$ -sources respectively.

**Table 1.** Absorbed dose measurement in situ, numerical calculations, and their comparison. Distance from the source – 570 mm

Distance Z, mm	Dose rates, kGy/h																				
	Y, mm																				
	-300			-200			-100			0			100			200			300		
	M	C	C <sub>m</sub>	M	C	C <sub>m</sub>	M	C	C <sub>m</sub>	M	C	C <sub>m</sub>	M	C	C <sub>m</sub>	M	C	C <sub>m</sub>	M	C	C <sub>m</sub>
250	1.08	0.99	8.31	1.16	1.05	9.09	1.24	1.17	6.08	1.27	1.18	7.09	1.24	1.14	7.93	1.14	1.06	7.06	1.08	1.03	5.07
200	1.11	1.14	3.25	1.27	1.20	5.83	1.37	1.30	5.55	1.42	1.34	5.36	1.39	1.33	4.07	1.24	1.21	2.53	1.14	1.14	0.16
100	1.26	1.21	3.72	1.42	1.31	7.41	1.56	1.44	7.96	1.63	1.49	8.53	1.55	1.42	8.48	1.42	1.32	6.91	1.27	1.24	2.76
0	1.30	1.25	3.46	1.48	1.34	9.84	1.63	1.47	10.00	1.70	1.51	11.08	1.63	1.47	9.88	1.47	1.32	9.68	1.30	1.23	5.00
-100	1.30	1.21	6.93	1.47	1.28	12.68	1.58	1.42	9.87	1.61	1.50	7.20	1.55	1.43	7.57	1.42	1.30	8.11	1.28	1.23	4.24
-200	1.16	1.13	2.53	1.21	1.22	-0.39	1.42	1.31	7.76	1.45	1.33	8.36	1.40	1.30	7.11	1.28	1.20	6.34	1.17	1.13	3.92
-250	1.09	1.00	8.06	1.19	1.05	11.44	1.27	1.16	9.06	1.34	1.18	12.45	1.30	1.14	12.16	1.24	1.07	13.65	1.09	1.01	7.14

**Table 2.** Absorbed dose measurement in situ, numerical calculations, and their comparison. Distance from the source – 820 mm

Distance Z, mm	Dose rates, kGy/h																				
	Y, mm																				
	-300			-200			-100			0			100			200			300		
	M	C	C <sub>m</sub>	M	C	C <sub>m</sub>	M	C	C <sub>m</sub>	M	C	C <sub>m</sub>	M	C	C <sub>m</sub>	M	C	C <sub>m</sub>	M	C	C <sub>m</sub>
250	0.635	0.61	3.35	0.65	0.64	1.92	0.69	0.66	4.64	0.70	0.68	2.97	0.69	0.64	7.52	0.66	0.64	4.39	0.64	0.60	5.24
200	0.649	0.65	0.08	0.69	0.66	4.79	0.72	0.69	3.39	0.72	0.71	2.64	0.71	0.70	2.05	0.69	0.66	4.64	0.66	0.64	2.41
100	0.710	0.65	8.68	0.74	0.69	7.54	0.76	0.71	6.06	0.79	0.72	9.05	0.77	0.72	6.86	0.74	0.68	7.68	0.70	0.66	6.11
0	0.725	0.67	7.05	0.76	0.70	7.25	0.79	0.73	8.16	0.82	0.72	12.38	0.81	0.72	10.18	0.76	0.68	10.02	0.73	0.68	6.91
-100	0.710	0.66	7.27	0.76	0.67	11.21	0.79	0.72	9.05	0.79	0.72	8.92	0.78	0.72	8.09	0.75	0.69	8.12	0.72	0.66	7.71
-200	0.687	0.64	6.65	0.72	0.67	6.32	0.75	0.70	7.19	0.76	0.72	5.40	0.75	0.70	6.26	0.73	0.68	6.22	0.67	0.65	3.07
-250	0.638	0.61	3.78	0.71	0.61	13.75	0.71	0.65	8.25	0.73	0.67	7.33	0.75	0.67	10.93	0.72	0.62	13.57	0.64	0.62	3.16

**Table 3.** Absorbed dose measurement in situ, numerical calculations, and their comparison. Distance from the source – 1700 mm

Distance Z, mm	Dose rates, kGy/h																				
	Y, mm																				
	-300			-200			-100			0			100			200			300		
	M	C	C <sub>m</sub>	M	C	C <sub>m</sub>	M	C	C <sub>m</sub>	M	C	C <sub>m</sub>	M	C	C <sub>m</sub>	M	C	C <sub>m</sub>	M	C	C <sub>m</sub>
250	0.43	0.39	10.15	0.43	0.40	5.31	0.45	0.42	5.98	0.44	0.42	6.36	0.44	0.41	5.86	0.44	0.41	6.32	0.43	0.39	10.15
200	0.45	0.41	7.08	0.49	0.41	15.69	0.50	0.43	15.51	0.53	0.44	17.07	0.52	0.43	17.09	0.50	0.42	16.91	0.46	0.40	12.60
100	0.45	0.41	8.91	0.47	0.43	7.94	0.47	0.44	5.37	0.48	0.43	11.30	0.48	0.44	7.69	0.47	0.42	9.45	0.45	0.41	8.87
0	0.47	0.42	9.45	0.47	0.43	9.93	0.48	0.44	12.13	0.49	0.44	9.33	0.48	0.44	9.03	0.47	0.42	11.62	0.46	0.41	10.48
-100	0.45	0.41	8.21	0.47	0.42	9.87	0.47	0.43	9.93	0.48	0.44	7.06	0.48	0.44	7.48	0.47	0.42	11.84	0.45	0.42	6.42
-200	0.44	0.42	4.72	0.46	0.42	8.09	0.47	0.44	6.01	0.48	0.43	10.62	0.48	0.42	11.25	0.48	0.42	12.71	0.45	0.42	7.31
-250	0.44	0.40	8.22	0.46	0.41	11.78	0.48	0.42	13.13	0.47	0.43	9.29	0.47	0.41	13.11	0.47	0.40	14.38	0.44	0.40	7.99





### CONCLUSION

The complex geometry of the Izotop irradiation facility was input into simulation. All proper physical processes and particles were included into the simulation and the numerical simulations were carry out.

The calculations were carried out for 109 events. Approximately time of calculations were 72 h. Comparison between measured and simulated results were done (Tables 1, 2, 3).

The accuracy of simulated results in comparison with measured ones is in the range 0.16 – 17.08 %. The accuracy can be improved by the increasing of the simulated events what will demands the using of the high-performance cluster (HPC).

### ORCID IDs

 Volodymyr Morgunov, <https://orcid.org/0000-0002-8681-1941>;  Serhii Lytovchenko, <https://orcid.org/0000-0002-3292-5468>  
 Volodymyr Chyshkala, <https://orcid.org/0000-0002-8634-4212>;  Bohdan Mazilin, <https://orcid.org/0000-0003-1576-0590>

### REFERENCES

- [1] B.P. Fairand, *Radiation Sterilization for Health Care Products: X-Ray, Gamma, and Electron Beam*, (CRC Press, Boca Raton, 2014), <https://doi.org/10.1201/9781482286205>.
- [2] S.N. Hajare, *Radiation technology for preservation and hygienization of food and agricultural commodities*, INIS Reference Number: 48066274 (Sinhgad Institutes, India, 2017).
- [3] A.G. Chmielewski, *Radiation Physics and Chemistry*, **76**, 1480 (2007), <https://doi.org/10.1016/j.radphyschem.2007.02.056>.
- [4] S.I. Borrely, A.C. Cruz, N.L. Del Mastro, M.H.O. Sampa, and E.S. Somessari, *Progress in Nuclear Energy*, **33**, 3 (1998), [https://doi.org/10.1016/S0149-1970\(97\)87287-3](https://doi.org/10.1016/S0149-1970(97)87287-3)
- [5] M. R. Cleland, L. A. Parks, and S. Cheng, en, *Nuclear Instruments and Methods in Physics Research Section B: Beam Interactions with Materials and Atoms, Ionizing Radiation and Polymers*, **208**, 66 (2003), [https://doi.org/10.1016/S0168-583X\(03\)00655-4](https://doi.org/10.1016/S0168-583X(03)00655-4).
- [6] L. Cortella, C. Albino, Q.-K. Tran, and K. Froment, *Radiation Physics and Chemistry* **171**, 108726 (2020), <https://doi.org/10.1016/j.radphyschem.2020.108726>.
- [7] P. Andreo, D. T. Burns, A. E. Nahum, J. Seuntjens, and F. H. Attix, *Fundamentals of Ionizing Radiation Dosimetry*, (John Wiley & Sons, Aug. 2017).
- [8] S. Agostinelli, J. Allison, K. Amako, J. Apostolakis, H. Araujo, P. Arce, M. Asai, and et al, en, *Nuclear Instruments and Methods in Physics Research Section A: Accelerators, Spectrometers, Detectors and Associated Equipment* **506**, 250 (2003), [https://doi.org/10.1016/S0168-9002\(03\)01368-8](https://doi.org/10.1016/S0168-9002(03)01368-8).
- [9] J. Allison, K. Amako, J. Apostolakis, H. Araujo, P. Arce Dubois, M. Asai, G. Barrand, and et al, *IEEE Transactions on Nuclear Science* **53**, 270 (2006), <https://doi.org/10.1109/TNS.2006.869826>.
- [10] J. Allison, K. Amako, J. Apostolakis, P. Arce, M. Asai, T. Aso, E. Bagli, et al, *Nuclear Instruments and Methods in Physics Research Section A: Accelerators, Spectrometers, Detectors and Associated Equipment*, **835**, 186 (2016), <https://doi.org/10.1016/j.nima.2016.06.125>.
- [11] Institute of Isotopes Ltd., Budapest, Gamma irradiation facility, [https://www.iki.kfki.hu/radsec/irradfac/pub/Gamma\\_Irradiation\\_Facility.pdf](https://www.iki.kfki.hu/radsec/irradfac/pub/Gamma_Irradiation_Facility.pdf)
- [12] International Organization for Standardization, ISO/ASTM 51538:2009 Practice for use of the ethanol-chlorobenzene dosimetry system, Standard (International Organization for Standardization, Geneva, CH, Feb. 2009).
- [13] A. Kovacs, V. Stenger, G. Foeldiak, and L. Legeza, in *High-dose dosimetry* (1985).
- [14] A. Kovacs, I. Slezsak, W.L. McLaughlin, and A. Miller, *Radiation Physics and Chemistry*, **46**, 1211 (1995), [https://doi.org/10.1016/0969-806X\(95\)00357-4](https://doi.org/10.1016/0969-806X(95)00357-4)

### ПОРІВНЯННЯ МІЖ ЗМОДЕЛЬОВАНИМИ ТА ВИМІРЯНИМИ ПОТУЖНЯСТОМИ ДОЗ НА ГАММА-ОБ'ЄКТІ

**В.В. Моргунов<sup>а</sup>, І. Мадар<sup>б</sup>, С.В. Литовченко<sup>а</sup>, В.О. Чишкала<sup>а</sup>, Б.О. Мазілін<sup>а</sup>**

<sup>а</sup>Харківський національний університет імена В.Н. Каразіна, м. Свободи, 4, Харків, 61022, Україна

<sup>б</sup>Інститут "Ізотоп", вул. Конколы-Теге Мікл'ос, 29-33, Будапешт, 1121, Угорщина

У статті наведено опис кроків, які були зроблені для порівняння між чисельно змодельованими та виміряними потужностями дози на гамма-об'єкті Ізотоп (Будапешт, Угорщина) Чисельне моделювання проводилося за допомогою програмного інструментарію GEANT4. Вимірювання дози проводили системою дозиметрів ЕСВ. Порівняння показує хорошу відповідність між змодельованими та виміряними значеннями. Найгірша точність була 17,08%.

**Ключові слова:** поглинута доза, потужність дози, чисельне моделювання, ЕСВ.

## INTERACTION OF NOVEL MONOMETHINE CYANINE DYES WITH PROTEINS IN NATIVE AND AMYLOID STATES<sup>†</sup>

 Olga Zhytniakivska<sup>a,\*</sup>,  Uliana Tarabara<sup>a</sup>,  Atanas Kurutos<sup>b,c</sup>,  Kateryna Vus<sup>a</sup>,  
 Valeriya Trusova<sup>a</sup>,  Galyna Gorbenko<sup>a</sup>

<sup>a</sup>Department of Medical Physics and Biomedical Nanotechnologies, V.N. Karazin Kharkiv National University  
4 Svobody Sq., Kharkiv, 61022, Ukraine

<sup>b</sup>Institute of Organic Chemistry with Centre of Phytochemistry, Bulgarian Academy of Sciences  
Acad. G. Bonchev str., bl. 9, 1113, Sofia, Bulgaria

<sup>c</sup>Department of Pharmaceutical and Applied Organic Chemistry, Faculty of Chemistry and Pharmacy  
Sofia University St. Kliment Ohridski, 1 blv. J. Bourchier, Sofia, 1164, Bulgaria

\*Corresponding Author: [olga.zhytniakivska@karazin.ua](mailto:olga.zhytniakivska@karazin.ua)

Received May 1, 2022; revised May 11, 2022; accepted May 18, 2022

Molecular interactions between novel monomethine cyanine dyes and non-fibrillar and fibrillar proteins were characterized using the fluorescence spectroscopy and molecular docking techniques. To this end, the fluorescence spectral properties of the dyes have been explored in buffer solution and in the presence of insulin and lysozyme in the native and amyloid states. It was observed that association of monomethines with the native and fibrillar proteins was accompanied with a significant enhancement of the fluorophore fluorescence, being more pronounced in the presence of aggregated insulin and lysozyme. The quantitative information about the dye-protein binding was obtained through approximating the experimental dependencies of the fluorescence intensity increase vs protein concentration by the Langmuir model. Analysis of the spectral properties and the binding characteristics of monomethines in the presence of fibrillar insulin and lysozyme showed that the introduction of chloro- and fluorine-substituents to the oxazole yellow derivatives, as well as the long aliphatic substitution on the nitrogen atom of the benzazole chromophore of YO-dyes had a negative impact on the dye amyloid specificity. Molecular docking studies showed that monomethines tend to form the most stable complexes with the B-chain residues Val 17, Leu17, Ala 14, Phe1, Gln 4 and Leu 6 and the A-chain residue Leu 13, Tyr 14, Glu 17 of non-fibrillar insulin and interact with the deep cleft of native lysozyme lined with hydrophobic (Ile98, Ile 58), polar (Thr108, Thr 62, Thr 63) and negatively charged (Asp101, Asp 107) residues. The wet surface groove Gln15\_Glu17 and groove G2-L4/S8-W10 were found as the most energetically favorable binding sites for the examined monomethine dyes in the presence of insulin and lysozyme fibrils, respectively.

**Keywords:** Monomethine cyanine dyes; insulin; lysozyme; amyloid fibrils; molecular docking.

**PACS:** 87.14.C++c, 87.16.Dg

The monomethine cyanine dye oxazole yellow (YO) and its derivatives have continuously attracted tremendous interest in a variety of biomedical applications: i) as effective fluorescent probes for the DNA detection [1-5], sizing, purification of DNA fragments [6] and visualization of a single DNA molecules using fluorescent microscopy [7, 8]; ii) as selective indicators for the internal loop of the bacterial A-site RNA [9]; iii) for the production of the nanohybrid fluorescent materials based on the self-assembling the DNA wrapped carbon nanotubes and YO dyes [10]; iv) for monitoring the bacteriophage T5 capsid permeability for small molecules [11] and for detection and characterization of the MS2 bacteriophage [12]; v) for synthesis a dsDNA-sensitive fluorescent oxazole yellow-peptide bioconjugates [13]; vi) for detection of amyloid protein aggregates [14,15], to name only a few. These research activities are driven by the advantageous photophysical properties of YO derivatives, namely: i) high molar extinction coefficients; ii) high quantum yield and a strong fluorescence enhancement in the presence of specific biomolecules; iii) an ability to switch from a “dark state” to a fluorescent state in the presence of a restrictive environment such as base-pairs of double stranded DNA or amyloid fibril beta-sheet core; iv) feasible conjugation with various biological targets. To exemplify, oxazole yellow and its derivatives are virtually non-fluorescent in buffer solution but form stable intercalating complexes with double-stranded DNA, enhancing their fluorescence more than 1000 times [1-6]. Besides, a homodimeric derivative of oxazole yellow, YOYO-1, appeared to be especially useful for the detection of amyloid fibrils exhibiting about 200-fold emission enhancement upon binding to the A $\beta$ (1-42) amyloid aggregates and a characteristic absorption shift originated from a self-stacking to non-stacking transition in its homodimer [14]. Notably, Cavuslar and Unal demonstrated a possibility of utilization of YO derivatives as fluorescent hybrid nanomaterials due to their light-up behavior when they interact with carbon nanotubes and DNA wrapped carbon nanotubes [10].

In the present study, the fluorescence spectroscopy and molecular docking techniques were used to explore the interaction of the novel monomethine cyanine oxazole yellow derivatives (Figure 1) with proteins in the native and amyloid states. To this end, the fluorescence spectral properties of YO-dyes were studied in the presence of native (non-fibrillar) and fibrillar insulin or lysozyme. More specifically, our aim was two-fold: i) to perform comparative analysis of

<sup>†</sup> Cite as: O. Zhytniakivska, U. Tarabara, A. Kurutos, K. Vus, V. Trusova, and G. Gorbenko, East Eur. J. Phys. 2, 124 (2022), <https://doi.org/10.26565/2312-4334-2022-2-16>

© O. Zhytniakivska, U. Tarabara, A. Kurutos, K. Vus, V. Trusova, G. Gorbenko, 2022

the spectral behaviour and binding parameters of the cyanine dyes in the non-fibrillar and fibrillar proteins; ii) to determine potential binding sites for the novel dyes in the nonaggregated and fibrillar insulin and lysozyme.

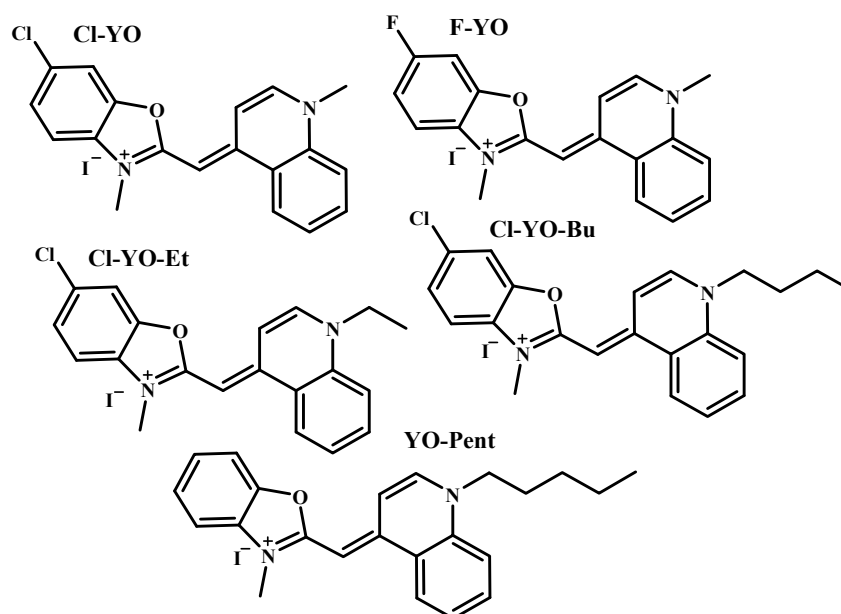


**Figure 1.** Structural formulas of monomethine cyanine dyes

## EXPERIMENTAL SECTION

### Materials

Bovine insulin (Ins), egg yolk lysozyme (Lz) and thioflavin T (ThT) were purchased from Sigma, USA. The monomethine cyanine dyes were kindly provided by Prof. Todor Deligeorgiev (Faculty of Chemistry, University of Sofia, Bulgaria). All other reagents were of analytical grade and used without the further purification. The structural formulas of the employed fluorescent dyes are shown in Fig. 1.

### Preparation of working solutions

Stock solutions of the monomethine cyanines were prepared immediately before the fluorescence measurements by dissolving the dyes in dimethyl sulfoxide. The ThT stock solution was prepared in 5 mM sodium phosphate buffer, pH 7.4. The concentrations of cyanine dyes and ThT were determined spectrophotometrically using their molar absorptivities  $72600 \text{ M}^{-1} \text{ cm}^{-1}$ ,  $60300 \text{ M}^{-1} \text{ cm}^{-1}$ ,  $64000 \text{ M}^{-1} \text{ cm}^{-1}$ ,  $90500 \text{ M}^{-1} \text{ cm}^{-1}$ ,  $90400 \text{ M}^{-1} \text{ cm}^{-1}$  and  $36000 \text{ M}^{-1} \text{ cm}^{-1}$  for Cl-YO, F-YO, Cl-YO-Et, Cl-YO-Bu, YO-Pent and ThT, respectively [12]. Working solutions of monomethines were prepared by dilution of the dye stock solutions in the sodium phosphate buffer, pH 7.4.

The insulin and lysozyme stock solutions (10 mg/ml) were prepared by dissolving the protein in 10 mM glycine buffer (pH 2.0). These solutions were used as references for non-aggregated proteins. Hereafter, the non-fibrillar insulin and lysozyme forms are designated as InsN and LzN, respectively. To prepare the insulin amyloid fibrils, this solution was subjected to constant agitation on the orbital shaker at 37 °C. Amyloid fibrils of lysozyme were obtained by the protein incubation in 10 mM glycine buffer at pH 2 and 60 °C for 14 days. The nature of the protein aggregates was confirmed by ThT assay and the transmission electron microscopy (data not shown). Hereafter, the fibrillar insulin and lysozyme are designated as InsF and LzF, respectively. The working solutions of proteins were prepared by dissolving a stock solution of the non-fibrillar or fibrillar insulin or lysozyme in 5 mM sodium phosphate buffer (pH 7.4).

### Fluorescence measurements

Steady-state fluorescence spectra were recorded with LS-55 spectrofluorimeter (Perkin Elmer, UK) at 20 °C using 10 mm path-length quartz cuvettes. Emission spectra were carried out in 5 mM sodium phosphate buffer (pH 7.4) and in the presence of non-fibrillar or fibrillar proteins with excitation wavelengths of 460 nm. The excitation and emission slit widths were set at 10 nm.

### Binding model

Quantitative characteristics of the dye-protein binding were determined in terms of the Langmuir adsorption model by analyzing protein-induced changes in the probe fluorescence intensity at the wavelengths, corresponding to



emission maxima for each dye [16]. Briefly, approximation of the experimental dependencies  $\Delta I$  (fluorescence intensity increase) on  $C_p$  (total protein concentration) by Eq. 1 allowed us to determine the dye-protein binding parameters – association constant ( $K_a$ ), binding stoichiometry ( $n$ ) and molar fluorescence ( $\alpha$ ), characterizing the difference between molar fluorescence of the bound and free dye:

$$\Delta I = 0.5\alpha[Z_0 + nC_p + 1/K_a - \sqrt{(Z_0 + nC_p + 1/K_a)^2 - 4nC_pZ_0}] \quad (1)$$

where  $Z_0$  is the total probe concentration.

### Molecular docking studies

To define the most energetically favorable binding sites for the examined dyes on the non-fibrillar and fibrillar proteins, the molecular docking studies were performed using the AutoDock (version 4.2) incorporated in the PyRx software (version 0.8) [17]. The chromophore structures were built in MarvinSketch (version 18.10.0) and optimized in Avogadro (version 1.1.0) [18,19]. Crystal structures of hen egg white lysozyme (PDB ID: 3A8Z) and bovine insulin (PDB ID: 2ZP6) were taken from the Protein Data Bank. Lysozyme fibril was built from the K-peptide, GILQINSRW (residues 54–62 of the wild-type protein), using CreateFibril tool as described previously [20]. The model of the human insulin fibril was obtained from <http://people.mbi.ucla.edu/sawaya/jmol/fibrilmodels/>. The selected docking poses were visualized with the UCSF Chimera software (version 1.14) [21].

## RESULTS AND DISCUSSION

To explore the interaction of the novel monomethine cyanine dye with proteins in globular and amyloid states, at the first step of the study the fluorescence spectral properties of these dyes were studied in the unbound state and in the presence of native and fibrillar insulin and lysozyme. Figure 2 represents typical fluorescence spectra recorded upon titration of cyanine dyes with proteins.

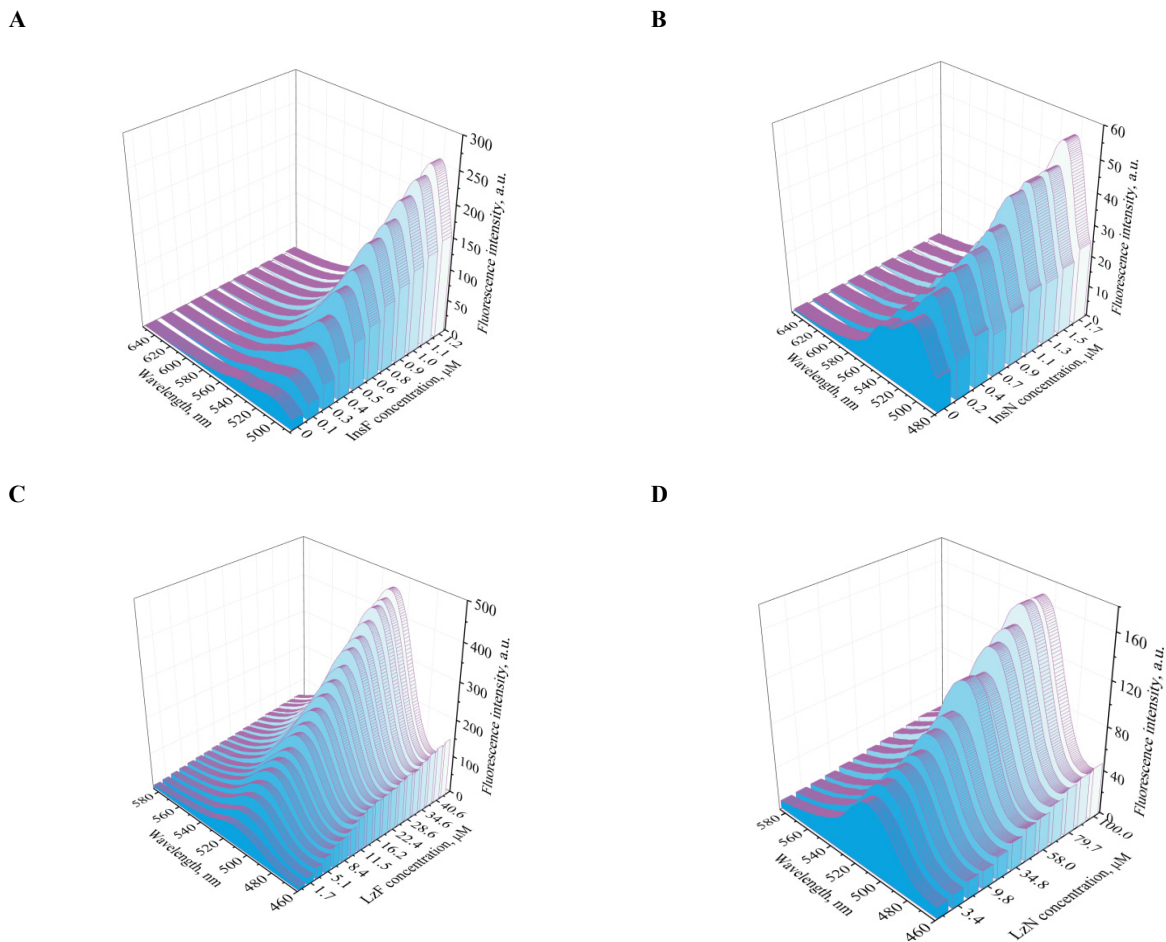


**Figure 2.** Typical emission spectra of Cl-YO-Bu recorded upon the dye fluorimetric titration with InsF (A), InsN(B), LzF (C) and LzN (D). Dye concentrations were 0.1  $\mu\text{M}$  (A, B) and 0.4  $\mu\text{M}$  (C, D), respectively.

The spectral characteristics of cyanine dyes in the presence of the non-fibrillar and fibrillar proteins were evaluated and summarized in Table 1. As seen in Table 1, all examined cyanine dyes exhibit a weak fluorescence in the

buffer solution with the emission maxima centered in the range 510-513 nm depending on the dye chemical structure. The addition of the non-fibrillar insulin resulted in a  $\sim 10$  nm hypsochromic shift of the emission maxima of monomethines, along with a slight fluorescence intensity increase. Elevating concentrations of the native lysozyme resulted in a more pronounced change of the cyanine emission coupled with a slight (3-5 nm) shift of the emission maxima to the lower wavelengths. Such behavior may be a consequence of a higher affinity of these dyes for lysozyme protein monomers in comparison with insulin. As shown in Table 1, the spectral response of the cyanines to the fibrillar proteins lies in a strong increase of the dye fluorescence ( $I_f$ ) as opposed to that in buffer ( $I_0$ ) and in the presence of nonfibrillar protein ( $I_n$ ), with a magnitude of the fluorescence intensity increase being more pronounced in the presence of the insulin amyloid fibrils. The fluorescence maxima of the monomethines are shifted by approximately 3-6 nm (depending on the dye chemical structure) towards shorter wavelengths compared to those observed in the non-aggregated proteins. These effects can be explained by a fluorophore transfer into a less polar and motionally restricted protein environment. Moreover, the emission spectra for all monomethine dyes bound to the lysozyme fibrils were red shifted for 5-9 nm (depending on dye structure) in comparison with those in the presence of the fibrillar insulin. The above finding most probably indicates that the cyanine dyes bind to more polar binding sites in the lysozyme amyloid fibrils than that on the insulin fibrils. Notably, the sensitivity of the dye spectral properties to the changes in the protein environment was previously reported for Michler's hydrol blue and Nile red [22,23].

**Table 1.** Spectral characteristics of the monomethine cyanine dyes in buffer and in the presence of native and fibrillar proteins

	Free dye		InsN		InsF		ADF	LzN		LzF		ADF
	$\lambda_{em}$	$I_0$	$\lambda_{em}$	$I_n$	$\lambda_{em}$	$I_f$		$\lambda_{em}$	$I_n$	$\lambda_{em}$	$I_f$	
Cl-YO	513	34.3	502	69.2	501	300.6	6.7	509	142.7	506	366.4	3.71
Cl-YO-Bu	511	31.9	506	47.4	501	258.1	6.3	505	167.1	507	473.9	5.5
Cl-YO-Et	513	34.4	502	34.7	499	220.9	5.4	509	105.9	507	215.2	2.2
F-YO	511	19.6	501	27.8	499	198.1	8.4	511	64.1	508	114.8	2.5
YO-Pent	510	53.7	502	63.0	500	354.3	5.3	508	94.1	506	327.6	3.47

$\lambda_{em}$  (nm)– the lowest energy maximum of the excitation spectra;  $I_0$ ,  $I_n$ , and  $I_f$  – fluorescence intensity of the dyes in buffer and in the presence of nonfibrillar and fibrillar proteins, respectively. Nonfibrillar and fibrillar insulin concentrations were 1.2  $\mu$ M. Native and fibrillar lysozyme concentrations were 44  $\mu$ M.

To determine the specificity of the examined cyanines to amyloid fibrils, the fluorescence spectral data were processed to the amyloid detection factor (ADF) characterizing the ability of a dye to selectively detect the fibrillar state over its native structure relative to the background fluorescence of the dye in buffer [24,25]:

$$ADF = \frac{I_f - I_n}{I_0} \quad (2)$$

It appeared that all dyes under study in the presence of the fibrillar insulin and lysozyme are characterized by the positive ADF values testifying to the higher sensitivity of monomethines to the fibrillar protein aggregates compared to the non-aggregated state. The ADF values for the fibrillar insulin were found to rise in the order YO-Pent  $\rightarrow$  Cl-YO-Et  $\rightarrow$  Cl-YO-Bu  $\rightarrow$  Cl-YO  $\rightarrow$  F-YO, indicating the increase of insulin amyloid selectivity from Yo-Pent to F-Yo dyes. It is worth noting that the long aliphatic substitution on the nitrogen atom of the benzazole chromophore reduces the amyloid specificity of the monomethines (Cl-YO-Et, Cl-YO-Bu, YO-Pent compared to Cl-YO, F-YO). Thus, the steric hindrances may result in the decrement of the number of available protein binding sites for Cl-YO-Et, Cl-YO-Bu and YO-Pent, which possess the bulky alkyl substitutions. Besides, in the presence of lysozyme fibrils the amyloid specificity was found to decrease in the following row Cl-YO-Bu  $\rightarrow$  Cl-YO  $\rightarrow$  YO-Pent  $\rightarrow$  F-YO  $\rightarrow$  Cl-YO-Et. Remarkably, ADF values appeared to be significantly higher in the presence of insulin amyloid fibrils in comparison with lysozyme, suggesting a sensitivity of the examined monomethine cyanines to the fibril morphology.

Next, to derive the quantitative parameters of the dye-protein binding, the experimental dependencies of the measured fluorescence intensity increase ( $\Delta I$ ) vs protein concentration ( $C_p$ ) (Figure 3) were approximated by the Langmuir adsorption model Eq. 1. The quantitative analysis of the dependencies  $\Delta I(C_p)$  allowed us to estimate the parameters of the monomethine complexation with native and fibrillar proteins – association constant ( $K_a$ ), binding stoichiometry ( $n$ ) and the difference between the molar fluorescence of the bound and free dye ( $\alpha$ ) (Table 2).

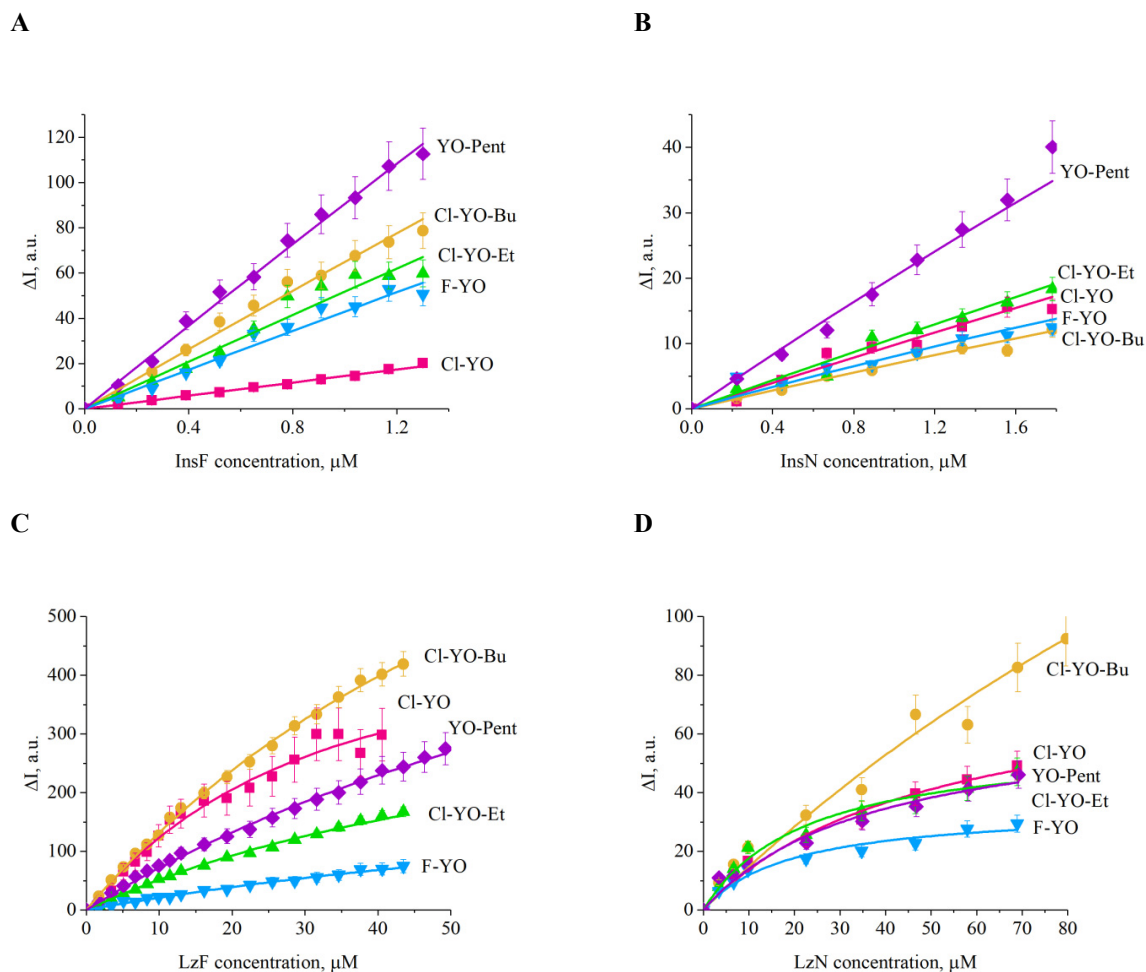


**Figure 3.** The isotherms of the cyanine dyes binding to InsF (A), InsN(B), LzF (C) and LzN (D). Dye concentrations were 0.1 μM (A, B) and 0.4 μM (C, D), respectively.

The results presented in Table 2 indicate that monomethine dyes possess relatively high association constant in the presence of nonfibrillar and fibrillar proteins. Besides, the  $K_a$  values for the examined dyes were ~ 2–30 times higher for the native proteins in comparison with the fibrillar insulin and lysozyme, whereas the values of the molar fluorescence ( $\alpha$ ) were higher in the presence of the amyloid fibrils. All above findings show that despite the positive ADF values, the dyes under study readily associate also with the monomeric (native) proteins.

**Table 2.** Binding characteristics of cyanine dyes in the presence of the non-aggregated and fibrillar proteins

Dye	InsN		InsF		LzN			LzF				
	$K_a \cdot 10^3, \mu M^{-1}$	n	$\alpha \cdot 10^{-3}, \mu M^{-1}$	$K_a \cdot 10^3, \mu M^{-1}$	n	$\alpha \cdot 10^{-4}, \mu M^{-1}$	$K_a \cdot 10^3, \mu M^{-1}$	n	$\alpha, \mu M^{-1}$	$K_a \cdot 10^3, \mu M^{-1}$	n	$\alpha \cdot 10^{-3}, \mu M^{-1}$
Cl-YO	32.36	0.68	4.54	1.92	0.29	25.52	44.92	1.31	85.54	10.77	0.99	0.59
Cl-YO-Bu	57.69	0.73	2.54	29.15	0.62	5.40	35.88	1.05	175.35	15.8	1.0	2.15
Cl-YO-Et	19.66	0.98	5.57	10.33	0.59	8.32	58.26	1.02	102.46	5.32	0.98	2.05
F-YO	72.25	1.00	1.07	14.85	0.57	4.50	77.7	1.01	73.04	63.03	1.03	0.17
YO-Pent	47.39	1.02	4.39	34.28	0.62	4.32	107.42	0.79	83.81	21.85	1.01	1.25

It should also be noted that despite the observed positive ADF values of the cyanine dyes under study, their amyloid specificity is significantly lower in comparison with other amyloid markers [24–28]. In particular the estimated ADF values for the previously reported trimethine cyanine dyes [24] and phenyleneethynylene-based dyes [25] were about twice as large as those calculated in the present work. Moreover, the enhancement of the fluorescence intensity (ratio  $I_f / I_0$ ) in the presence of amyloid fibrils for the all dyes under investigation didn't exceed 10, while for some

cyanine dyes [24, 26], benzanthrone derivatives [27] and  $\beta$ -ketoenoles [28] binding preferences were significantly higher (values of  $I_f/I_0$  ratios were more than 50). Specifically, the binding of a homodimeric derivative of oxazole yellow YOYO to amyloid fibrils was found to be accompanied by a 200-fold emission enhancement [14]. Therefore, the following correlation between the dye structural properties and their amyloid sensing potential can be suggested:

- 1) The introduction of chloro- (Cl-YO-Et, Cl-YO-Bu, Cl-YO) and fluorine-substituents (F-YO) to the oxazole yellow derivatives had a negative impact on the dye amyloid specificity. It should be noted in this respect that in contrast, the chloro-substituent at YOYO structure resulted in a significant increase of the dye affinity for DNA and RNA relative to the parent compounds YOYO [4].
- 2) The long aliphatic substituents on the nitrogen atom of the benzazole chromophore can be responsible for a reduction of the monomethine binding to amyloid fibrils (Cl-YO-Et, Cl-YO-Bu, YO-Pent compared to Cl-YO, F-YO)

To identify the monomethine-protein binding sites, as well as the nature of the interactions involved in the dye-protein complexation in the non-fibrillized proteins and amyloid fibrils, we used the molecular docking technique. The possible binding sites of the dyes under study within the native (Figure 4 panels A, B) and fibrillar (Figure 4, panel E) insulin were identified using the AutoDock tools. All monomethines under study tend to form the most stable complexes with the B-chain residues (Val 17, Leu17, Ala 14, Phe1, Gln 4 and Leu 6) and the residues Leu 13, Tyr 14, Glu 17 of the A-chain of insulin. The protein-ligand interaction profiler PLIP (<https://plip-tool.biotech.tu-dresden.de/plip-web/plip/index>) was used to further characterize the nature of the dye-protein interactions [29]. The binding of the investigated cyanines is governed predominantly by hydrophobic interactions between the dye molecule and the insulin residues Val 17, Leu17, Ala 14, Gln 4 and Leu 6, Leu 13, Tyr 14, Glu 17 (gray dashed lines on the panels C and D, Figure 4). Moreover, it was found that all examined dyes tend to form  $\pi$ -stacking contacts between benzene ring and Phe1 residue of the B-chain of the non-fibrillar insulin (green dashed line on the panel D, Figure 1). The docking results with the fibrillar insulin showed that the wet surface groove Gln15\_Glu17 provides the most energetically favorable binding site for all examined monomethine dyes with the binding affinity for the docked poses equal to -6.05 kcal/mol (Cl-YO), -6.09 kcal/mol (Cl-YO-Bu), -5.72 kcal/mol (F-YO), -5.95 kcal/mol (Cl-YO-Et) and -5.48 kcal/mol (YO-pent).

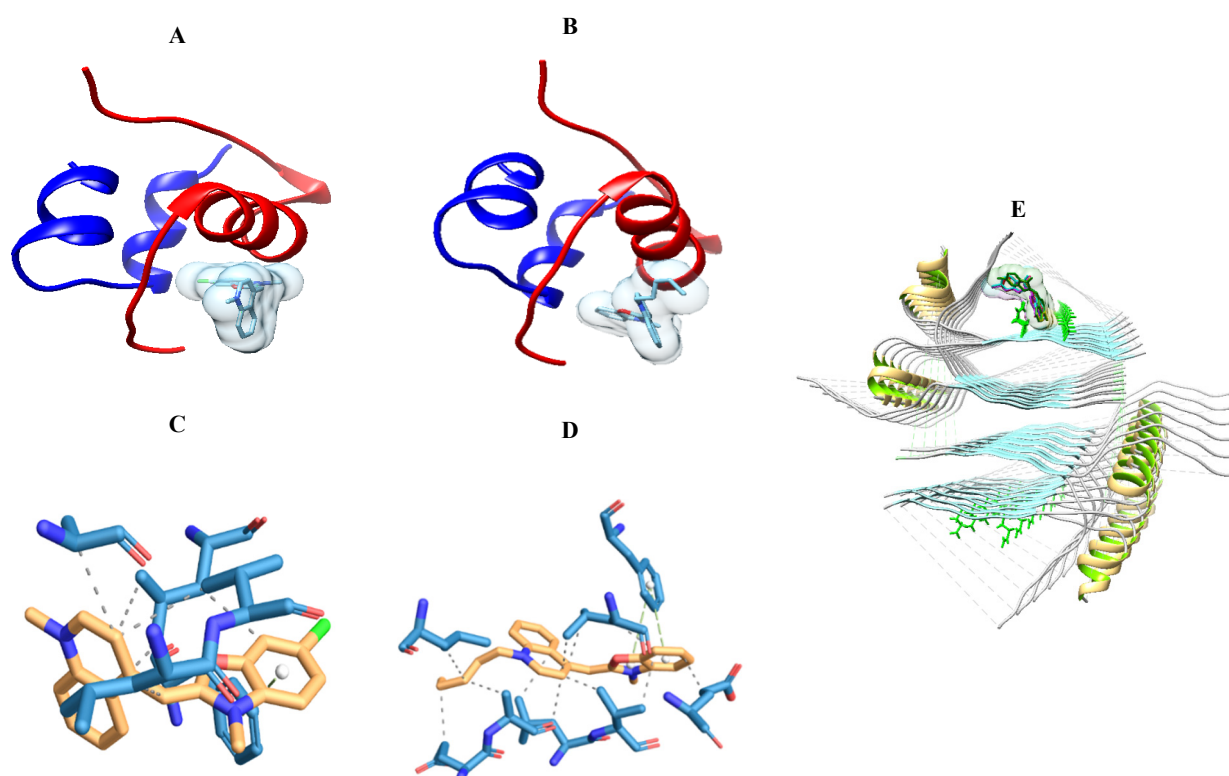


**Figure 4.** Schematic representation of the energetically most favourable dye complexes with the non-fibrillized and fibrillar insulin, obtained using the AutoDock (panels A, B and E) and the protein-ligand interaction profiler PLIP (panels C and D). The panels A and C represent Cl-YO interactions with non-aggregated insulin. Shown in the panels B and D is association of YO-Pent with the B-chain and the A-chain residues of the non-fibrillized protein. The panel E represents the binding of Oxazole yellow derivatives (Cl-YO – green, Cl-YO-Bu – purple, Cl-YO-Et – blue, F-YO – yellow, YO-Pent – red) to the fibrillar insulin.

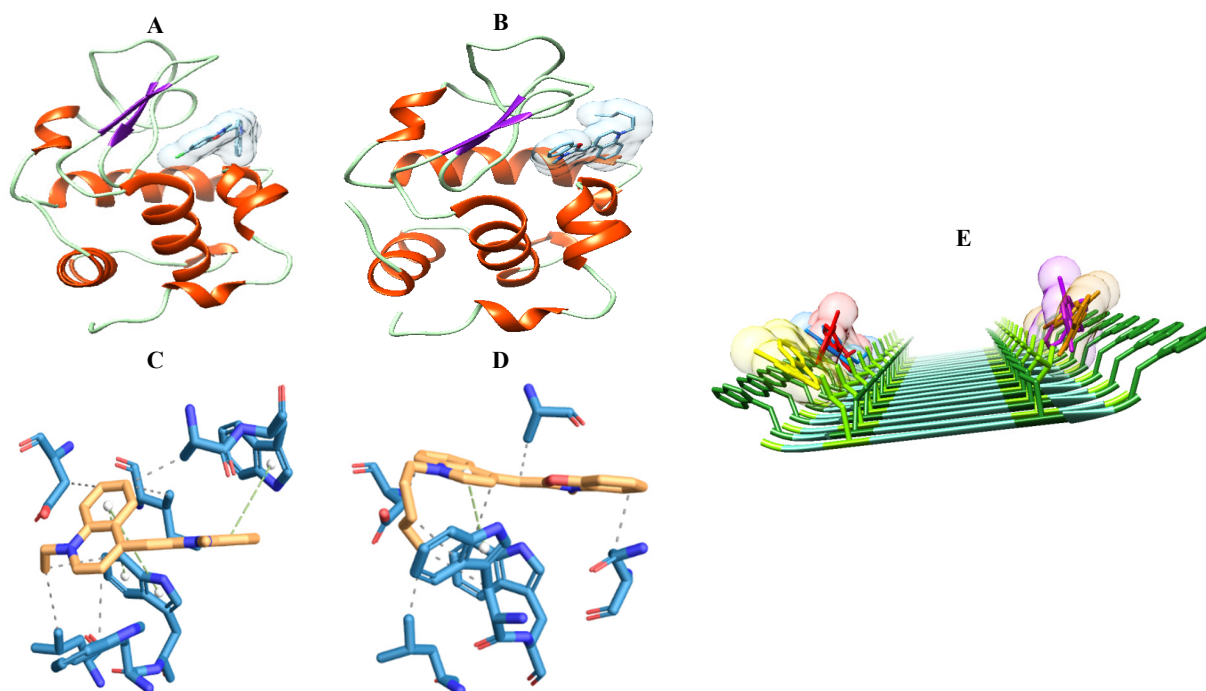


**Figure 5.** Schematic representation of the energetically most favourable dye complexes with the native and fibrillar lysozyme, obtained using the AutoDock (panels A, B and E) and the protein–ligand interaction profiler PLIP (panels C and D). The panels A and C represent Cl-YO-Et interactions with native lysozyme. Shown in the panels B and D is association of YO-Pent with the deep cleft of native lysozyme. The panel E represents the binding of monomethines (Cl-YO – brown, Cl-YO-Bu – purple, Cl-YO-Et – blue, F-YO – yellow, YO-Pent – red) to the groove G2-L4/S8-W10 of the lysozyme fibril.

The novel monomethine dyes interact with the deep cleft of native lysozyme lined with both hydrophobic (Ile98, Ile 58), polar (Thr108, Thr 62 and Thr 63 residues) and negatively (Asp101, Asp 107) charged residues (Figure 5, panels A-D). Similarly to the non-fibrillar insulin, the results obtained using PLIP serve indicate that the dye-lysozyme association is predominantly driven by the hydrophobic dye–protein interactions (dashed grey lines on the panel C and D, Figure 5). Moreover, the docking studies predict that there is a  $\pi$ -stacking interaction between the benzene ring of the dye with Trp 62. The role of the  $\pi$ -stacking interactions in the dye-lysozyme complexation was previously reported also for Azo dyes [30]. Figure 5 D represents that monomethines under study are prone to form the energetically most favourable dye complexes with the groove G2-L4/S8-W10 of the lysozyme fibril. Similarly, classical amyloid marker Thioflavin T preferentially interacted with the grooves, containing aromatic residues [31].







## CONCLUSIONS

To summarize, the present study was focused on the investigation of the interactions between the novel monomethine cyanine dyes and proteins in the non-aggregated and fibrillar states. Using the fluorescence spectroscopy technique it was found, that the oxazole yellow derivatives are readily associate with both non-fibrillar and fibrillar insulin or lysozyme with the magnitude of the dye-protein complexation being higher for the fibrillar proteins. The comparison of the fluorescence responses and the binding parameters in the presence of the fibrillar insulin and lysozyme led us to hypothesize, that novel monomethine dyes are sensitive to the fibril morphology. It was found that the introduction of chloro- and fluorine-substituents to the oxazole yellow derivatives, as well as the long aliphatic substituents on the nitrogen atom of the benzazole chromophore of YO-dyes had a negative impact on the dye amyloid specificity. Based on the molecular docking modeling, it was found that the dye–protein hydrophobic and  $\pi$ -stacking interactions are supposed to have the predominant influence on the association of monomethines with proteins in the non-aggregated and fibrillar states. Overall, the obtained results can be useful for the development and optimization of fluorescent probes for amyloid fibril detection.

## Acknowledgements

This work was supported by the Ministry of Education and Science of Ukraine (the Young Scientist projects № 0120U101064 “Novel nanomaterials based on the lyophilic self-assembled systems: theoretical prediction, experimental investigation and biomedical applications” and the project “Development of novel ultrasonic and fluorescence techniques for medical micro- and macrodiagnostics”).

## ORCID IDs

-  Olga Zhytniakivska, <https://orcid.org/0000-0002-2068-5823>;  Uliana Tarabara, <https://orcid.org/0000-0002-7677-0779>  
 Atanas Kurutos, <https://orcid.org/0000-0002-6847-198X>;  Kateryna Vus, <https://orcid.org/0000-0003-4738-4016>  
 Valeriya Trusova, <https://orcid.org/0000-0002-7087-071X>;  Galyna Gorbenko, <https://orcid.org/0000-0002-0954-5053>

## REFERENCES

- [1] T. Ishiguro, J. Saitoh, H. Yawata, M. Otsuka, T. Inoue, and Y. Sugiura, *Nucleic Acids Res.* **24**, 4492-4497 (1996), <https://doi.org/10.1093/nar/24.24.4992>
- [2] A.S. Biebricher, I. Heller, R.F.H. Roijmans, and T.P. Hoekstra, et al, *Nat. Commun.* **6**, 7304 (2015), <https://doi.org/10.1038/ncomms8304>
- [3] M. Wong, S. Kong, W. H. Dragovska, and M.B. Bally, *Biochim. Biophys Acta*, **1527**, 61-72 (2001), [https://doi.org/10.1016/S0304-4165\(01\)00149-50](https://doi.org/10.1016/S0304-4165(01)00149-50)
- [4] A. Rozman, I. Crnolatac, T. Deligeorgiev, I. Piantanida, and J. Luminesc. **205**, 87-96 (2019), <https://doi.org/10.1016/j.jlumin.2018.08.074>
- [5] A. Furstenberg, T. Deligeorgiev, N. Gadjev, A. Vasilev, and E. Vauthey, *Chem. Eur. J.* **13**, 8600-8609 (2007), <https://doi.org/10.1002/chem.200700665>
- [6] H. Rye, S. Yue, D. Wemmer, M. Quesada, P. Haugland, R. Mathies, et al. *Nucleic Acid Res.* **20**, 2803-2812 (1992), <http://dx.doi.org/10.1093/nar/20.11.2803>
- [7] C.U. Murade, V. Sabramaniam, C. Otto, and M.L. Bennink, *Biophys. J.* **97**, 835-843 (2009), <https://doi.org/10.1016/j.bpj.2009.05.024>
- [8] S. Gurrieri, K. Wells, I. Johnson, and C. Bustamante, *Anal. Biochem.* **249**, 44-53 (1997), <http://dx.doi.org/10.1006/abio.1997.2102>
- [9] Y. Sato, S. Yajima, A. Taguchi, K. Baba, M. Nakagomi, Y. Aiba, and S. Nishizawa, *ChemComm.* **55**, 3183-3186 (2019),
- [10] O. Cavuslar, and H. Unal, *RSC Advances*, **5**, 22380-22389 (2015), <http://dx.doi.org/10.1039/C5RA00236B>
- [11] M. Eriksson, M. Hårdelin, A. Larsson, J. Bergenholtz, B. Akerman, *J. Phys. Chem. B* **111**, 1139-1148 (2007), <http://dx.doi.org/10.1021/jp064322m>
- [12] K. Vus, U. Tarabara, Z. Balklava, D. Neruch, M. Stich, et al, *J. Mol. Liq.* **302**, 112569 (2020), <http://dx.doi.org/10.1016/j.molliq.2020.112569>
- [13] M. Thompson, *Bioconjugate Chem.* **17**, 507-513 (2006), <http://dx.doi.org/10.1021/bc050307t>
- [14] D.J. Lindberg, and E.K. Esbjorner, *Biochem. Biophys. Res. Commun.* **469**, 313-318 (2016), <http://dx.doi.org/10.1016/j.bbrc.2015.11.051>
- [15] S. Stefansson, D.L Adams, and C.-M. Tang, *Biotechniques*, **52**, 26307253 (2012), <http://dx.doi.org/10.2144/000113873>
- [16] K. Vus, V. Trusova, G. Gorbenko, E. Kirilova, G. Kirilov, I. Kalnina, and P. Kinnunen. *Chem. Phys. Lett.* **532**, 110-115 (2012), <http://dx.doi.org/10.1016/j.cplett.2012.02.061>
- [17] S. Dallakyan, and A.J. Olson, *Methods Mol. Biol.* **1263**, 243-250 (2015), [https://doi.org/10.1007/978-1-4939-2269-7\\_19](https://doi.org/10.1007/978-1-4939-2269-7_19)
- [18] P. Csizmadia, In: *Proceedings of ECSOC-3, the third international electronic conference on synthetic organic chemistry*, 367-369 (1999), <https://doi.org/10.3390/ECSOC-3-01775>
- [19] M.D. Hanwell, D.E. Curtis, D.C. Lonie, T. Vandermeersch, E. Zurek, and G.R. Hutchison, *J. Cheminform.* **4**, 17 (2012), <https://doi.org/10.1186/1758-2946-4-17>.
- [20] V. Trusova, *East Eur. J. Phys.* **2**, 51-58 (2015), <https://doi.org/10.26565/2312-4334-2015-2-06>
- [21] E.F. Pettersen, T.D. Goddard, C.C. Huang, G.S. Couch, D.M. Greenblatt, E.C. Meng, and T.E. Ferrin. *J. Comput. Chem.* **25**, 1605-1612 (2004), <https://doi.org/10.1002/jcc.20084>
- [22] C.C. Kitts, T. Beke-Somfai, and B. Norden, *Biochemistry*, **50**, 3451-3461 (2011), <https://doi.org/10.1021/bi102016p>
- [23] R. Mishra, D. Sjölander, and P. Hammarström, *Mol. Biosyst.* **7**, 1232-1240 (2011), <https://doi.org/10.1039/C0MB00236D>
- [24] O. Zhytniakivska, A. Kurutos, U. Tarabara, K. Vus, V. Trusova, G. Gorbenko, N. Gadjev, and T. Deligeorgiev, *J. Mol. Liq.* **311**, 113287 (2020), <https://doi.org/10.1016/j.molliq.2020.113287>
- [25] P.L. Donabedian, M. Evanoff, F.A. Monge, D.G. Whitten, and E.Y. Chi, *ACS Omega*, **2**, 3192-3200 (2017), <https://doi.org/10.1021/acsomega.7b00231>
- [26] K. Volkova, V.B. Kovalska, M. Losytskyy, K.O. Fal, N.O. Derevyanko, et al. *J. Fluoresc.* **21**, 775-784 (2011), <https://doi.org/10.1007/s10895-010-0770-6>
- [27] O. Ryzhova, K. Vus, V. Trusova, E. Kirilova, G. Kirilov, G. Gorbenko, and P. Kinnunen, *Methods Appl. Fluoresc.* **4**, 034007 (2016), <https://doi.org/10.1088/2050-6120/4/3/034007>
- [28] V. Kovalska, S. Chernii, M. Losytskyy, I. Tretyakova, Y. Dovbii, A. Gorski, et al. *New. J. Chem.* **42**, 13308-13318 (2018), <https://doi.org/10.1039/C8NJ01020J>
- [29] S. Salentin, S. Schreiber, V. Joachim Haupt, M.F. Adasme, and M. Schroeder, *Nucleic Acids Res.* **43**, W443-W447 (2015), <https://doi.org/10.1093/nar/gkv315>
- [30] W. Peng, F. Dei, Y.-K. Peng, U.-T. Jiang, and L. Zang. *J. Agr. Food Chem.* **61**, 12415-12428 (2013), <https://doi.org/10.1021/jf4039327>
- [31] M. Biancalana, and S. Koide, *Biochim. Biophys. Acta*, **1804**, 1405-1412 (2010), <https://doi.org/10.1016/j.bbapap.2010.04.001>

**ВЗАЄМОДІЯ НОВИХ МОНОМЕТИНОВИХ ЦІАНІНОВИХ БАРВНИКІВ З БІЛКАМИ У НАТИВНОМУ ТА АМІЛОЇДНОМУ СТАНАХ**

**О. Житняківська<sup>1</sup>, У. Тарабара<sup>1</sup>, А. Курutos<sup>2,3</sup>, К. Вус<sup>1</sup>, В. Трусова<sup>1</sup>, Г. Горбенко<sup>1</sup>**

<sup>1</sup>*Кафедра медичної фізики та біомедичних нанотехнологій, Харківський національний університет імені В.Н. Каразіна м. Свободи 4, Харків, 61022, Україна*

<sup>2</sup>*Інститут органічної хімії та фітохімії Академії Наук Болгарії, Вул. Акад. Бончева, 9, 1113, Софія, Болгарія;*

<sup>3</sup>*Кафедра фармацевтичної та прикладної органічної хімії, Факультет хімії та фармації,*

*Софійський університет імені Св. Климента Охридського, 1164, Софія, Болгарія;*

За допомогою методів флуоресцентної спектроскопії та молекулярного докінгу проведено дослідження молекулярних механізмів взаємодії між новими монометиновими ціаніновими зондами і нефібрилярними та фібрилярними білками. З цією метою, були досліджені флуоресцентні спектральні властивості зондів в буфері та в присутності інсуліну та лізоциму в нативному та амілоїдному станах. Встановлено, що асоціація монометинів з нефібрилярними та фібрилярними білками

супроводжується значним зростанням інтенсивності флуоресценції барвників, яке було більш вираженим у присутності агрегованого інсуліну та лізоциму. Шляхом апроксимації експериментальних залежностей збільшення інтенсивності флуоресценції флуорофору від концентрації білка моделлю Ленгмюра було отримано кількісну інформацію щодо зв'язування зондів з білками. Аналіз спектральних властивостей і отриманих параметрів зв'язування монометинів з фібрилярним інсуліном та лізоцимом показав, що хлор- і фтор-замісники в структурі похідних оксазолowego жовтого, а також довгі аліфатичні групи на атомі азоту бензозолового фрагменту YO-барвників негативно впливають на амліоїдну специфічність барвників. З використанням молекулярного докінгу показано, що монометини мають тенденцію утворювати найбільш стабільні комплекси із залишками Val 17, Leu17, Ala 14, Phe1, Gln 4 і Leu 6 В-ланцюга і залишками Leu 13, Tyr 14, Glu 17 А-ланцюга нефібрилярного інсуліну та з гідрофобними (Ile98, Ile 58), полярними (Thr108, Thr 62, Thr 63) і негативно зарядженими (Asp101, Asp 107) амінокислотними залишками нативного лізоциму. Показано, що жолобки фібрил, що утворені амінокислотними залишками Gln15\_Glu17 в фібрилярному інсуліні та G2-L4/S8-W10 в фібрилах лізоциму є найбільш енергетично вигідними сайтами зв'язування для монометинових зондів.

**Ключові слова:** Монометинові ціанінові зонди, інсулін, лізоцим, молекулярний докінг

## INTERACTIONS OF FIBRILLAR INSULIN WITH PROTEINS: A MOLECULAR DOCKING STUDY<sup>†</sup>

 Valeriya Trusova,  Olga Zhytniakivska,  Uliana Tarabara\*,  Kateryna Vus,  
 Galyna Gorbenko

*Department of Medical Physics and Biomedical Nanotechnologies, V.N. Karazin Kharkiv National University  
4 Svobody Sq., Kharkiv, 61022, Ukraine*

*\*Corresponding Author: [uliana.tarabara@karazin.ua](mailto:uliana.tarabara@karazin.ua)*

Received April 15, 2022, revised May 25, 2022; accepted May 30, 2022

During the last decades growing attention has been paid to ascertaining the factors responsible for the toxic potential of particular protein aggregates, amyloid fibrils, whose formation is associated with a range of human pathologies, including the neurodegenerative diseases, systemic amyloidosis, type II diabetes, etc. Despite significant progress in elucidating the mechanisms of cytotoxic action of amyloid fibrils, the role of fibril-protein interactions in determining the amyloid toxicity remains poorly understood. In view of this, in the present study the molecular docking techniques has been employed to investigate the interactions between the insulin amyloid fibrils (InsF) and three biologically important multifunctional proteins, viz. serum albumin, lysozyme and insulin in their native globular state. Using the ClusPro, HDOCK, PatchDock and COCOMAPS web servers, along with BIOVIA Discovery Studio software, the structural characteristics of fibril-protein complexes such as the number of interacting amino acid residues, the amount of residues at fibril and protein interfaces, the contributions of various kinds of interactions, buried area upon the complex formation, etc. It was found that i) hydrophilic-hydrophilic and hydrophilic-hydrophobic interactions play dominating role in the formation of fibril-protein complexes; ii) there is no significant differences between the investigated proteins in the number of fibrillar interacting residues; iii) the dominating hydrogen bond forming residues are represented by glutamine and asparagine in fibrillar insulin, lysine in serum albumin and arginine in lysozyme; iv) polar buried area exceeds the nonpolar one upon the protein complexation with the insulin fibrils. The molecular docking evidence for the localization of phosphonium fluorescent dye TDV at the fibril-protein interface was obtained.

**Key words:** insulin amyloid fibrils; serum albumin; lysozyme; fibril-protein complex; phosphonium probe.

**PACS:** 87.14.C++c, 87.16.Dg

Over the past decades biomedical research has been revolutionized by the emergence of powerful computational methods among which one of the most widespread is the molecular docking technique allowing to gain atomic-level insights into the mechanisms of various types of biomolecular interactions and high-throughput drug screening [1]. Prediction of three-dimensional structure of the complexes formed by biological macromolecules is a key to better understanding of their functioning. This is a multidimensional optimization problem that is practically unsolvable in an exact way because of complex energy landscapes with many local minima. A multitude of energy functions and optimization algorithms have been developed and the quality of molecular docking predictions is continuously improving [2, 3]. One area where molecular docking tool has found numerous applications concerns exploring the protein-protein interactions (PPIs). The interactions of this kind are involved in a wide variety of fundamental biological processes, such as signal transduction [4], cell growth, differentiation and apoptosis [5, 6], protein synthesis and transport [7], DNA replication and RNA transcription, host-pathogen interactions [8], immune response [9], the assembly of cellular components, regulation of enzymatic activity, etc. Cell functioning is controlled by a complex PPI network termed “interactome” [10], and up to 200,000 PPIs are thought to be involved in the human interactome [11]. Moreover, the aberrant PPIs are associated with a number of human pathologies and are regarded as potential drug targets for a broad range of therapeutic areas, such as cancer therapy [12], infectious diseases [13], heart failure [14], inflammation and oxidative stress [15], neurological disorders [16], etc. A special class of PPIs involves protein self-association into amyloid fibrils, the ordered aggregates with a core  $\beta$ -sheet structure. Amyloid transformation of about 50 disease-specific proteins and accumulation of fibrillar aggregates in various organs and tissues are associated with multiple human disorders, including type-II diabetes [17], cancer [18], neurodegenerative diseases [19], systemic amyloidosis, etc. For instance, extracellular amyloid beta plaques and intra-cellular Tau tangles are formed in Alzheimer’s disease,  $\alpha$ -synuclein positive Lewy bodies are found in Parkinson’s disease and human islet polypeptide deposits are characteristic of type 2 diabetes [20]. Accumulating evidence lends support to hypothesis that multiple species formed along the aggregation pathway (oligomers, protofibrils and polymorphs of mature fibrils), can coherently account for amyloid-induced cellular dysfunction [21]. The suggested mechanisms of amyloid cytotoxicity lie in disruption of plasma and intracellular cell membranes [22-25], suppression of proteasomal degradation [25], impairment of mitochondrial function [26], generation of reactive oxygen species [27] and sequestration of other proteins [23]. It appeared that amyloid fibrils can interact with endogenous proteins, as was demonstrated, in particular, for A $\beta$  peptide and human serum albumin [28]. The

<sup>†</sup> **Cite as:** V. Trusova, O. Zhytniakivska, U. Tarabara, K. Vus, and G. Gorbenko, East Eur. J. Phys. 2, 133 (2022), <https://doi.org/10.26565/2312-4334-2022-2-17>

© V. Trusova, O. Zhytniakivska, U. Tarabara, K. Vus, G. Gorbenko, 2022



amyloid-related aspects of PPIs encompass a range of issues: i) protein self-assembly into amyloid fibrils [20]; ii) inhibition of amyloid growth by proteinaceous compounds [29]; iii) amyloid cross-seeding aggregation [30]; iv) interaction of oligomers and fibrils with endogenous proteins. The last aspect has been addressed in our previous work focused on investigating the complexation of the insulin amyloid fibrils (InsF) with one of three globular proteins, *viz.* serum albumin (SA) lysozyme (Lz) and insulin (Ins) using the fluorescent phosphonium probe TDV. To create a basis for a more comprehensive interpretation of the obtained fluorescence data, the aim of the present study was to elucidate the atomistic details of the interactions between InsF and SA/Lz/Ins utilizing the molecular docking approach.

## METHODS

To predict the most favorable modes of interactions between the insulin amyloid fibrils and proteins, the molecular docking studies were conducted using the ClusPro (<https://cluspro.bu.edu/login.php>) [31, 32] and HDOCK (<http://hdock.phys.hust.edu.cn/>) web servers [33, 34]. The ClusPro was developed to perform the rigid body docking using a Fast Fourier Transform correlation approach. The docking procedure involves filtering the generated complexes according to their desolvation and electrostatic energies, followed by clustering the retained structures with lowest energy and energy minimization for a limited number of structures. A distinguishing feature of ClusPro lies in the scoring of docking solutions on a basis of the cluster size rather than the energy values. This approach assumes that the energy range of the lowest energy docked complexes is comparable to the error in the energy calculation so that further discrimination between the docking structures becomes impossible [31]. The HDOCK implements an FFT-based hierarchical algorithm of rigid-body docking through mapping the receptor and ligand molecules onto grids and global sampling of the possible binding modes with an improved shape complementarity scoring method in which one molecule is fixed, while the second one adopts evenly distributed orientations in rotational Euler space and translational space within a grid. The resulting docking solutions are ranked according to their binding energy and clustered [33]. The PatchDock algorithm involves a geometry-based shape complementarity principles and consists of three main steps: i) molecular shape segmentation into concave, convex and flat patches; ii) surface patch matching and iii) filtering and ranking of the docking positions through their evaluation by geometric shape complementarity fit and atomic desolvation energy scoring function [35]. The web server COCOMAPS (bioCOMplexes COntact MAPS) was used to analyze the properties of interfacial region in the fibril-protein complexes (<https://www.molnac.unisa.it/BioTools/cocomaps/>) by setting a distance cut-off of 5 Å. In the COCOMAPS analyses two residues are considered to be in contact if they present at least two heavy atoms separated by a distance  $\leq 5$  Å. The TDV structure was built in MarvinSketch (version 18.10.0) and the dye geometry was further optimized in Avogadro (version 1.1.0). The dye was docked with the complexes of 50-monomer fragment of insulin fibril model provided by M. Sawaya (<http://people.mbi.ucla.edu/sawaya/jmol/fibrilmodels/>) with one of three proteins, *viz.* bovine serum albumin (PDB code 4f5s), hen egg white lysozyme (PDB code 1aki) and bovine insulin (PDB code 2zp6, chains A, B). The selected docking poses were visualized with the UCSF Chimera software (version 1.14) and analyzed with BIOVIA Discovery Studio Visualizer, v21.1.0.20298, San Diego: Dassault Systemes; 2021.

## RESULTS AND DISCUSSION

As illustrated in Fig. 1, both employed docking tools, ClusPro and HDOCK, provide evidence for the ability of fibrillar insulin to form complexes with serum albumin (Fig.1, A, D), lysozyme (Fig.1, B, E) and insulin (Fig.1, C, F).

The analysis of the selected highest-score docking structures in the web application COCOMAPS revealed the following main tendencies (Table 1): i) the number of interacting residues of fibrillar insulin is comparable for the examined proteins despite the differences in their size, amino acid sequence and physicochemical properties, while the number of interacting residues in protein seems to reflect these differences; ii) the lysozyme-fibril complexes are distinguished by the highest numbers of hydrophilic-hydrophobic and hydrophilic-hydrophilic interactions; iii) the number of hydrophobic-hydrophobic contacts is significantly lower than the number of hydrophilic ones, following the order: SA > Ins > Lz; iv) the size of total interface area is greatest for the complex InsF-SA and is comparable for the complexes InsF-Lz and InsF-Ins; v) the fraction of interface area in fibrillar insulin insignificantly differs for the examined systems; vi) the fraction of the protein interface area follows the order: Ins > Lz > SA; vii) the polar interface (buried) area exceeds the nonpolar one by a factor of  $\sim 3$  for InsF complexes with SA and Ins, and by a factor  $\sim 1.7$  for the system InsF-Lz.

**Table 1.** The general parameters of fibril-protein complexes predicted by ClusPro

Parameter	InsF+SA	InsF+Lz	InsF+Ins	Parameter	InsF+SA	InsF+Lz	InsF+Ins
Number of interacting residues in InsF	40	39	32	Interface area (Å <sup>2</sup> )	1620.5	1383.7	1251.8
Number of interacting residues in protein	43	35	20	Interface area InsF (%)	5.67	7.29	5.30
Number of hydrophilic-hydrophobic interactions	35	57	48	Interface area Protein (%)	2.69	10.98	12.88
Number of hydrophilic-hydrophilic interactions	47	60	32	Polar interface area (Å <sup>2</sup> )	1204.6	863.7	933.45
Number of hydrophobic-hydrophobic interactions	16	6	13	Nonpolar interface area (Å <sup>2</sup> )	415.95	520.0	318.4

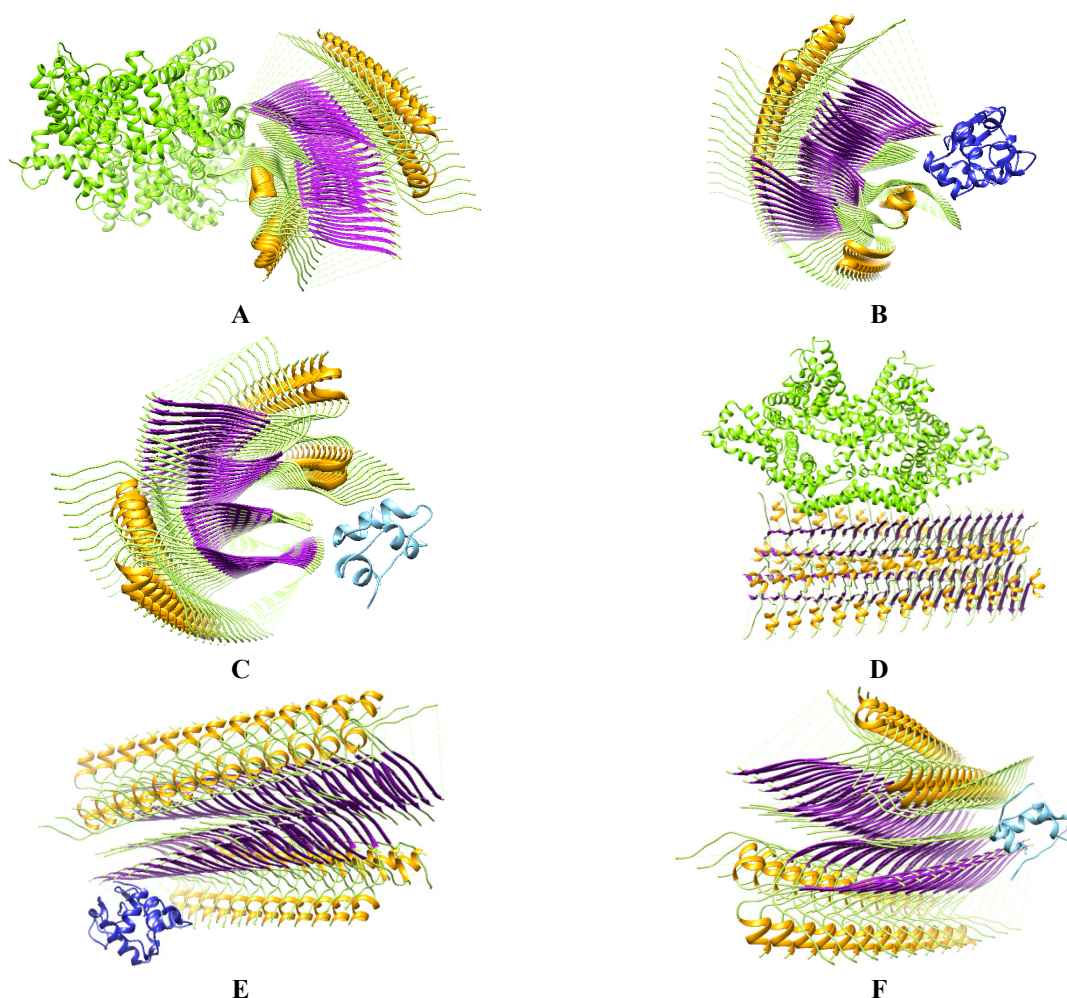


**Figure 1.** The highest-score non-end docking positions obtained from ClusPro (A, B, C) and HDOCK (D, E, F) for the complexes of fibrillar insulin with serum albumin, PDB code 4f5s (A), lysozyme, PDB code 1aki (B) and insulin, PDB code 2zp6, chains A and B (C).

As seen in Table 2, the buried area upon the formation of fibril-protein complexes is rather high, ranging between 3241 for SA and 2504 for Ins. The surface area buried at a protein-protein interface is usually calculated as the sum of the solvent accessible surface areas of the interacting molecules minus the solvent accessible surface area of the complex, not taking into account the possibility of conformational changes of the proteins upon complex formation. The number of residues at the fibrillar interface varies from 36 (InsF-Lz, InsF-Ins) to 47 (InsF-SA), while the amount of residues at the protein interface appeared to be considerably higher for SA (205), compared to Lz (60) and Ins (41).

**Table 2.** Buried and interface areas in the fibril-protein complexes

Parameter	InsF+SA	InsF+Lz	InsF+Ins	Parameter	InsF+SA	InsF+Lz	InsF+Ins
Buried area upon the complex formation ( $\text{\AA}^2$ )	3241.0	2767.4	2503.6	Polar Interface (%)	74.34	62.42	74.57
Buried area upon the complex formation (%)	3.65	8.76	7.51	Nonpolar interface (%)	25.67	37.58	25.44
Polar buried area upon the complex formation ( $\text{\AA}^2$ )	2409.2	1727.4	1866.9	Residues at the interface	252	96	77
Nonpolar buried area upon the complex formation ( $\text{\AA}^2$ )	831.9	1040.0	636.8	Residues at the interface (InsF)	47	36	36
				Residues at the interface (Protein)	205	60	41

Notably, the COCOMAPS data are indicative of a marked role of hydrogen bonding in stabilizing the investigated fibril-protein complexes. As shown in Table 3, the most abundant amino acid residues forming hydrogen bonds are glutamine and asparagine in fibrillar insulin, lysine in serum albumin and arginine in lysozyme. A more detailed analysis of amino acid composition of the contact region in the examined complexes showed that the interface of serum albumin consists of 37% of nonpolar (Leu<sub>177</sub>, Leu<sub>397</sub>, Leu<sub>574</sub>, Ala<sub>500</sub>, Ala<sub>552</sub>, Ala<sub>175</sub>, Ala<sub>581</sub>, Ala<sub>583</sub>, Ala<sub>568</sub>, Val<sub>569</sub>, Val<sub>575</sub>, Val<sub>576</sub>, Pro<sub>179</sub>, Pro<sub>498</sub>, Pro<sub>572</sub>, Phe<sub>501</sub>) residues, 21% of negatively charged (Asp<sub>561</sub>, Asp<sub>172</sub>, Asp<sub>561</sub>, Asp<sub>562</sub>, Glu<sub>171</sub>, Glu<sub>395</sub>, Glu<sub>503</sub>, Glu<sub>548</sub>, Glu<sub>570</sub>), 16% of positively charged (Lys<sub>180</sub>, Lys<sub>396</sub>, Lys<sub>499</sub>, Lys<sub>504</sub>, Lys<sub>535</sub>, Lys<sub>556</sub>, Lys<sub>573</sub>) and 26% of polar (Gln<sub>542</sub>, Gln<sub>542</sub>, Ser<sub>579</sub>, His<sub>534</sub>, His<sub>509</sub>, Thr<sub>507</sub>, Thr<sub>545</sub>, Thr<sub>580</sub>, Asn<sub>549</sub>, Cys<sub>176</sub>, Cys<sub>566</sub>) residues. The interface of lysozyme in its complexes with insulin fibril contains 37% of nonpolar (Val<sub>2</sub>, Phe<sub>3</sub>, Phe<sub>38</sub>, Ile<sub>88</sub>, Ile<sub>124</sub>, Ala<sub>122</sub>, Ala<sub>10</sub>, Ala<sub>11</sub>, Leu<sub>8</sub>, Leu<sub>129</sub>, Gly<sub>4</sub>, Gly<sub>16</sub>, Gly<sub>126</sub>), 6% of amphipathic (Met<sub>12</sub>, Trp<sub>123</sub>), 9% of negatively charged (Asp<sub>87</sub>, Asp<sub>119</sub>, Glu<sub>7</sub>), 23% of positively charged (Arg<sub>5</sub>, Arg<sub>14</sub>, Arg<sub>125</sub>, Arg<sub>128</sub>, Lys<sub>1</sub>, Lys<sub>13</sub>, Lys<sub>33</sub>, Lys<sub>86</sub>) and 25% of polar (Asn<sub>37</sub>, Asn<sub>39</sub>, Asn<sub>93</sub>, Thr<sub>89</sub>, Ser<sub>86</sub>, Gln<sub>121</sub>, Cys<sub>6</sub>, Cys<sub>127</sub>, His<sub>15</sub>) residues. The interface residues of insulin are represented by 40% of nonpolar (Leu<sub>6</sub>, Leu<sub>13</sub>, Leu<sub>15</sub>, Leu<sub>16</sub>, Leu<sub>17</sub>, Val<sub>10</sub>, Val<sub>12</sub>, Val<sub>18</sub>), 10% of amphipathic (Tyr<sub>14</sub>, Tyr<sub>16</sub>), 15% of negatively charged (Glu<sub>13</sub>, Glu<sub>17</sub>, Glu<sub>21</sub>), and 35% of polar (Ser<sub>9</sub>, Ser<sub>12</sub>, Cys<sub>7</sub>, Cys<sub>19</sub>, His<sub>5</sub>, His<sub>10</sub>, Gln<sub>4</sub>) residues. The interface area of the insulin fibrils for all complexes under study includes hydrophobic (Leu, Val, Phe), polar (Asn, Gln, His, Cys) and negatively charged (Glu) residues. The above analyses show that the contribution of hydrophobic amino acids in the fibril-protein complexation is comparable for all examined proteins (~40%), positively charged residues (lysine in SA, arginine and lysine in lysozyme) can interact electrostatically with negatively charged glutamic acid of InsF. Nevertheless, electrostatics is unlikely to play a critical role in the complex formation, since the Ins interface does not contain any positive charge.

**Table 3.** Amino acid residues forming hydrogen bonds in the fibril-protein complexes

Serum albumin	Insulin fibrils	Distance, Å	Lysozyme	Insulin fibrils	Distance, Å
Lys535	Gln304	2.66	Asn39	Asn21	2.84
Lys573	Cys120	3.09	Asn39	Asn121	2.83
Lys573	Asn121	2.94	Arg14	Glu104	2.80
Lys556	Asn21	2.69	Arg14	Asn303	2.77
His534	Gln304	2.85	Arg5	Asn21	3.24
Thr507	Gln304	3.24	Asn37	Asn21	2.83
			Lys33	Asn121	2.57
Insulin			Arg5	Cys319	2.94
Ala14	Gln304	3.30	Arg128	Glu104	2.89
Gln4	His305	2.91	Arg14	Gln304	2.94
Phe1	Gln304	2.81	Arg125	Asn121	3.13
Glu13	His305	2.89	Leu129	Gln304	2.98
			Glu7	Leu306	3.02

At the next step of the study we made an attempt to gain molecular docking insights into the binding behavior of the phosphonium dye TDV in the ternary systems InsF + protein + TDV. This dye has been used in our recent fluorescence study of the interactions between the insulin fibrils and serum albumin / lysozyme / insulin [36]. It has been hypothesized that TDV responsiveness to fibril-protein complexation is associated with its location in the interfacial region. To verify this hypothesis, the molecular docking between InsF-protein structures and TDV was performed using the PatchDock server. As illustrated in Fig. 2 and 3-5, TDV indeed tends to reside at the fibril-protein interface.

The analysis of the docking data via BIOVIA Discovery Studio revealed that different types of binding contacts are involved in the dye-protein complexation, such as van der Waals, alkyl/pi-alkyl, pi-cation interactions, pi-donor and carbon hydrogen bonds (Figs. 3-5, B). Likewise, long-range electrostatic interactions may contribute to the TDV orienting and anchoring at the fibril-protein interface (Figs. 3-5, D).

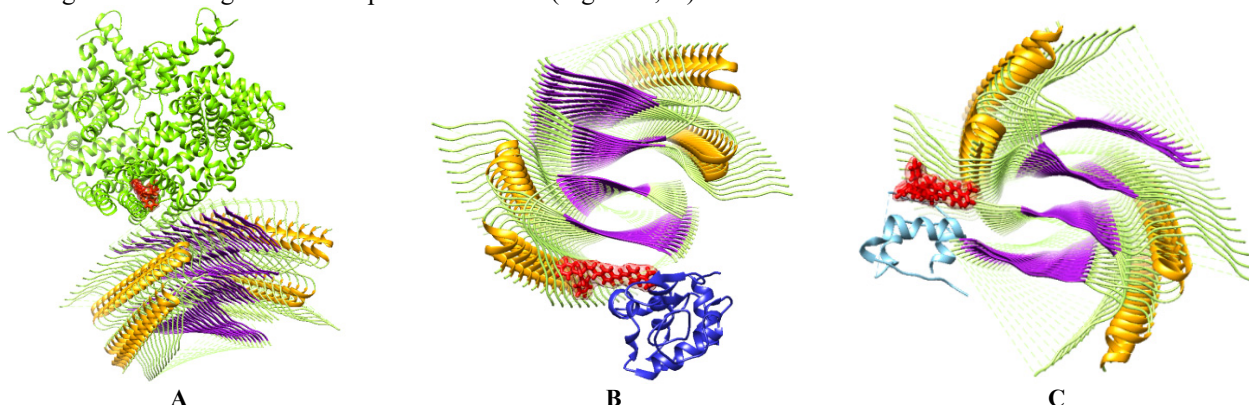


**Figure 2.** Highest-score docking solutions for the ternary complexes insulin fibrils – serum albumin (A)/lysozyme (B)/ insulin (C) - TDV predicted by PatchDock. The TDV molecule is colored in red

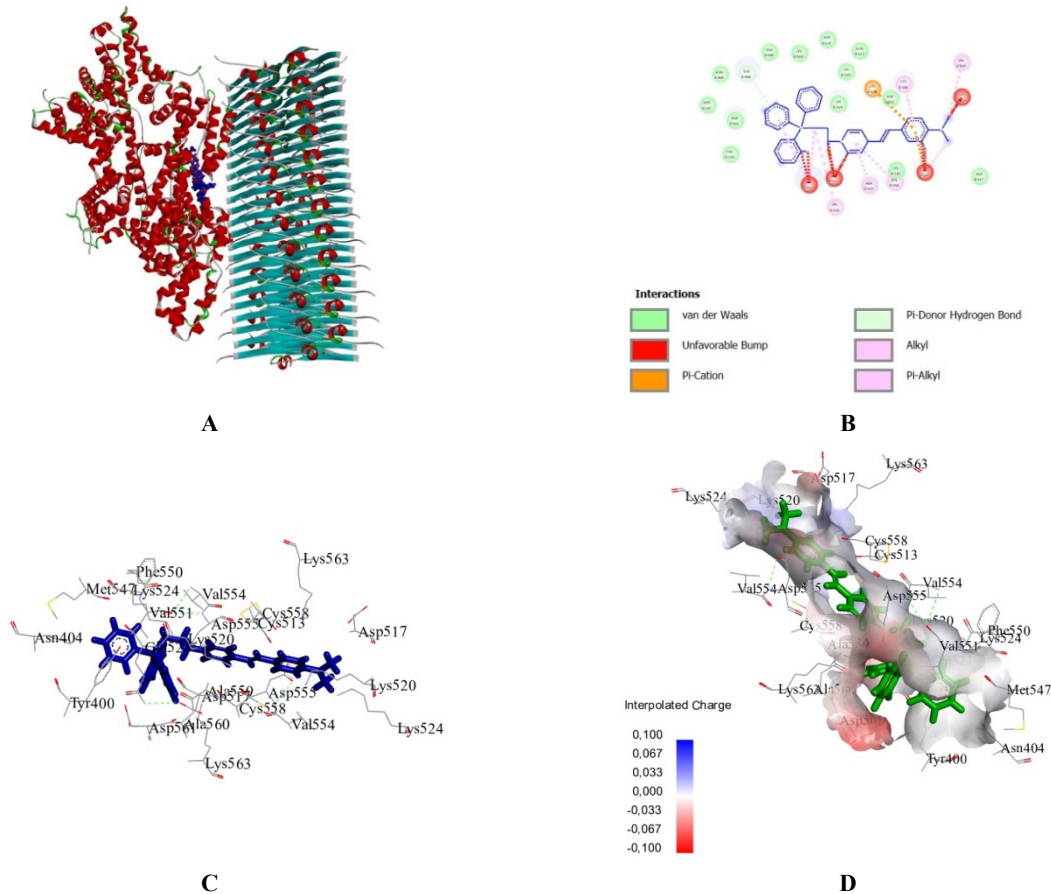


Figure 3. Binding residues and types of interactions between TDV and InsF + SA complexes

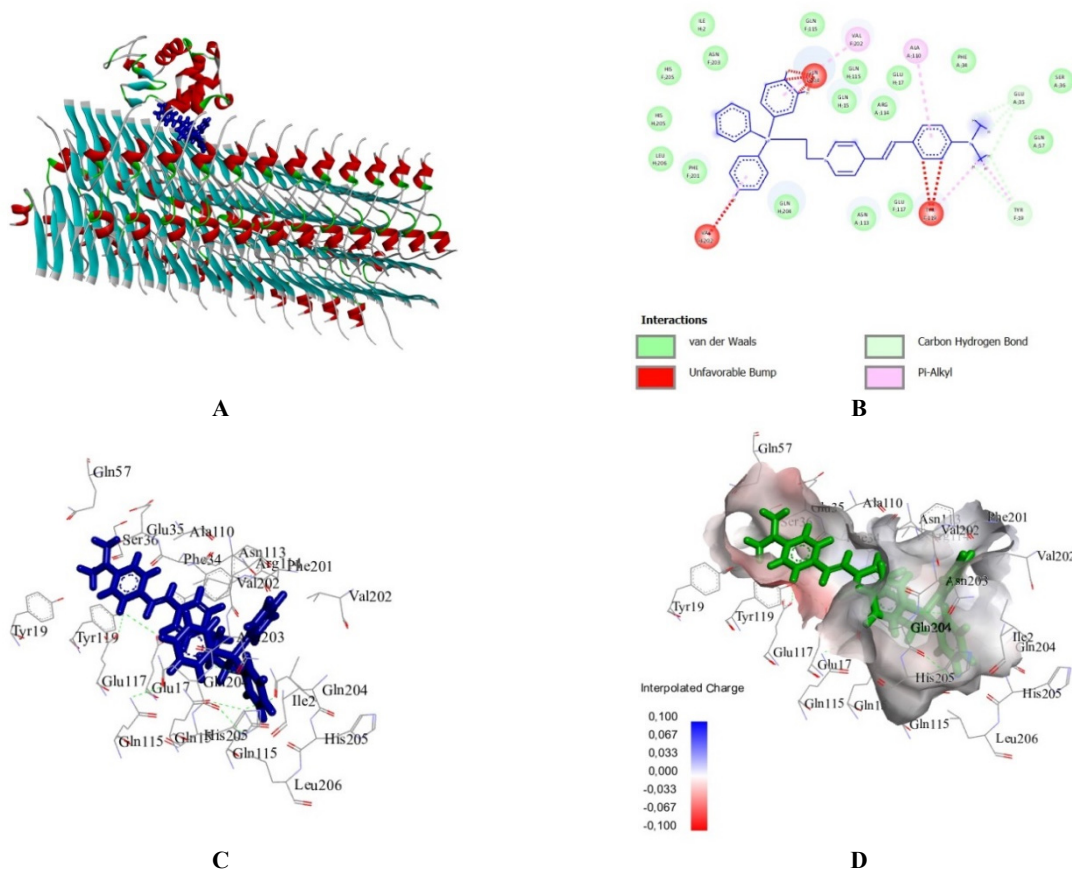
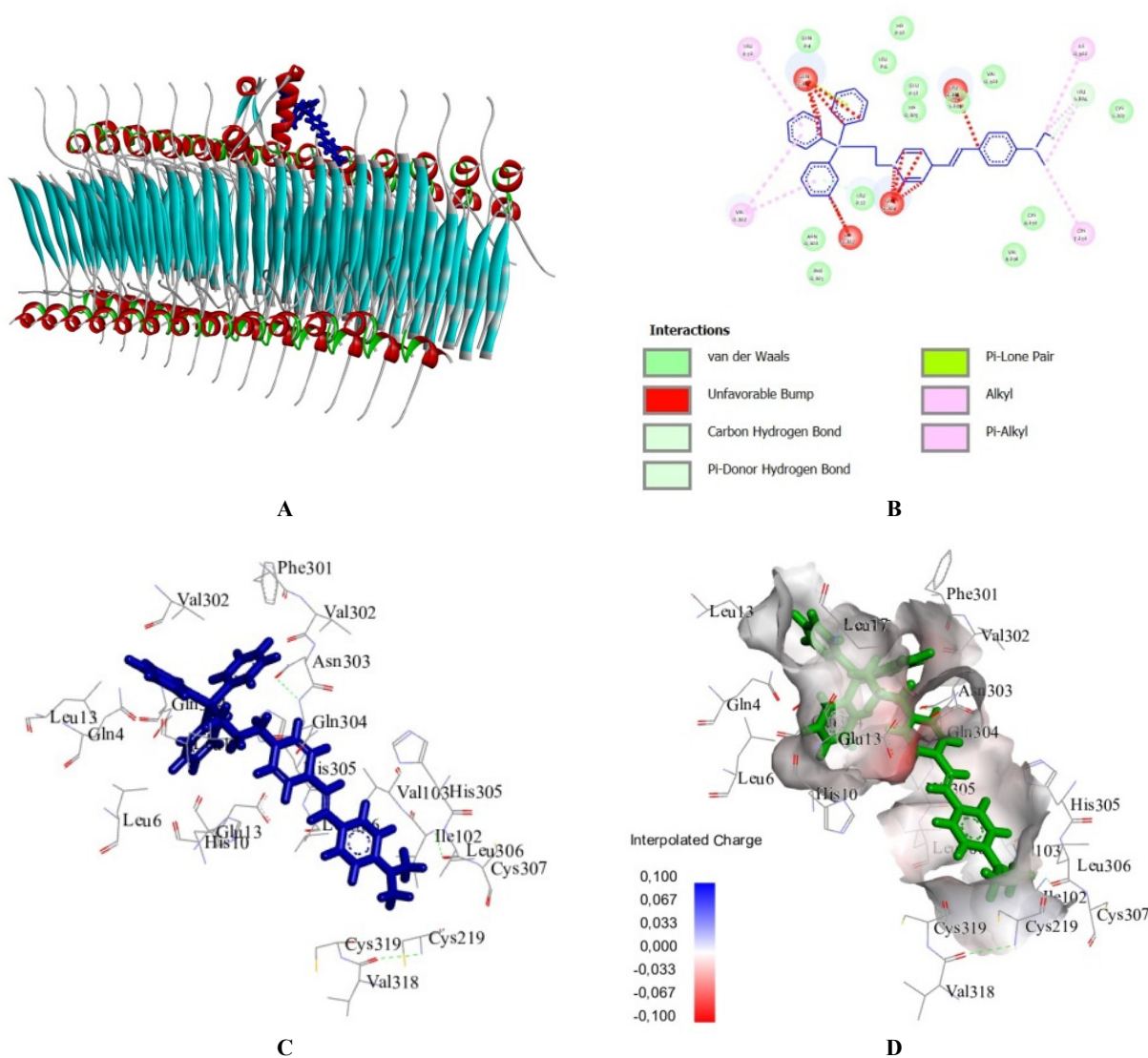


Figure 4. Binding residues and types of interactions between TDV and InsF + Lys complexes.



**Figure 5.** Binding residues and types of interactions between TDV and InsF + Ins complexes.

The most abundant residues in the TDV binding sites are represented by Lys (5), Asp (4), Cys (4), Val (3) for InsF + SA system, Gln (6), Glu (3) for InsF + LZ, and Val (4), Gln (4), His (3), Cys (3) for InsF + Ins. All the above findings, taken together with the results of the previous fluorescence study of analogous fibril-protein and fibril-protein-dye systems, support the idea that amyloid fibrils can form complexes with endogenous proteins, thereby affecting their structural and functional properties.






### CONCLUSIONS

To summarize, the present molecular docking investigation has been undertaken to elucidate the nature of interactions between the insulin amyloid fibrils and biologically important proteins, *viz.* serum albumin, lysozyme and insulin. Using the ClusPro, HDOCK and COCOMAPS web servers, a range of fibril-protein complexation parameters including the number of interacting amino acid residues, the number of different types of interactions, buried area upon the complex formation, the amount of residues at fibril and protein interfaces, etc. Based on the presented results, the following main conclusions can be drawn: i) hydrophilic fibril-protein interactions dominate over the hydrophobic ones in all examined complexes; ii) the amounts of insulin fibril residues interacting with globular proteins are similar for serum albumin, lysozyme and insulin; iii) the hydrophobic leucine, valine and phenylalanine, polar asparagine, glutamine, histidine, cysteine and negatively charged glutamic acid prevail among the interacting residues of fibrillar insulin; iv) glutamine and asparagine in fibrillar insulin, lysine in serum albumin and arginine in lysozyme represent the most abundant hydrogen bond forming residues. The analysis of the binding behavior of fluorescent phosphonium dye TDV using the PatchDock and Discovery Studio tools confirmed the assumption that this dye is located at the fibril-protein interface and can be employed for probing the protein-protein interactions involving the polypeptide chains in amyloid state.

### Acknowledgements

This work was supported by the Ministry of Education and Science of Ukraine (the Young Scientist projects № 0120U101064 “Novel nanomaterials based on the lyophilic self-assembled systems: theoretical prediction, experimental investigation and biomedical applications” and the project “Development of novel means of medical diagnostics by biomedical nanotechnologies and modern ultrasonic and fluorescence methods”).

### ORCID IDs

-  Valeriya Trusova, <https://orcid.org/0000-0002-7087-071X>;  Olga Zhytniakivska, <https://orcid.org/0000-0002-2068-5823>  
 Uliana Tarabara, <https://orcid.org/0000-0002-7677-0779>;  Kateryna Vus, <https://orcid.org/0000-0003-4738-4016>  
 Galyna Gorbenko, <https://orcid.org/0000-0002-0954-5053>

### REFERENCES

- [1] A. Marchand, A.K. Van Hall-Beauvais, and B.E. Correia, *Curr. Opin. Struct. Biol.* **74**, 102370 (2022), <https://doi.org/10.1016/j.sbi.2022.102370>
- [2] L. Zhang, G.Yu, D. Xi, *Neurocomputing*, **324**, 10-19 (2019), <https://doi.org/10.1016/j.neucom.2018.02.097>
- [3] C.J. Morris, and D. Della Corte, *Mod. Phys. Lett. B* **35**, 2130002 (2021), <https://doi.org/10.1142/S0217984921300027>
- [4] X.M. Zhao, R.S. Wang, L. Chen, and K. Aihara, *Nucleic Acids Res.* **36**, 48 (2008), <https://doi.org/10.1093/nar/gkn145>
- [5] T.L. Nero, C.J. Morton, J.K. Holien, J. Wielens, and M.W. Parker, *Nat. Rev. Cancer*, **14**, 248-262 (2014), <https://doi.org/10.1038/nrc3690>
- [6] J. Gao, W.X. Li, S.Q. Feng, Y.S. Yuan, D.F. Wan, W. Han, and Y. Yu, *Genomics*, **91**, 347-355 (2008), <https://doi.org/10.1016/j.ygeno.2007.12.007>
- [7] C.M. Paumi, J. Menendez, A. Arnoldo, K. Engels, K.R. Iyer, S. Thaminy, O. Georgiev, Y. Barral, S. Michaelis, and I. Stagljar, *Mol. Cell*, **26**, 15-25 (2007), <https://doi.org/10.1016/j.molcel.2007.03.011>
- [8] C. Nicod, A. Banaei-Esfahani, and B.C. Collins, *Curr. Opin. Microbiol.* **39**, 7-15 (2017), <https://doi.org/10.1016/j.mib.2017.07.005>
- [9] N. E. Williams, *Methods Cell. Biol.* **62** 449-453 (2000), [https://doi.org/10.1016/S0091-679X\(08\)61549-6](https://doi.org/10.1016/S0091-679X(08)61549-6)
- [10] G.C. Koh, P. Porras, B. Aranda, H. Hermjakob, and S.E. Orchard, *J. Proteome Res.* **11**, 2014-2031 (2012), <https://doi.org/10.1021/pr201211w>
- [11] A.L. Garner, and K.D. Janda, *Curr. Top. Med. Chem.* **11**, 258-280 (2011), <https://doi.org/10.2174/156802611794072614>
- [12] M.R. Arkin, Y. Tang, and J.A. Wells, *Chem. Biol.* **21**, 1102-1114 (2014), <https://doi.org/10.1016/j.chembiol.2014.09.001>
- [13] M. Dawidowski, L. Emmanouilidis, V.C. Kalel, K. Tripsianes, K. Schorpp, K. Hadian, M. Kaiser, P. Maser, M. Kolonko, S. Tanghe, A. Rodriguez, W. Schliebs, R. Erdmann, M. Sattler, and G.M. Popowicz, *Science*, **355**, 1416-1420 (2017), <https://doi.org/10.1126/science.aal1807>
- [14] P. Anand, J.D. Brown, C.Y. Lin, J. Qi, R. Zhang, P.C. Artero, M.A. Alaiti, J. Bullard, K. Alazem, K.B. Margulies, T.P. Cappola, M. Lemieux, J. Plutzky, J.E. Bradner, and S.M. Haldar, *Cell* **154**, 569-582 (2013), <https://doi.org/10.1016/j.cell.2013.07.013>
- [15] M.C. Lu, S.J. Tan, J.A. Ji, Z.Y. Chen, Z.W. Yuan, Q.D. You, and Z.Y. Jiang, *ACS Med. Chem. Lett.* **7**, 835-840 (2016), <https://doi.org/10.1021/acsmchemlett.5b00407>
- [16] M.P. Hayes, M. Soto-Velasquez, C.A. Fowler, V.J. Watts, and D.L. Roman, *ACS Chem. Neurosci.* **9**, 346-357 (2018), <https://doi.org/10.1021/acscchemneuro.7b00349>
- [17] G.J. Cooper, A.C. Willis, A. Clark, R.C. Turner, R.B. Sim, and K.B. Reid, *Proc. Natl. Acad. Sci. USA*, **84**, 8628-8632 (1987), <https://www.ncbi.nlm.nih.gov/pubmed/3317417>
- [18] A.P. Ano Bom, L.P. Rangel, D.C. Costa, G.A. de Oliveira, D. Sanches, C.A. Braga, L.M. Gava, C.H. Ramos, A.O. Cepeda, A.C. Stumbo, C.V. De Moura Gallo, Y. Cordeiro, and J.L. Silva, *J. Biol. Chem.* **287**, 28152-28162 (2012), <http://dx.doi.org/10.1074/jbc.M112.340638>
- [19] M.G. Spillantini, M.L. Schmidt, V.M.-Y. Lee, J.Q. Trojanowski, R. Jakes, and M. Goedert, *Nature*, **388**, 839-840 (1997), <https://doi.org/10.1038/42166>
- [20] R. Gallardo, N.A. Ranson, S.E. Radford, *Curr. Opin. Struct. Biol.* **60**, 7-16 (2020), <https://doi.org/10.1016/j.sbi.2019.09.001>
- [21] M.G. Iadanza, M.P. Jackson, E.W. Hewitt, N.A. Ranson, and S.E. Radford, *Nat. Rev. Mol. Cell. Biol.* **19**, 755-773 (2018), <https://doi.org/10.1038/s41580-018-0060-8>
- [22] F.J. Bauerlein, I. Saha, A. Mishra, M. Kalemantov, A. Martínez-Sánchez, R. Klein, I. Dudanova, M.S. Hipp, F.U. Hartl, W. Baumeister, and R. Fernández-Busnadiego, *Cell*, **171**, 179-187 (2017), <https://doi.org/10.1016/j.cell.2017.08.009>
- [23] H. Olzscha, S.M. Schermann, A.C. Woerner, S. Pinkert, M.H. Hecht, G.G. Tartaglia, M. Vendruscolo, M. Hayer-Hartl, F.U. Hartl, and R. Martin Vabulas, *Cell*, **144**, 67-78 (2011), <https://doi.org/10.1016/j.cell.2010.11.050>
- [24] S.C. Goodchild, T. Sheynis, R. Thompson, K.W. Tipping, W.F. Xue, N.A. Ranson, P.A. Beales, E.W. Hewitt, and S.E. Radford, *PLOS One*, **9**, e104492 (2014), <https://doi.org/10.1371/journal.pone.0104492>
- [25] M.P. Jackson, and E.W. Hewitt, *Essays Biochem.* **60**, 173-180 (2016), <https://doi.org/10.1042/EBC20160005>
- [26] K.F. Winklhofer, C. Haass, *Biochim. Biophys. Acta*, **1802**, 29-44 (2010), <https://doi.org/10.1016/j.bbadis.2009.08.013>
- [27] B. Uttara, A.V. Singh, P. Zamboni, and R.T. Mahajan, *Curr. Neuropharmacol.* **7**, 65-74 (2009), <https://doi.org/10.2174/157015909787602823>
- [28] Xie H, Guo C *Front. Mol. Biosci.* **7**, 629520 (2021), <https://doi.org/10.3389/fmolb.2020.629520>
- [29] C.Q. Liang, and Y.M. Li, *Curr. Opin. Chem. Biol.* **64**, 124-130 (2021), <https://doi.org/10.1016/j.cbpa.2021.05.011>
- [30] I.C. Stancu, B. Vasconcelos, D. Terwel, and I. Dewachter, *Mol. Neurodegener.* **9**, 1-14 (2014), <https://doi.org/10.1186/1750-1326-9-51>
- [31] I.T. Desta, K.A. Porter, B. Xia, D. Kozakov, and S. Vajda, *Structure*, **28**, 1071-1081 (2020), <https://doi.org/10.1016/j.str.2020.06.006>
- [32] S. Vajda, C. Yueh, D. Beglov, T. Bohnuud, S.E. Mottarella, B. Xia, D.R. Hall, and D. Kozakov, *Proteins: Structure, Function, and Bioinformatics*, **85**, 435-444 (2017), <https://doi.org/10.1002/prot.25219>

- [33] Y. Yan, H. Tao, J. He, and S-Y. Huang, *Nat. Protoc.* **15**, 1829–1852 (2020), <https://doi.org/10.1038/s41596-020-0312-x>
- [34] Y. Yan, D. Zhang, P. Zhou, B. Li, and S-Y. Huang, *Nucleic Acids Res.* **45**, W365-W373 (2017), <https://doi.org/10.1093/nar/gkx407>
- [35] C. Zhang, G. Vasmatzis, J.L. Cornette, and C. De Lisi, *J. Mol. Biol.* **267**, 707-726 (1997), <https://doi.org/10.1006/jmbi.1996.0859>
- [36] U. Tarabara, O. Zhytniakivska, K. Vus, V. Trusova, and G. Gorbenko, *East Eur. J. Phys.* **1**, 96-104 (2022), <https://doi.org/10.26565/2312-4334-2022-1-13>

**ВЗАЄМОДІЯ ФІБРИЛЯРНОГО ІНСУЛІНУ З БІЛКАМИ: ДОСЛІДЖЕННЯ  
МЕТОДОМ МОЛЕКУЛЯРНОГО ДОКІНГУ**

**В. Трусова, О. Житняківська, У. Тарабара, К. Вус, Г. Горбенко**

*Кафедра медичної фізики та біомедичних нанотехнологій, Харківський національний університет імені В.Н. Каразіна  
м. Свободи 4, Харків, 61022, Україна*

Протягом останніх десятиріч зростаюча увага приділяється з'ясуванню факторів, відповідальних за токсичний потенціал специфічних білкових агрегатів, амیلлоїдних фібрил, утворення яких пов'язане із низкою патологій людини, включаючи нейродегенеративні захворювання, системний амیلлоїдоз, діабет II-го типу, тощо. Незважаючи на значний прогрес у встановленні механізмів цитотоксичної дії амیلлоїдних фібрил, роль фібрил-білкових взаємодій у визначенні амیلлоїдної токсичності залишається маловивченою. З огляду на це, у даній роботі методом молекулярного докінгу було проведено дослідження взаємодії між амیلлоїдними фібрилами інсуліну (InsF) та трьома біологічно важливими мультифункціональними білками, сироватковим альбуміном, лізоцимом та інсуліном в нативному глобулярному стані. З використанням web-серверів ClusPro, HDOCK, PatchDock, COCOMAPS та програмного пакету BIOVIA Discovery Studio, були визначені структурні характеристики фібрил-білкових комплексів, а саме: число взаємодіючих амінокислотних залишків, кількість залишків на інтерфейсі фібрили та білків, внески різних типів взаємодій, занурена площа при утворенні комплексу, тощо. Було встановлено, що: i) гідрофільно-гідрофільні та гідрофільно-гідрофобні взаємодії відіграють головну роль в утворенні фібрил-білкових комплексів; ii) число фібрилярних взаємодіючих залишків незначно відрізняється для досліджуваних білків; iii) водневі зв'язки утворюються, головним чином, між глутаміном та аспарагіном фібрилярного інсуліну, лізином сироваткового альбуміну та аргініном лізоциму; iv) полярна занурена площа перевищує неполярну при комплексоутворенні білків з фібрилами інсуліну. Методом молекулярного докінгу були отримані докази локалізації фосфонієвого флуоресцентного барвника TDV на фібрил-білковому інтерфейсі.

**Ключові слова:** амیلлоїдні фібрили інсуліну; сироватковий альбумін; лізоцим; комплекс фібрила-білок; фосфонієвий зонд.

## ELECTRONIC CHIPS ACTING AS CAPACITORS OR INDUCTORS WHEN LASER ACT AS INFORMATION TRANSMITTER<sup>†</sup>

 **Mashair Ahmed Mohammed Yousef<sup>a\*</sup>, Abdullah Saad Alsubaie<sup>a</sup>,**  
 **Zoalnoon Ahmed Abeid Allah Saad<sup>b</sup>,  Mubarak Dirar Abd-Alla<sup>c</sup>**

<sup>a</sup>Department of Physics, College of Khurma University College, Taif University, Saudi Arabia

<sup>b</sup>Department of Physics, Faculty of Arts and Sciences, Dhahran Aljanoub, King Khalid University, Saudi Arabia

<sup>c</sup>Department of Physics, Faculty of Science, Sudan University of Science and Technology, Khartoum, Sudan

\*Corresponding Author: [mayousif@tu.edu.sa](mailto:mayousif@tu.edu.sa), [asubaie@tu.edu.sa](mailto:asubaie@tu.edu.sa), [zsaad@kku.edu.sa](mailto:zsaad@kku.edu.sa), P.O. Box 11099 Taif 21944

Received March 12, 2022; revised March 28, 2022; accepted May 6, 2022

To increase the speed of information flow and storage capacity in electronic devices laser can be used to carry information instead of electric current. Since the photon is faster than electrons, one expects information to be transmitted very fast through the internet when photons replace electrons. This requires searching for chips that act as capacitors, inductors or resistors. To do this Maxwell's equation for the electric field intensity beside the electron equation of motion were used. The electron is assumed to vibrate naturally inside a frictional medium in the presence of a local electric and magnetic fields. These equations have been used to find a useful expression for the absorption coefficient. The absorption coefficient was found to be dependent on the laser and natural frequencies beside the coefficient of friction in addition to the internal electric and magnetic fields. These parameters can be fine-tuned to make the chip act as a capacitor, inductor or resistor. The laser intensity decreases when the absorption coefficient increases. Thus, the absorption coefficient acts as an electric resistor. Therefore, if the absorption coefficient increases upon decreasing the frequency the chip acts as a capacitor. But when the absorption coefficient increases when the laser frequency increases the chip acts as an inductor. In the case that the absorption coefficient increases with the concentration of the carriers it acts in this situation as a resistor. For magnetic materials with magnetic flux density that cancels the frictional force, when the laser frequency is equal nearly to the atom's natural frequency the material acts as an inductor. But when the frictional force is low with the internal and external electric fields in phase, the material acts as a capacitor. However, it acts as a resistor for negligible natural frequency, when no electric dipoles exist and when the internal magnetic field force balance the frictional force.

**Key words:** laser; chip; capacitor; inductor; resistor.

**PACS:** 42.55.f

Electromagnetic waves (EMW) play an important role in our day life. They are oscillating electric and magnetic field propagating with the speed of light  $c$  in free space. The behavior of EMW is described by Maxwell's equations [1]. Light, laser, microwave, x-rays and gamma rays are electromagnetic waves used in a wide variety of applications. Radio and laser EMW are used in telecommunication, where they transmit information through the internet to mobile phones and computers [2]. Laser is used also in medicine in surgery and curing some diseases, beside other biological applications [3].

The utilization of EMW in telecommunication is the most commercially important to people. The rapid increase of people using network encourages scientists to search enabling the electronic chips to store very large number of bits and digits, beside fast transmission of information. These needs replacing electrons by faster particles to increase information flow. These particles also need to be smaller than electrons by many orders of magnitude to store more information. The particles that satisfy such requirements are photons [4]. Laser rays, which are photon streams, is suitable to be used to transmit and store information [5].

Different attempts were made to utilize laser in storing and transmitting information [6,7,8].

The work done by Christopher Monroe [3] speak about using laser in quantum computer to control floating atoms. This will enable computers to perform many calculations within almost no time. One particle can store many pieces of information [9]. This means that the behavior of atoms is on the atomic scale. The quantum laws thus control their behavior. Therefore, the control of such computers become a formidable task due to the probabilistic nature of the quantum systems. This problem can be surpassed by utilizing laser but using classical systems on the scale of more than 300nm, say on the micro scale. These needs using classical laws like Maxwell equations for laser electronic systems. Monroe informs us that in 2016 that for quantum electronic system ytterbium – 17 was used for qubits for particular states. Error – corrected universal reconfigurable ion trap quantum archetype) EURIQA began operating autonomously in April 2019 [9]. The work done by Vishal, et al [10], is concerned with using quantum laws to show how to use them for qubits and gates like Not and Xor gates.

The paper showed that the probabilistic nature of quantum laws allows storing very large number of information pieces of information but at the same time make the control of computer behavior very difficult [109]. In the work done by Julie change, et al [11], the cost was minimized for convolutional neural networks (CNNs) by incorporating a layer of optical computing prior to electronic computing. This system improves the accuracies of the optical system. The modeling of neural dynamics can be done with the aid of nonlinear optics. When the task of producing non-linearity is given to

<sup>†</sup> **Cite as:** M.A.M. Yousef, A.S. Alsubaie, Z.A.A.A. Saad, and M.D. Abd-Alla, East Eur. J. Phys. 2, 141 (2022), <https://doi.org/10.26565/2312-4334-2022-2-18>  
 © M.A.M. Yousef, A.S. Alsubaie, Z.A.A.A. Saad, M.D. Abd-Alla, 2022



electronic circuits in hybrid op to electronic circuit, the system will become more practical. This analogy is quite natural as far as the neuron cells functions are related to the electric pluses and bio photons [13,14,15]. The use of laser in electronic chips was realized by many researchers [16,17].

In the work done by Jin Li and others an optical gain op to electronic oscillator based on dual frequency integrated semiconductor laser was fabricated to generate high frequency micro and milli wave frequency. The device is dual semiconductor laser. The bandwidth was widened by introducing optical amplifier instead of electric one [18]. This means that laser electronic chips are now available. The rapid grow of topological photonics can give remarkable push to quantum computers. The discovery of quantum hall effect and topological insulators in condensed matter. The topological photonics using orbital angular momentum (OAM) can be used in optical quantum computer, routing and switching [19]. Many approaches and designs were suggested for quantum electronics [20,21,22]. However no intensive work or attention were played on designing laser capacitor or inductor although many researches were done for frequency dependent conductivity [23,24,25]. This paper is devoted for laser capacitors and inductor as shown in sections “Laser travelling in a resistive frictional medium” and “Laser electronic components for the electron equation of motion in the presence of local electric and magnetic fields beside thermal”. Sections “Discussion” and “Conclusion” are for discussion and conclusion.

### LASER TRAVELLING IN A RESISTIVE FRICTIONAL MEDIUM

Maxwell's equations describe the behavior of moving and static charges as well as electromagnetic waves (EMW). The electric field intensity  $E$  for a medium with electric permittivity and conductivity  $\epsilon$  and  $\sigma$  is given by

$$\nabla^2 E - \mu\epsilon \frac{\partial^2 E}{\partial t^2} - \mu\sigma \frac{\partial E}{\partial t} = 0, \quad (1)$$

where  $\mu$  is the magnetic permeability of the medium. Consider a solution in the form

$$E = E_0 e^{i(\omega t - \gamma_a z)} \quad (2)$$

Differentiating equation (2) with respect to space and time yields

$$\begin{aligned} \nabla^2 E &= -\gamma_a^2 E \\ \frac{\partial^2 E}{\partial t^2} &= -\omega^2 E \\ \frac{\partial E}{\partial t} &= +i\omega E \end{aligned} \quad (3)$$

Inserting equation (3) in (1) gives

$$(\gamma_a^2 + \mu\epsilon\omega^2 - i\omega\mu\sigma)E = 0 \quad (4)$$

Rearranging equation (4) gives

$$\gamma_a^2 = i\omega\mu\sigma - \mu\epsilon\omega^2 \quad (5)$$

For the electron moving with velocity  $v$  in a resistive medium of coefficient  $\gamma$ , under the action of the electric field  $E$ , the equation of motion of the electron is given by

$$m \frac{dv}{dt} = eE - \gamma v \quad (6)$$

Since  $E$  oscillates with time thus

$$E = E_0 e^{i\omega t} \quad (7)$$

In this case the electron also oscillates with velocity

$$v = v_0 e^{i\omega t} \quad (8)$$

Differentiating  $v$  in eqn (8) w.r.t time and inserting this result in equation (6) gives

$$\begin{aligned} im\omega v &= eE - \gamma v \\ [im\omega + \gamma]v &= eE \end{aligned} \quad (9)$$

Thus, the electron velocity is given by

$$v = \frac{e}{im\omega + \gamma} E = \frac{e(\gamma - im\omega)}{m^2\omega^2 + \gamma^2} E \quad (10)$$

For dielectric material the electric dipole moment (polarization) for  $n$  dielectric atoms per unit volume having distance  $x$  between the dipoles and charge  $q$  is given by

$$p = qnx \quad (11)$$

Thus, the current density  $J$  is given by [1]

$$J = \frac{dp}{dt} = qn \frac{dx}{dt} = qnv \quad (12)$$

Inserting eqn (10) in (12) and using the definition of the conductivity ( $\sigma = \sigma_1 + i\sigma_2$ ) yields

$$J = qn \frac{e(\gamma - imw)}{m^2w^2 + \gamma^2} E = \sigma E = (\sigma_1 + i\sigma_2)E \quad (13)$$

Thus, the real part  $\sigma_1$  and the imaginary part  $\sigma_2$  of the conductivity are given by

$$\sigma_1 = \frac{neq\gamma}{m^2w^2 + \gamma^2} \quad \sigma_2 = \frac{-mwneq}{m^2w^2 + \gamma^2} \quad (14)$$

One can simplify the expressions for  $\sigma_1$  and  $\sigma_2$  by adopting some approximations. For instance let

$$\gamma < mw \quad mw > \gamma \quad (15)$$

In this case equation (14) gives

$$\sigma_1 = \frac{neq\gamma}{m^2w^2} \quad \sigma_2 = \frac{-neqmw}{m^2w^2} = \frac{neq}{mw} \quad (16)$$

Since  $\gamma < mw$ , thus  $\sigma_1 < |\sigma_2|$

Numerically

$$\begin{aligned} neq\gamma &\sim n \times 10^{-38} \gamma \\ mw &\sim 10^{-30} \times 10^{15} \sim 10^{-15} \end{aligned} \quad (17)$$

$$\gamma \sim \frac{m}{\tau} \sim \frac{10^{-30}}{10^{-14}} \sim 10^{-16}$$

$$neqmw \sim n \times 10^{-38} \times 10^{-15} \sim n \times 10^{-51} \quad (18)$$

$$\sigma_2 \sim 10^{-23} n \quad (19)$$

$$|\sigma_2| > \sigma_1 \quad (20)$$

Since for visible light  $w \sim 10^{15}$

$$\mu\epsilon \sim \frac{1}{c^2} \sim 10^{-17}$$

Thus

$$\mu\epsilon w^2 \sim 10^{-17} \times 10^{30} \sim 10^{13} \quad (21)$$

Clearly, the above estimations show that

$$mw > \gamma \quad (22)$$

According to equations (16), (17), (18) and (5) with the fact that [1, 26]

$$\mu_0 = 4\pi \times 10^{-7} \sim 10^{-6} \text{ henry } m^{-1}$$

$$n \sim 10^{20}$$

$$e \sim q \sim 10^{-19} \quad (23)$$

$$\sigma_1 \sim \frac{10^{20} \times 10^{-38} \times 10^{-16}}{10^{-30}} \sim 10^{-4}$$

$$\sigma_2 \sim \frac{10^{20} \times 10^{-38}}{10^{-15}} \sim 10^{-3} \quad (24)$$

$$w\mu\sigma = w\mu\sigma_1 + iw\mu\sigma_2 \sim 10^{15} \times 10^{-6} \times 10^{-4} + i 10^{15} \times 10^{-6} \times 10^{-3} \sim 10^5 + i 10^6 \quad (25)$$

But

$$\mu\epsilon w^2 = \frac{w^2}{c^2} = \frac{10^{30}}{9 \times 10^{16}} \sim 10^{30} \times 10^{-17} \sim 10^{13} \quad (26)$$

Thus are can to a good approximation ignore both  $w\mu\sigma_1$  and  $w\mu\sigma_2$  compared to  $\mu\epsilon w^2$  in equation (5) to get

$$\gamma_a^2 = -\mu\epsilon w^2 = -\frac{w^2}{v^2} \tag{27}$$

$$\gamma_a = i \sqrt{\frac{w^2}{v^2}} = i \frac{w}{v} = i k \tag{28}$$

In view of eqn (2), one gets

$$E = E_0 e^{i(\omega t - kz)} \tag{29}$$

Which were sent a pure travelling wave with attenuation.

**LASER ELECTRONIC COMPONENTS FOR THE ELECTRON EQUATION OF MOTION IN THE PRESENCE OF LOCAL ELECTRIC AND MAGNETIC FIELDS BESIDE THERMAL**

The local field  $E_L$  can be induced when the external electric field displace atoms to form electric dipoles having dipole moment  $p$ . the local field strength is thus by

$$E_L = \alpha p = \alpha qnx, \tag{30}$$

where  $\alpha$  is a constant of proportionality  $q$  is the dipole charge,  $x$  is the displacement  $n$  is the atomic concentration. Thus, the equation of motion is given by

$$m \frac{dv}{dt} = eE + E_L - \gamma v - k_0 x = eE + \alpha qnx - \gamma_0 v + Bev - mw_0^2 x \tag{31}$$

$$\gamma = \gamma_0 - Be, \tag{32}$$

where  $B$  is the magnetic flux density of the internal field and  $k_0 x$  is the thermal vibration force. Again the velocity can become.

$$v = v_0 e^{i\omega t} \tag{33}$$

Integrating both sides yields

$$x = \int v dt = \frac{v}{i\omega} = -\frac{iv}{\omega}, \tag{34}$$

where  $x$  is the displacement. The differentiation gives

$$\frac{dv}{dt} = i\omega v \tag{35}$$

Inserting eqns (34) (35) in (31) gives

$$imw v = eE - \frac{\alpha qn}{w} iv - \gamma v + \frac{imw_0^2 v}{w}$$

$$[i[m(\omega^2 - w_0^2) + \alpha qn] + \gamma w]v = ewE \tag{36}$$

For simplicity and to gain time as well as ink and paper one can define

$$\beta = m\omega^2 + \alpha qn - m w_0^2 = m(\omega^2 - w_0^2) + \alpha qn \tag{37}$$

$$\gamma = \gamma_0 - Be \tag{38}$$

Thus, eqn (36) becomes

$$[i\beta + w\gamma]v = ewE \tag{39}$$

Hence, the velocity  $v$  is given by

$$v = \frac{ew}{(w\gamma + i\beta)} E \tag{40}$$

The current density resulting from dipole oscillation is thus given by

$$J = \frac{dp}{dt} = qn \frac{dx}{dt} = qnv \quad (41)$$

In view of equation (40) one gets

$$J = \frac{eqnw(w\gamma - i\beta)}{w^2\gamma^2 + \beta^2} E = \sigma E = (\sigma_1 + i\sigma_2) E \quad (42)$$

Thus the real and imaginary conductivities are given by

$$\sigma_1 = \frac{eqnw^2\gamma}{w^2\gamma^2 + \beta^2} \quad (43)$$

$$\sigma_2 = \frac{-\beta e n q w}{w^2\gamma^2 + \beta^2} \quad (44)$$

If we select a material with weak internal field, and when we consider the case when the frequency  $w$  equal to  $w_o$ . Thus

$$w \gamma > \beta \quad (45)$$

There fore

$$w^2 \gamma^2 + \beta^2 \approx w^2 \gamma^2 \quad (46)$$

One is concerned with dipole current according to eqn (41). Thus, the mass of vibrating atoms  $m$  and  $w$  for visible light have the orders

$$m \sim 10^{-26} \quad w \sim 10^{15} \quad (47)$$

Hence

$$\beta \sim 10^{-26} \times 10^{30} \sim 10^4 \quad (48)$$

Also

$$w\gamma \sim 10^{15}\gamma \quad (49)$$

$$w\gamma > \beta \quad \beta < w\gamma \quad (50)$$

This requires

$$\gamma > 10^{-11} \quad (51)$$

The value of  $\gamma$  ( $\gamma = m/\tau$ ) for the element *Bi* exceeds  $10^{-11}$  [26]. Thus the oscillating dipole should have friction more than that of the element *Bi*. In this case

$$\sigma_1 = \frac{e q n}{\gamma} \quad (52)$$

$$\sigma_2 = -\frac{\beta e n q w}{\gamma^2 w^2} = -e n q \frac{\beta}{w\gamma^2} = -\sigma_1 \frac{\beta}{w\gamma} \quad (53)$$

$$|\sigma_2| < \sigma_1 \quad (54)$$

Thus one can neglect the imaginary conductivity to get

$$\sigma_2 \sim 0$$

According to eqns (53), (54) and (5)

$$\gamma_a^2 = i\mu \frac{weqn}{\gamma} - \mu\epsilon w^2 = \mu w \left( \frac{ieqn}{\gamma} - \epsilon w \right) = \mu w (i \times 10^{-38} \times 10^{11} \times 10^{20} - 10^{15} \times 10^{-11}) = \mu w (10^{-7}i - 10^4) \quad (55)$$

Thus

$$\gamma_a^2 \approx -\mu \epsilon w^2 = -\frac{w^2}{v^2} = -k^2$$

$$\gamma_a = i k \quad (56)$$

In view of eqn (2) is a travelling wave in the form

$$E = E_o e^{i(\omega t - kZ)} \tag{57}$$

This wave is un attenuated. Now consider the resonance condition with no local field, i.e

$$\omega = \omega_o \quad \alpha = o \tag{58}$$

In this case eqn (37) gives

$$\beta = 0 \tag{59}$$

Thus eqns (43) and (44) gives

$$\sigma_1 = \frac{e n q}{\gamma} \tag{60}$$

$$\sigma_1 = 0 \tag{61}$$

In view of equation (38)

$$\gamma = \gamma_o - B_e \tag{62}$$

If one make the internal magnetic field by doping the sample with magnetic dipoles such that

$$\gamma_o - B_e \tag{63}$$

In order to make

$$\gamma \sim 10^{-60} \tag{64}$$

In this case equation (60) gives

$$\sigma_1 \sim 10^{22} n \tag{65}$$

Since

$$\mu \varepsilon \omega^2 \sim 10^{13} \tag{66}$$

Thus one can neglect the last term in eqn (5) to get [see eqns (61) , (65) , (66)]

$$\gamma_a^2 = i \omega \mu \sigma_1 = (e^{90})^i \omega \mu \sigma_1 \tag{66}$$

Thus

$$\begin{aligned} \gamma_a &= e^{45i} \sqrt{\omega \mu \sigma_1} \\ \gamma_a &= \left( \frac{1}{\sqrt{2}} + \frac{i}{\sqrt{2}} \right) \sqrt{\omega \mu \sigma_1} \end{aligned} \tag{67}$$

A direct substitution of eqn (67) in eqn (2) gives

$$\begin{aligned} E &= E_o e^{i\left(\omega t - \frac{\sqrt{\omega \mu \sigma_1}}{\sqrt{2}} Z\right)} e^{\frac{\sqrt{\omega \mu \sigma_1}}{2} Z} \\ E &= E_o e^{\frac{\sqrt{\omega \mu \sigma_1}}{\sqrt{2}} Z} e^{i\left(\omega t - \frac{\sqrt{\omega \mu \sigma_1}}{\sqrt{2}} Z\right)} \end{aligned} \tag{69}$$

Thus the attenuation (absorption) coefficient becomes

$$\alpha = \frac{\sqrt{\omega \mu \sigma_1}}{\sqrt{2}} \tag{70}$$

Increases with the frequency. This means that the resistance of the medium to the radiation increases upon increasing frequency. This behavior resembles that of an inductor, which has resistance ( $x_L = \omega L$ ) increasing with frequency. This means that the medium behaves in this case as an inductor.

Another case can be considered by doping the chip with magnetic dipole atoms such that

$$\gamma = \gamma_o - B_e = o \tag{71}$$

In this case eqns (43) and (44) gives

$$\sigma_1 = 0 \quad \sigma_2 = \frac{-enqw}{\beta} \quad (72)$$

In view of equation (37)

$$\beta = m(w^2 - w_o^2) + \alpha q n \quad (73)$$

$\beta$  can also be adjusted by doping the chip with electric dipoles and selecting atoms having natural frequency  $w_o$  or alternatively when no electric dipole exist, with the laser frequency fine-tuned such that

$$\beta \sim 10^{-60} \quad (74)$$

In this case equation (72) gives

$$\sigma_2 \sim 10^{22} nw \quad (75)$$

Thus with the aid of equations (17) and (23)

$$w\mu\sigma_2 \sim 10^{30} \times 10^{-6} \times 10^{22}n \sim 10^{46} n \quad (76)$$

In view of equations (5), (21), (72) and (76), one can neglect all terms except the term (76) to get

$$\gamma_a^2 = -w\mu\sigma_2 = \frac{w^2\mu enq}{\beta} = C_o^2 w^2 \quad (77)$$

Therefore

$$\gamma_a = C_o w \quad (78)$$

Where

$$C_o^2 = \frac{\mu enq}{\beta} \quad (79)$$

A direct substitution of eqn (79) in (2) gives

$$E = E_o e^{-C_o w z} e^{i(wt)} \quad (80)$$

This equation represents an oscillating wave with amplitude diminishes with distance  $z$  and angular frequency  $w$ . Thus the resistance of the medium to the wave increases with frequency. Thus, this medium acts as an inductor. This medium also allows intalgenment as far as

$$K = \frac{2\pi}{\lambda} = 0 \quad (81)$$

Thus the wave speed is

$$v = \frac{w}{k} \rightarrow \infty \quad (82)$$

Another approach can be tackled using equation (5) by considering a travelling diminished wave. This requires defining  $\gamma_a$  to be in the form

$$\gamma_a = ik + \gamma_{oa} \quad (83)$$

Where conductivity  $\sigma$  and electric permittivity are complex

$$\begin{aligned} \sigma &= \sigma_1 + i\sigma_2 \\ \varepsilon &= \varepsilon_1 + i\varepsilon_2 \end{aligned} \quad (84)$$

Thus a direct substitution of equations (83) and (84) in eqn (5) gives

$$\gamma_a^2 = -k^2 + \gamma_{oa}^2 + 2k\gamma_{oa}i = iw\mu\sigma_1 - w\mu\sigma_2 - \mu\varepsilon_1 w^2 - i\mu\varepsilon_2 w^2$$

Since the wave number  $k$  is given by

$$k = \frac{w}{v} = w\sqrt{\mu\varepsilon_1} \tag{85}$$

Then the two terms cancel out on both sides. Equating real and imaginary parts give

$$\gamma_{oa}^2 = -w\mu\sigma_2 \qquad \gamma_{oa} = \sqrt{-w\mu\sigma_2} \tag{86}$$

$$2k\gamma_{oa} = w\mu\sigma_1 - \mu\varepsilon_2w^2$$

$$\gamma_{oa} = \frac{w\mu\sigma_1 - \mu\varepsilon_2w^2}{2k} \tag{87}$$

For elements like Ag and Cu with  $\tau \sim 10^{-14}$  at 273 K [26]

$$m \sim 10^{-30} \qquad w \sim 10^{15} \qquad \gamma \sim \frac{m}{\tau} \sim 10^{-30} \times 10^{14} \sim 10^{-16}$$

$$mw \sim 10^{-15} \tag{88}$$

Therefore

$$mw > \gamma \tag{89}$$

Thus equations (14) and (89) gives

$$\sigma_1 = \frac{neq\gamma}{m^2w^2} \tag{90}$$

$$\sigma_2 = \frac{-mw eq}{m^2w^2} = -\frac{neq}{mw} \tag{91}$$

Inserting eqn (91) in (86) gives

$$\gamma_{oa} = \sqrt{\frac{neq\mu}{m}} \tag{92}$$

Inserting also eqn (90) in (87)

$$\gamma_{oa} = \frac{\left(\frac{neq\gamma\mu w}{m^2w^2}\right) - \mu\varepsilon_2w^2}{2k} \tag{93}$$

When the internal local polarized field is in the same direction and in phase with the external field

$$\varepsilon = \varepsilon_1 \qquad \varepsilon_2 = 0 \tag{94}$$

$$\gamma_{oa} = \frac{neq\gamma\mu}{2m^2kw} \tag{95}$$

The term in equation (92) can be made similar to that of eqn (95) by

$$\mu\varepsilon = \frac{1}{v^2} = \frac{k^2}{w^2} \tag{96}$$

Thus inserting equation (96) in (92) gives

$$\gamma_{oa} = \sqrt{\frac{neq\mu\varepsilon}{m\varepsilon}} = \sqrt{\frac{neq}{m\varepsilon v^2}} = \sqrt{\frac{neqk^2}{m\varepsilon w^2}} = \frac{k}{w} \sqrt{\frac{neq}{m\varepsilon}} \tag{97}$$

Therefore equations (97) and (83) inserted in (2) gives

$$E = E_0 e^{-\frac{k}{w} \sqrt{\frac{neq}{m\varepsilon}} Z} e^{i(\omega t - kZ)} \tag{98}$$

Equation (98) represent a travelling wave attenuated with distance Z. the attenuation rate increases upon decreasing the frequency. This means that the medium resistance to the wave increases when the frequency decreases.

Therefore, the medium, which is doped with electric polarized atoms or molecules, with low mechanical resistance act as a capacitor for electric circuits, where the capacitor resistance  $\left(xc = \frac{1}{wc}\right)$  increases when the frequency decreases.

However for elements like  $Bi$  with  $\tau \sim 10^{-16}$  [26], the friction coefficient takes the form

$$\gamma \sim \frac{m}{\tau} \sim 10^{-30} \times 10^{16} \sim 10^{-14} \quad (99)$$

Thus

$$\gamma > mw \quad (100)$$

This since ( $m w \sim 10^{-15}$ ), in the case of copper the relaxation time [1] is of the order  $\tau \sim 10^{-19}$ . Thus

$$\gamma \sim \frac{m}{\tau} \sim 10^{-30} \times 10^{19} \sim 10^{-11}$$

The frictional term is thus much larger than the term  $mw$ , i.e.

$$\gamma \gg mw \quad (101)$$

Thus equation (14) gives

$$\sigma_1 = \frac{neq}{\gamma} \quad \sigma_2 = -\frac{meqmw}{\gamma^2} \quad (102)$$

In view of equation (86) the insertion of the imaginary conductivity gives

$$\gamma_{oa} = \frac{w}{\gamma} \sqrt{neqm\mu} \quad (103)$$

For real dielectric constant when the internal and external fields are in phase

$$\varepsilon_1 = \varepsilon \quad \varepsilon_2 = 0 \quad (104)$$

Thus inserting the real conductivity in eqn (102), together with (104) in (87) gives

$$\gamma_{oa} = \frac{w}{\gamma} \frac{neq\mu}{2k} \quad (105)$$

Thus inserting eqns (105) and (83) in eqn (2) gives

$$E = E_o e^{-\frac{w}{\gamma} \frac{neq\mu}{2k} z} e^{i(\omega t - kz)} \quad (106)$$

This equation represent a travelling wave facing resistance proportional to the frequency. Thus this chip, doped with materials that polarize themselves in the direction of the external electric field, acts as an inductor.

The chip can acts as a resistor, when using equations (37), (38) and (39). When the internal field  $B$  is adjusted by doping the chip with magnetic material such that [see (38)]

$$\gamma = \gamma_o - Be = 0 \quad (107)$$

i.e

$$B = \frac{\gamma_o}{e} \quad (108)$$

When also electric dipoles that generate internal field are present

$$\alpha = 0 \quad (109)$$

Neglecting also thermal agitation when one cool the thin film or dope it with very strong bond which prevents electrons and atoms vibrations. In this case

$$\omega o \approx 0 \quad (110)$$

Thus equation (37) gives



$$\beta = m \omega^2 \tag{111}$$

In view of equation (39) one gets

$$v = -\frac{i\omega e}{m\omega^2} E = -\frac{ie}{m\omega} E \tag{112}$$

Using the formal definition of the current density

$$J = nev = -\frac{ine^2}{m\omega} E = (\sigma_1 + i\sigma_2)E \tag{113}$$

Thus, the real and imaginary conductivities are given by

$$\sigma_1 = 0 \qquad \sigma_2 = -\frac{ne^2}{m\omega} \tag{114}$$

Using equation (86) yields

$$\gamma_{oa} = \sqrt{\frac{ne^2\mu}{m}} = e \sqrt{\frac{n\mu}{m}} \tag{115}$$

This equation represents an attenuated travelling wave with attenuation and resistance proportional to the concentration of the doped material  $n$ . This indicates that the chip acts here as an ordinary resistor.

### DISCUSSION

The magnetic and electrical properties of the materials or the impurities added to the host substrate determine completely and affect the laser propagation inside electronic laser chips. Section (2) shows that for a medium which has only mechanical resistance, such that the atoms are in the form of dielectrics equations (10), (12), (14) and (15) beside equation (29) show that such dielectric material enables laser waves to travel without any attenuation. Thus this material act as a conducting wire which connect electronic components with each other.

The dream of scientists to use laser instead of electrons in integrated circuits and electronic chips can be realized if certain conditions are satisfied.

According to equation (5) the attenuation coefficient reflects the resistance of the medium to the laser or electromagnetic radiation. Large attenuation coefficient reflects high resistance, while low coefficients reflects low resistance. This means that also when the attenuation coefficient is directly proportional to the frequency the medium acts as an inductor, which has resistance ( $X_L = \omega L$ ). Nevertheless, when the attenuation coefficient is inversely proportional to the frequency the medium acts as a capacitor, which has resistance ( $X_c = 1/(\omega c)$ ).

The dependence of the attenuation coefficient on the frequency is through the conductivity  $\sigma$  as shown by equations (5) and (14). The interaction of the medium with EMW manifests itself through the electron equation of motion (31), beside equations (37) and (38). This interaction manifests itself through conductivity as shown by eqns (43) and (44). The properties of the medium that affect the attenuation coefficient through the conductivity  $\sigma$  are the local magnetic field  $B$  beside the local electric field  $\propto qn$  in an edition to the natural vibration frequency  $\omega_0$  and friction coefficient  $\gamma$ . Equations (58 – 70) shows that when the laser frequency is equal to the natural medium frequency, and in the absence of a local electric field, by adjusting the magnetic internal field to can cell out (see (64)) and to be just less than the friction force, in this case the attenuation coefficient is directly proportional to the frequency. Thus, the medium act as an inductor in this situation (see eqn (70)). However, when the magnetic force exactly can cell out friction force as shown by eqn (71), with laser frequency equal to the natural frequency, for very low doping with dielectric or electric dipoles that having very weak local field, the medium acts again as an inductor as shown by eqn (80).

Another approach can be tried by assuming the laser as a travelling wave with attenuation coefficient  $\gamma_{oa}$  as shown by eqn (83).

When one has elements like Ag and cu with relaxation time  $t \sim 10^{-13}$  or more the attenuation coefficient is inversely proportional to the frequency (see (97)). The medium thus acts as a capacitor.

However, for elements like Bi with  $t \sim 10^{-16}$  or less (see eqn (99)), the medium doped with Bi acts as an inductor as shown by eqns (105, 106).

The chip acts also as a resistor for nonelectric, non-oscillating atoms medium having internal field force exactly cancelling the frictional force (see eqns (107 – 116)).

### CONCLUSION

Using Maxwell's equations and the electron and dipole equation of motion it was shown that chips fabricated from some materials act as conductor or capacitor or resistor. For laser or light frequency nearly equal to the natural frequency, such that the local magnetic force just cancels the frictional force, in this case the material act as an inductor. The chip acts as a capacitor for nonmagnetic material with negligible natural frequency and high mobility electric dipole, which align itself in the external electric field completely. The chip also acts as a resistor for non-dielectric, nonmagnetic material with negligible natural frequency when its relaxation time exceeds  $10^{-14}$  second.

### Acknowledgments


The authors would like to acknowledge the financial support of Taif University Researchers Supporting Project number (TURSP-2020/189), Taif University, Taif, Saudi Arabia


**Authors Note.** All authors contributed equally to this work

**Conflicts of Interest.** The authors declare no conflicts of interest regarding the publication of this paper.

**Funding.** The funding support of this paper is from the authors of this paper themselves.

### ORCID IDs

 Mashair Ahmed Mohammed Yousef, <https://orcid.org/0000-0002-5641-4849>

 Zoalnoon Ahmed Abeid Allah Saad, <https://orcid.org/0000-0002-6722-7061>

 Mubarak Dirar Abd-Alla, <https://orcid.org/0000-0002-2036-320X>

### REFERENCES

- [1] P. Lorrain, and D.R. Corson, *Electromagnetic fields and waves*, (W.H. Freeman and company, San Francisco, 1970).
- [2] A.S. Sedra, and K.C. Smith, *Micro electronic circuit*, (Oxford University press, New York, 1998).
- [3] M.A. Haimid, A.A.S. Marouf, and M.D. Abdalla, Helium – Neon Laser Effects on Human whole Blood by spectroscopy in vitro study, *Asian Journal of Physical and Chemical Sciences*, **7**, 1 (2019), <https://www.journalajopacs.com/index.php/AJOPACS/article/view/29706>
- [4] A.N. Matveev, *Optics*, (Mir, Moscow, 1988).
- [5] L. Maleki, “The Optoelectronic Oscillator”, *Nat. Photonics*, **5**(12), 728 (2011), <https://doi.org/10.1038/nphoton.2011.293>
- [6] H.-K. Sung, X. Zhao, E.K. Lau, D. Parekh, C.J. Chang-Hasnain, and M.C. Wu, “Optoelectronic oscillators using direct modulated semiconductor lasers under strong optical injection”, *IEEE Journal of Selected Topics in Quantum Electronics*, **15**(3), 572 (2009), <https://doi.org/10.1109/JSTQE.2008.2010334>
- [7] H.K. Sung, *Modulation and dynamical characteristics of high speed semiconductor laser subject to optical injection*, (2003).
- [8] H.G. Abed, K.A. Hubeatira, and K.A.AI. Namicee, “Spiking control in Semiconductor laser with Ac-coupled opto electronic feedback”, *Australian Journal of Basic and Applied Sciences*, **9**(33), 417 (2015), <http://www.ajbasweb.com/old/ajbas/2015/October/417-426.pdf>
- [9] C. Monroe, “Remote quantum computing is the future”, *Nature*, **583**, (2020), <https://media.nature.com/original/magazine-assets/d41586-020-01937-x/d41586-020-01937-x.pdf>
- [10] Mr. S.M. Gandhi, and Mr. V.R. Gotarane, “Quantum computing: Future computing”, *International Reaserch Journal of Engineering and Technology (IRJET)*, **3**(2), 1377 (2016), <https://www.irjet.net/archives/V3/2/IRJET-V3I2246.pdf>
- [11] J. Chang, V. Sitzmann, X. Dun, W. Heidrich, and G. Wetzstein, “Hybrid optical – electronic convolutional neural networks with optimized diffractive optics for image classification”, *Scientific Reports*, **8**, 12324 (2018), <https://doi.org/10.1038/s41598-018-30619-y>
- [12] K.S. Hung, K.M. Curtis, and J.W. Orton, “Optoelectronic implementation of multifunction cellular neural network”, *IEEE Transactions on Circuits and Systems II: Analog and Digital Signal Processing*, **43**(8), 601 (1996), <https://doi.org/10.1109/82.532007>
- [13] J. Conhen, N.T.K. Vo, D.R. Chettle, F.E. McNeill, C.B. Seymour, and C. Mothersill, “Quantifying Biophoton Emissions From Human Cells Directly Exposed to Low-Dose Gamma Radiation”, *Dose Response*, **18**(2), (2020), <https://doi.org/10.1177%2F1559325820926763>
- [14] J.B. Kent, Li. Jin, and X.J. Li, “Quantifying Biofield Therapy through Biophoton Emission in a cellular”, *Model Journal of Scientific Exploration*, **34**(3), 434 (2020), <https://dx.doi.org/10.31275%2F20201691>
- [15] T. Yoshii, M. Ikeaa, and I. Hamachi, “Two-photon – responsive supramolecular Hydrogel for controlling materials motion in Micrometer space”, *Angew. Chem.* **126**(28), 7392 (2014), <https://doi.org/10.1002/ange.201404158>
- [16] J. Li, J. Zheng, T. Pu, Y. Zhang, Y. Li, X. Meng, and X. Chan, “Monolithically integrated multi-section semiconductor lasers: towards the future of integrated microwave photonics”, *Optic*, **226**(1), 165724 (2021), <https://doi.org/10.1016/j.ijleo.2020.165724>
- [17] X. Zhang, T. Pu, J. Zheng, Y. Zhang, Y. Shi, H. Zu, Y. Li, J. Li, and X. Chen, “A simple frequency tunable opto electronic osullator using an indegrated multi section distributed feedback semiconductor laser”, *Optics Express*, **27**(5), 7036 (2019), <https://doi.org/10.1364/OE.27.007036>
- [18] J. Li, T. Pu, J. Aheng, Y. Zhang, Y. Shi, W. Shao, X. Zhang, X. Meng, J. Liu, J. Liu, and X. Feichen, “All – optical gain opto electronic oscillator based on a dual- frequency integrated semiconductor laser: potential to speak the band width limitation in the traditional OEO confugration”, *Optics Express*, **29**(2), 1064 (2021), <https://doi.org/10.1364/OE.415429>
- [19] A. Manzalnic, *Topological photonics for optical communications and quantum reports*, **2**(4), 579 (2020), <https://doi.org/10.3390/quantum2040040>
- [20] T. Rudolph, “Why I am optimistic about the silicon route to quantum computing”, *APL photonics*, **2**, 030901 (2017), <https://doi.org/10.1063/1.4976737>
- [21] A.S. Cacciapuoti, M. Caleffi, R. Van Meter, and L. Hanzo, “When entanglement meets classical communications: quantum teleportation for the quantum Internet”, *IEEE Trans commun*, **6**, 3808 (2020), <https://doi.org/10.1109/TCOMM.2020.2978071>
- [22] G. Jaeger, D.S. Simon, and A.V. Sergienko, “Topological qubits as carried of quantum information in Optics”, *Appl. Sci.* **9**, 575 (2019), <https://doi.org/10.3390/app9030575>
- [23] N.I.A. Elbadawi, M.D. Abdallah, R. AbdElhai, and S.A.E. Ahmed, “The Effect of oxidation Number on Refractive index based on string theory”, *International Journal of Engineering Sciences & Research Technology*, **7**(1), 122 (2018), <https://www.academia.edu/download/55466191/104.pdf>
- [24] N.I.A. Elbadawi, M.D. Abdallah, R. AbdElhai, and S.A.E. Ahmed, “The dependence of absorption coefficient on Alomic and oxidation number for some Elements according to string theory”, *International Journal of Engineering Sciences & Research*, **7**(1), 130 (2018), <https://www.academia.edu/download/55466195/105-.pdf>
- [25] S.A.E. Ahmed, and M.D. Abd-Alla, “Light induced current using Quantum Mechanical Approaches”, *Journal of Applied and industrial Sciences*, **1**(1), 16 (2013), <https://citeseerx.ist.psu.edu/viewdoc/download?doi=10.1.1.1049.2908&rep=rep1&type=pdf>
- [26] Gerald Burns, *Solid state physics*, (Academic press, Orlando, 1989).

**ЕЛЕКТРОННІ ЧИПИ, ЩО ДІЮТЬ ЯК КОНДЕНСАТОРИ АБО ІНДУКТОРИ,  
КОЛИ ЛАЗЕР ДІЄ ЯК ПЕРЕДАВАЧ ІНФОРМАЦІЇ**  
Машайр Ахмед Мохаммед Юсеф<sup>а</sup>, Абдулла Саад Алсубай<sup>а</sup>, Золнун Ахмед Абейд Аллах Саад<sup>б</sup>,  
Мубарак Дірар Абд-Алла<sup>с</sup>

<sup>а</sup>Фізичний факультет, коледж університету Хурма, університет Таїф, Саудівська Аравія

<sup>б</sup>Фізичний факультет, факультет мистецтв і наук, Дахран Аджануб, Університет короля Халіда, Саудівська Аравія

<sup>с</sup>Фізичний факультет, факультет природничих наук Суданського університету науки і техніки, Хартум, Судан

Для збільшення швидкості потоку інформації і ємності пам'яті в електронних пристроях для перенесення інформації замість електричного струму можна використовувати лазер. Оскільки фотон швидший за електрони, очікується, що інформація буде передаватися дуже швидко через Інтернет, коли фотони замінять електрони. Це вимагає пошуку мікросхем, які діють як конденсатори, індуктори або резистори. Для цього було використано рівняння Максвелла для напруженості електричного поля поряд з електронним рівнянням руху. Вважається, що електрон вібрує природним чином всередині середовища з тертям в присутності локального електричного та магнітного полів. Ці рівняння були використані для пошуку корисного виразу для коефіцієнта поглинання. Було виявлено, що коефіцієнт поглинання залежить від частоти лазера та власних поряд з коефіцієнтом тертя на додаток до внутрішніх електричних та магнітних полів. Ці параметри можна точно налаштувати, щоб мікросхема діяла як конденсатор, індуктивність або резистор. Інтенсивність лазера зменшується при збільшенні коефіцієнта поглинання. Таким чином, коефіцієнт поглинання діє як електричний резистор. Отже, якщо коефіцієнт поглинання збільшується при зменшенні частоти, мікросхема діє як конденсатор. Але коли коефіцієнт поглинання збільшується при підвищенні частоти лазера, мікросхема діє як індуктор. У випадку, коли коефіцієнт поглинання зростає з концентрацією носіїв, він виступає в цій ситуації як резистор. Для магнітних матеріалів із щільністю магнітного потоку, яка скасовує силу тертя, коли частота лазера дорівнює майже власній частоті атома, матеріал діє як індуктор. Але коли сила тертя низька з внутрішнім і зовнішнім електричними полями в фазі, матеріал діє як конденсатор. Однак він діє як резистор для незначної власної частоти, коли не існує електричних диполів і коли сила внутрішнього магнітного поля врівноважує силу тертя.

**Ключові слова:** лазер, мікросхема, конденсатор, індуктор, резистор

## SOLUTIONS OF THE SCHRÖDINGER EQUATION WITH HALO NEUTRON POSITION FOR BETA ( $\beta^-$ ) DECAY AND NEUTRON EMISSION<sup>†</sup>

 **Waleed S. Hwash**

*Department of Physics, Faculty of Education for Pure Sciences, University of Anbar, Anbar, Iraq  
School of Applied Physics, Faculty of Science and Technology, University Kebangsaan Malaysia  
43600 Bangi, Selangor, Malaysia  
E-mail: [waleed973@yahoo.com](mailto:waleed973@yahoo.com)*

Received April 16, 2022; revised May 26, 2022; accepted May 26, 2022

The current study is about the structure of  $^{17}\text{B}$ , which has been investigated by the Microscopic Cluster Model. The binding energy and neutron position of two valence neutrons of Beta-decay and neutron emission have been calculated. A cluster configuration of the Halo nucleus inspired me to consider all radioisotopes have cluster configuration before the decay process. The Jacobi coordinates has been used to investigated the  $^{17}\text{B}$  nucleus. The Jacobi coordinate is a very well technique to describe such as a three-body system or halo structure. The  $^{17}\text{B}$  has Borromean property, so it has been defined in T-configuration in this coordinates. The angle in the figure defines an angle of halo neutron motion around the core. The study has considered a deformation of the core as a high influence on the binding of the valence neutrons.

**Keywords:**  $^{17}\text{B}$ ; neutron-halo structure;  $\beta^-$ -decay; neutron emission; microscopic cluster model.

**PACS:** 21.45.+v, 21.60.gx

There are many works have been done in investigates of nuclei away from the line of  $\beta$ -stable through the beginning of new facilities and technologies. Experimental studies [1–3] on light atomic nuclei have shown exotic large r.m.s. radius and specifically [4] that has ascribed this to the halo property. Halo structure is defined as the effect of threshold that happens in weakly bound nuclei where the nucleons are connected in very small-range potential. The halo atomic nuclei are confined as more loosely.

The three-body halo nuclei of choice with two neutrons move around the core are drip-line of light nuclei, the ( $^{17}\text{B} = ^{15}\text{B} + n + n$ ) nucleus. Actually, the first observation of (Boron-17) is in 1973 [5], interest of the Boron  $^{17}\text{B}$  nucleus is exotic properties (neutron emission and  $\beta$ -decayed [6] and an abnormal radius [7,8]). The very large matter radius is a significance of a halo, formed by external nucleons far from a core that increases meaningfully the matter radius [9].

Many studies have been done using the microscopic cluster model and the three-body models [10,11] of  $^{17}\text{B}$  depending on different configurations of  $^{15}\text{B} + \text{di-neutron} + \text{di-neutron}$ . The wavefunction was built on the shell of lp with the excitations of the core on the harmonic-oscillator. The angular momentum and parity of  $^{17}\text{B}$  have been investigated. The R.M.S. radius and electric quadrupole of (Boron-17) were observed to be around 2.81 fm and around 2.74 e.fm<sup>2</sup>, without the  $^{15}\text{B} + n + n$  configuration [11]. Ren and Xu [12] investigated the  $^{17}\text{B}$  ground state with a three-body model including two neutrons and  $^{15}\text{B}$  core. Ren and Xu have calculations regarding a  $^{15}\text{B} + n$  interaction that was complicated and explained about the large RMS radius. The shell model spectrum of several boron isotopes has also been used by Warburton and Brown has used several Boron isotopes by the shell model. [13]

Several experimental studies on  $^{17}\text{B}$  have been achieved [14, 15]. The separation energy of two neutrons ( $S_{2-n}$ ) was 1.39 MeV $\pm$ 0.14 MeV for  $^{17}\text{B}$  [14] while the radius of  $^{17}\text{B}$  was 4.10 fm $\pm$ 0.46 fm [8] and 3.0 fm $\pm$ 0.6 fm [16] by Ozawa in 1993. The abnormal large radius has been taken as a halo structure and loosely bound. The halo phenomenon (especially, the neutron-halo nuclei) is fairly common in nuclei and with high  $N/Z$  ratios which lead to  $\beta$ -decay and neutron emissions. The weakening in the correlation of p-n distribution is a typical of the stable nuclei [17]. In this approach, the skin nucleons can be released from the nuclei to form  $\beta$ -decay and neutron emissions and move away freely from the other nucleons. The deformation or the core electric quadrupole moment as predicted by the shell model that caused by nucleons outside a close closed shell. [18].

In the current work, the Boron-17 was investigated to determine where is the position of valence neutron to start  $\beta$ -decay or neutron emissions by using the Microscopic Cluster Model. The hyperspherical harmonic method has been used to solve the model. The core was considered deformed and this deformation has a high role in determining the position of decay. The protons and neutrons far from the magic number in the core shaped the deformations. Thus, the deformation has a clear influence on the energy of valence neutrons. The Jacobi coordinates were space coordinates of  $^{17}\text{B}$  nucleus which were used in this calculation, as formerly used for  $^{14}\text{Be}$  [21] and  $^{11}\text{Li}$  [22].

### THEORETICAL ASPECT

The Jacobi coordinates has been used to investigate the  $^{17}\text{B}$  nucleus. The Jacobi coordinate is a very well technique to describe such as a three-body system or halo structure as in Fig. 1. The  $^{17}\text{B}$  has Borromean property [23], so it has

<sup>†</sup> Cite as: W.S. Hwash, East Eur. J. Phys. 2, 153 (2022), <https://doi.org/10.26565/2312-4334-2022-2-19>

© W. Hwash, 2022

been defined in T-configuration in this coordinates. The angle in the figure defines an angle of halo neutron motion around the core.

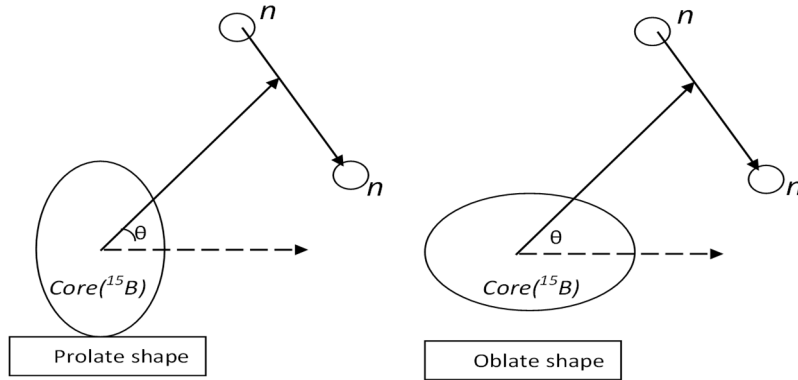


**Figure 1.** Jacobi coordinates for free-body system with two shapes of the core and angle of two-halo neutrons

The halo structure was defined as the core plus valence neutrons. The total wavefunction of the system is:

$$\Psi^{JM}(x, y, \xi) = \phi_{core}(\xi_{core})\psi(x, y) \tag{1}$$

The Hamiltonian of the core is given as

$$\hat{h}_{core}(\xi_{core})\phi_{core}(\xi_{core}) = \epsilon_{core}\phi_{core}(\xi_{core}) \tag{2}$$

The angular part, the radial part, and spin of the valence neutrons have been included in  $\psi(x,y)$ .

The relationship between the coordinates  $(x, y)$  and the hyperspherical coordinates (hyper-radius  $\rho$  and hyper-angle  $\theta$ ) as

$$\rho^2 = x^2 + y^2 \quad \text{and} \quad \theta = \arctan\left(\frac{x}{y}\right)$$

Hyperspherical expansion is

$$R_n(\rho) = \frac{\rho^{\frac{3}{2}}}{\rho_o^3} \sqrt{\frac{n!}{(n+5)!}} L_{nlag}^5(z) \exp\left(\frac{-z}{2}\right) \tag{3}$$

$$z = \rho / \rho_o \quad \text{and} \quad \psi_k^{l_x l_y}(\theta) = N_k^{l_x l_y} (\sin \theta)^{l_x} (\cos \theta)^{l_y} P_n^{l_x + \frac{1}{2}, l_y + \frac{1}{2}}(\cos 2\theta) \tag{4}$$

The valence neutrons wave function is

$$\psi_{n,k}^{l_x l_y}(\rho, \theta) = R_n(\rho)\psi_k^{l_x l_y}(\theta) \tag{5}$$

$$\psi(x, y) = \psi_{n,k}^{l_x l_y}(\rho, \theta),$$

where  $L_{nlag}^5(z)$  is the associated Laguerre polynomial of the order  $nlag = 0, 1, 2, \dots$  and  $P_n^{l_x + \frac{1}{2}, l_y + \frac{1}{2}}(\cos 2\theta)$  is the Jacobi polynomial [24, 25].

Total Hamiltonian of the system is

$$\hat{H} = \hat{T} + \hat{h}_{core}(\vec{\xi}) + \hat{V}_{core-n1}(r_{core-n1}, \vec{\xi}) + \hat{V}_{core-n2}(r_{core-n2}, \vec{\xi}) + \hat{V}_{n-n}(r_{n-n}) \tag{6}$$

$$\hat{V}_{core-n}(r_{core-n}, \vec{\xi}) = \left[ \frac{-V_0}{1 + \exp\left(\frac{r_{core-n} - R(\theta, \phi)}{a}\right)} \right] \tag{7}$$

$$+ \frac{-\hbar^2}{m^2 c^2} 2(l.s) \frac{V_{s.o}}{4r_{core-n}} \frac{d}{dr_{core-n}} \left( \left[ 1 + \exp\left(\frac{r_{core-n} - R_{so}}{a_{so}}\right) \right]^{-1} \right)$$

$$V_{n-n}(r_{n-n}) = -\frac{\hbar^2}{m^2 c^2} 2(l.s) \frac{V_{s.o}}{4r_{n-n}} \frac{d}{dr_{n-n}} \left( \left[ 1 + \exp\left(\frac{r_{n-n} - R_{so}}{a_{so}}\right) \right]^{-1} \right) \tag{8}$$

with

$$R = R_0 [1 + \beta_2 Y_{20}(\theta, \phi)] \quad (9)$$

$$\langle r_m^2 \rangle^{1/2} = \frac{1}{A} \left[ A_{core} \langle r_m^2 (core) \rangle + \langle \rho^2 \rangle \right] \quad (10)$$

For more information about the formulas [26-28].

## RESULTS

The  $^{17}\text{B}$  is radioisotope with a half-life of about 5.08(5) ms and its probabilities of decay are

$\beta^-$ ,  $n$  (63.0%),

$\beta^-$  (22.1%),

$\beta^-$ ,  $2n$  (11.0%),

$\beta^-$ ,  $3n$  (3.5%) and

$\beta^-$ ,  $4n$  (0.4%).

The biggest probability is  $\beta^-$ ,  $n$  (63.0%), which has been focused in the current work. The  $^{17}\text{B}$  has two neutrons far from the rest nucleons, which be the reason for that decay. The two valence neutrons surround and move around the deformed core. The Hamiltonian of this system depended on the microscopic of the core and the clusterization of the valence neutrons. This clusterization depended on many factors; one of them is the angle ( $\theta$ ) of valence neutron position. The binding energy of the valence neutrons is calculated depending on Eq.(6).

Eq.(5) defines a wavefunction of the two valence neutrons, whereas  $\phi$  in eq. (2), describes the core wavefunction calculated by the shell model. So the wave function of the valence neutrons has been a function of the angle as appear in eq.(5), where the core is connected to the valence neutrons and deformed. In eq.(9),  $Y_{20}(\theta, \phi)$  was taken as

$$Y_{20}(\theta, \phi) = \frac{1}{4} \sqrt{\frac{5}{\pi}} (3 \cos^2(\theta) - 1)$$

Motion of the valence neutrons around the deformed core make binding energy of these neutrons diverse regarding the angle ( $\theta$ ) and also regarding the shape of deformation (prolate or oblate). In figure (2), the energy diverse from (-0.2MeV to -1.8MeV) with angle from ( $0^\circ$  to  $90^\circ$ ) that for deformation of  $\beta_2=0.7$ .

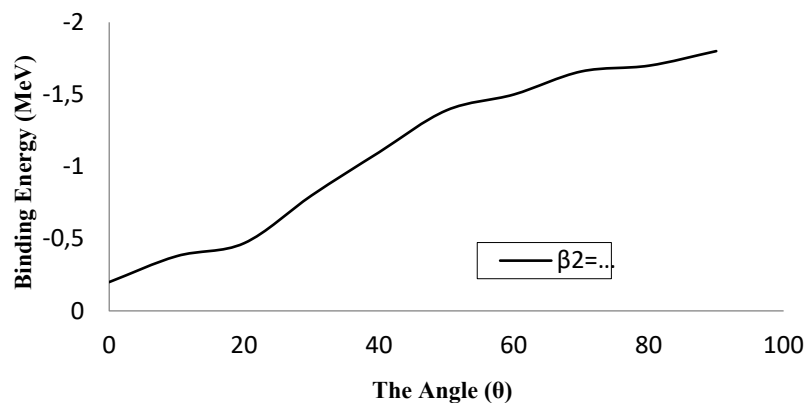


**Figure 2.** The Binding energy of the valence neutrons as function of the angle with deformation parameter ( $\beta_2=0.7$ )

The Figures (2,3,4 and 5) have considered the core is prolate and its deformation parameter  $\beta_2$  (0.7, 0.5, 0.3 and 0.1) respectively. Regarding to the structure of the shell model, the core of  $^{17}\text{B}$  (it is  $^{15}\text{B}$ ) has three protons outside the first closed shell and two neutrons outside the second closed shell. That reason to make a high influence for an electric quadrupole moment. The electric quadrupole moment of this nucleus is  $Q=Q_j+Q_c$ , it collected from  $Q_j$  that caused from the two neutrons which has been neglected in this study and  $Q_c$  of the core. In general  $Q_c \gg Q_j$  [29, 30]

$$Q_c = Q' \left[ (3\Omega^2 / 2J^2) - \frac{1}{2} \right] \quad (11)$$

Eq. (11) can drive as

$$Q_c = Q' \frac{J}{2J+3} \left[ \frac{3\Omega^2}{J(J+1)} - 1 \right] \quad (12)$$

The  $J$  is angular momentum,  $Q'$  can be equal to

$$Q' = \frac{4}{5} \delta ZR^2 \tag{13}$$

The  $\Omega$  is the projection of  $j$  and  $\delta$  has relation with the parameter  $\beta_2$  as

$$(\beta_2 = 2/3(4\pi/5)^{1/2}\delta) [28, 29].$$

From the eq. (12) and eq. (13), the proton has a high effect on deformation, so we expect the deformation parameter about 0.2 to 0.4 if it is prolate and about -0.2 to -0.4 if it is oblate. However, the experimental data is  $\beta_2=0.437$  [31]. Depending on the experimental data and from the fig. (2), the lowest value of energy is 0.3MeV in the angle ( $\theta=0$ ).

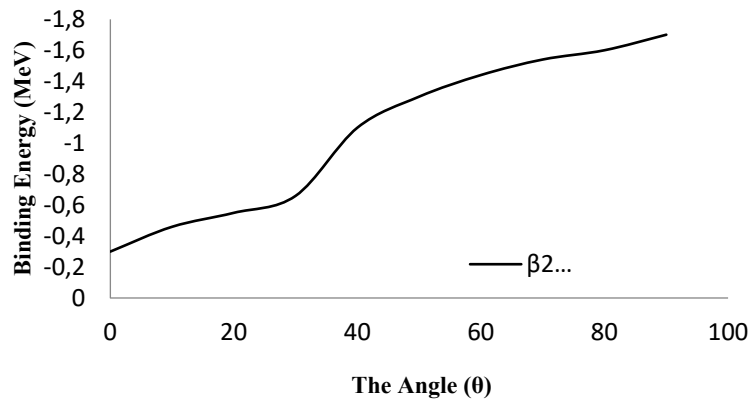


Figure 3. The Binding energy of the valence neutrons as function of the angle with deformation parameter ( $\beta_2=0.5$ )

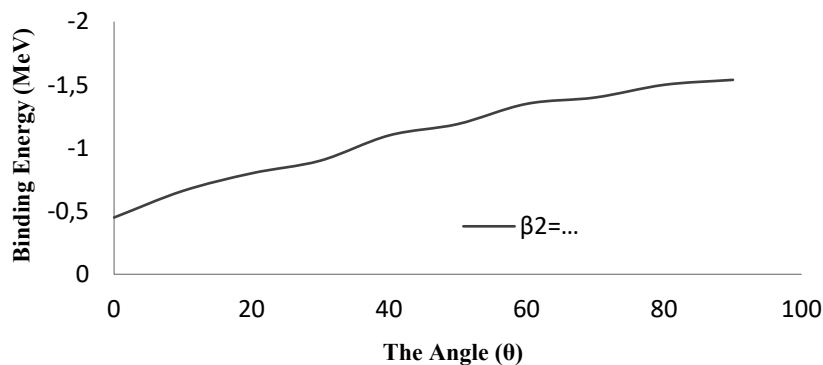


Figure 4. The Binding energy of the valence neutrons as function of the angle with deformation parameter ( $\beta_2=0.3$ )

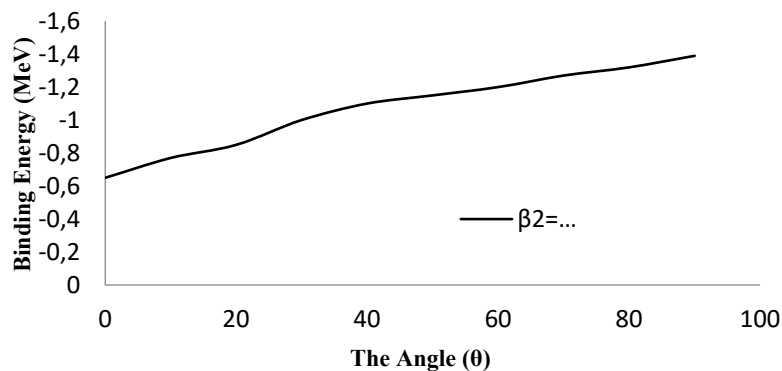


Figure 5. The Binding energy of the valence neutrons as function of the angle with deformation parameter ( $\beta_2=0.1$ )

The oblate shape has been taken into consideration. The figures (6,7,8 and 9) have considered the core is oblate and its deformation parameter  $\beta_2$  (-0.7, -0.5, -0.3, and -0.1) respectively.

The procedure applied within this work has relied on the use of influence the total angular moment, atomic number, and angle characterizes both the clusters and the parent nucleus. All possible deformation parameters and angles in clusterization channels have been studied. The point of starting is always the deformation parameter of the core. The deformation theoretical values that have been studied instead of experimental values is modified by the space of our study: if only experimental values have been used, several probable clusterization canals cannot be done because of the lack of values of deformation for both or one of the clusters.

The many energies of the neutrons regarding relative motion was calculated as seen in figures using the virtual description. The predilection of diverse cluster configurations is categorized by the reciprocal forbiddingness. Using deformation of the ground state for the parent makes all cluster configurations possible and turn out to be allowed theoretically. A clear configuration towards radioactivity (or neutron emission) may be deduced from these figures. Always keep in mind that “forbidden” in the theoretical structural analysis should mean restrained. We should expect that looks to be of certain advantage: the cluster configuration of low-lying of prolate nucleus isn't meaning the pole-to-pole; instead of both clusters are tended with regard to the axis.

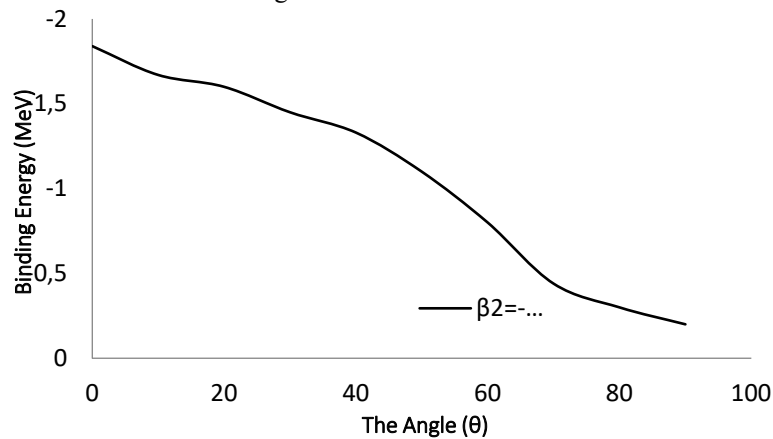


Figure 6. The Binding energy of the valence neutrons as function of the angle with deformation parameter ( $\beta_2=-0.7$ )

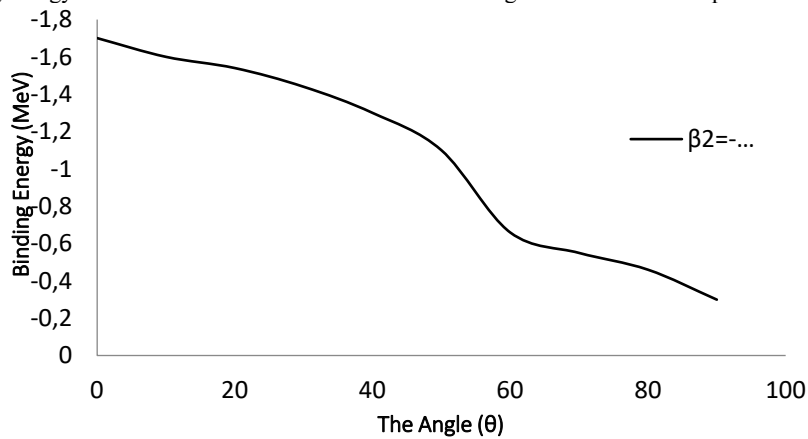


Figure 7. The Binding energy of the valence neutrons as function of the angle with deformation parameter ( $\beta_2=-0.5$ )

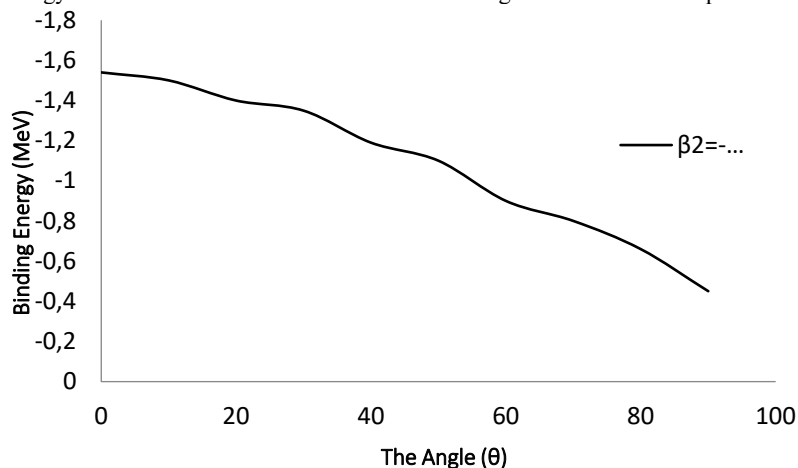
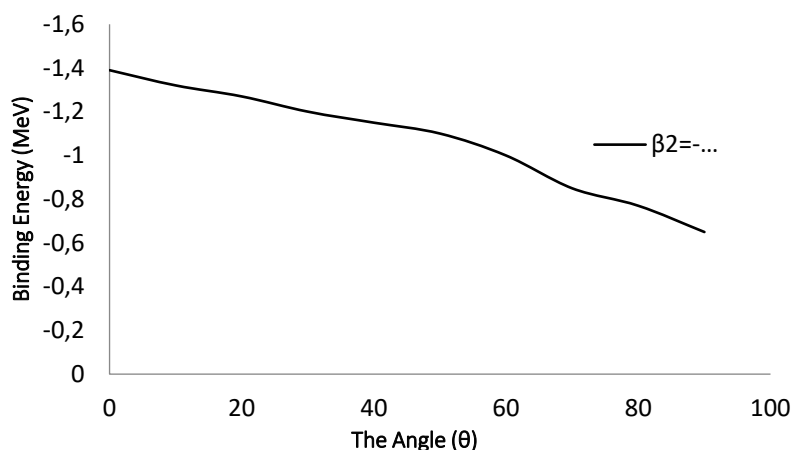


Figure 8. The Binding energy of the valence neutrons as function of the angle with deformation parameter ( $\beta_2=-0.3$ )





**Figure 9.** The Binding energy of the valence neutrons as function of the angle with deformation parameter ( $\beta_2=-0.1$ )

This clusterization configuration is of particular interest for starting point of decay or neutron emission as seen in a binary neutron emission channel. The pole-pole shapes, favored by calculation of penetrability, are highly Pauli principle forbidden as seen in results.

So they only can be a small compounds in the wave function of the ground state of the system. Also, if there are allowed clusterizations have been addressed in the case when one change the core deformation to superdeformation or hyperdeformation which connected to the valence neutrons.

The results are presented the clusters of neutrons and the core are considered to have deformation of the ground state. It is exciting to get that in these situations have allowed clusterizations also. In a superdeformed case; the allowed clusterizations connected to mostly to two particular areas wherein: (a) both neutron clusters have big prolate electric quadrupole deformation (around the region with *Zlight*,36), (b) first cluster with prolate deformation (electric quadrupole), and the second with oblate shape (around with *Zlight*,22). For the case of the hyperdeformed more channels are exposed, and from Figs. 2,3,4 and 5 and figs.6,7,8 and 9 a clear inferred to symmetric clusterization.

One of the interesting questions is if clusterization of the Halo nuclei exists in other radioactivity nuclei before the decay process. The clusterization is predicted for radioisotopes at excitation states close the relative multiple Beta decays. Actually, the main point is to determine when and where the decay starting. The position of the valence neutrons to decay or emission is our goal. However, the results determined the starting point of decay regarding energies.

The sizes of nuclei and the nucleon distributions give us the important parameters which connected extremely to the strong or weak interaction and decay. Also, the main idea of this study is to drive the clusterization of nucleons in Halo nuclei to other nuclei, which have radioactivity and large radii. The idea that Halo nuclei and radioisotopes having radii greater than those of the stable nuclei. These nuclei can be presented in a clusterization system.

From the results and regarding the decay energy of  $^{17}\text{B}$ , the figures 4, 5, 8, and 9 have been excluded. The figures 2 and 3 represent the prolate shape and the figures 6 and 7 represent the oblate shape. Regardless of the experimental deformation parameter and from equation (13), the theoretical value of deformation is around ( $\beta_2=0.5$ ). from the Figure 3, the energy is about (-0.3MeV) with angle ( $\theta=0$ ).

By normalization, the experimental data of deformation parameter has been used to get the energy, which is about (-0.387MeV).

## CONCLUSIONS

In this study, the halo structure and decay process have been investigated by clusterization configuration. The Microscopic Cluster Model (MCM) was the main tool and logical form to describe such as this system. This model gave us a wide range to take into consideration all components even freedom degrees of the core. The results obviously refer to the two considerations, first based on the angle of clusters of the microscopic cluster structure and the second on freedom degrees of the core.

The movement of the valence neutrons around the core represented various energies based on the angles. From that variance, we can determine the location of the valence neutron to emission or to decay. The deformation selection rule has a similar propensity for affecting on the energy. The core deformation parameter has high influence on the decay process. Our results clearly indicate to that the asymmetric binary microscopic cluster forms are preferred for the ground state. I can strongly say, we can expand this approach to all radio nuclei to appoint the energies and the neutron position of decay.

## ORCID IDs

Waleed S. Hwash, <https://orcid.org/0000-0002-0105-4540>

## REFERENCES

- [1] I. Tanihata, T. Kobayashi, O. Yamakawa, S. Shimoura, K. Ekuni, K. Sugimoto, N. Takahashi, et al, Phys. Lett. B, **206**, 592 (1988), [https://doi.org/10.1016/0370-2693\(88\)90702-2](https://doi.org/10.1016/0370-2693(88)90702-2)

- [2] W. Mittig, J. M. Chauvel, Z.W. Long, L. Bianchi, A. Cunsolo, B. Fernandez, A. Foti, et al, Phys. Rev. Lett. **59**, 1889 (1987), <https://doi.org/10.1103/PhysRevLett.59.1889>
- [3] M.G. Saint-Laurent, R. Anne, D. Bazin, D. Guillemaud-Mueller, U. Jahnke, Jin Gen Ming, A. C. Mueller, et al, Z. Phys. A, **332**, 457 (1989), <https://doi.org/10.1007/BF01292431>
- [4] P.G. Hansen, and B. Johnson, Europhys. Lett. **4**, 409 (1987), <https://doi.org/10.1209/0295-5075/4/4/005>
- [5] J.D. Bowman, A.M. Poskanzer, R.G. Korteling, and G.W. Butler, Phys. Rev. Lett. **31**, 614 (1973), <https://doi.org/10.1103/PhysRevLett.31.614>
- [6] J.D. Bowman, J.P. Dufour, R. Del Moral, F. Hubert, D. Jean, M.S. Pravikoff, A. Fleury, A.C. Mueller, et al, Phys. Lett. B **206**, 195 (1988), [https://doi.org/10.1016/0370-2693\(88\)91491-8](https://doi.org/10.1016/0370-2693(88)91491-8)
- [7] I. Tanihata, Nucl. Phys. A, **488**, 113 (1988), [https://doi.org/10.1016/0375-9474\(88\)90257-6](https://doi.org/10.1016/0375-9474(88)90257-6)
- [8] J.D. Bowman, J.P. Dufour, R. Del Moral, F. Hubert, D. Jean, M.S. Pravikoff, A. Fleury, A.C. Mueller, et al, Europhys. Lett. **13**, 401 (1990), <https://doi.org/10.1209/0295-5075/13/5/004>
- [9] P.G. Hansen, Nucl. Phys. A **553**, 89 (1993), [https://doi.org/10.1016/0375-9474\(93\)90617-7](https://doi.org/10.1016/0375-9474(93)90617-7)
- [10] Z. Ren, N. Li, H.Y. Zhang, and W.Q. Shen, Modern Physics Letters A, **18**, 174 (2003), <https://doi.org/10.1142/S0217732303010193>
- [11] P. Descouvemont, Nuclear Physics A, **581**, 61 (1995), [https://doi.org/10.1016/0375-9474\(94\)00461-U](https://doi.org/10.1016/0375-9474(94)00461-U)
- [12] Z. Ren and G. Xu, Phys. Lett. B, **252**, 311 (1990), [https://doi.org/10.1016/0370-2693\(90\)90542-E](https://doi.org/10.1016/0370-2693(90)90542-E)
- [13] E.K. Warburton and B.A. Brown, Phys. Rev. C, **46**, 923 (1992), <https://doi.org/10.1103/PhysRevC.46.923>
- [14] T. Suzuki, R. Kanungo, O. Bochkarev, L. Chulkov, D. Cortina, M. Fukuda, H. Geissel, et al, Nuclear Physics A, **658**, 313 (1999), [https://doi.org/10.1016/S0375-9474\(99\)00376-0](https://doi.org/10.1016/S0375-9474(99)00376-0)
- [15] Zs. Dombórádi, Z. Elekes, R. Kanungo, H. Baba, Zs. Fülöp, J. Gibelin, Á. Horváth, et al, Physics Letters B, **621**, 81(2005), <https://doi.org/10.1016/j.physletb.2005.06.031>
- [16] A. Ozawa, T. Kobayashi, H. Sato, D. Hirata, I. Tanihata, O. Yamakawa, K. Omatac, et al, Phys. Lett. B, **334**, 18 (1994), [https://doi.org/10.1016/0370-2693\(94\)90585-1](https://doi.org/10.1016/0370-2693(94)90585-1)
- [17] A. Ozawa, T. Suzuki, and I. Tanihata, Nucl. Phys. A, **693**, 32 (2001), [https://doi.org/10.1016/S0375-9474\(01\)01152-6](https://doi.org/10.1016/S0375-9474(01)01152-6)
- [18] H. Ogawa, K. Asahi, K. Sakai, T. Suzuki, H. Izumi, H. Miyoshi, M. Nagakura, et al, Phys. Rev. C, **67**, 064308 (2003), <https://doi.org/10.1103/PhysRevC.67.064308>
- [19] A. Ozawa, O. Bochkarev, L. Chulkov, D. Cortina, H. Geissel, M. Hellström, M. Ivanov, et al, Nucl. Phys. A, **691**, 599 (2001), [https://doi.org/10.1016/S0375-9474\(01\)00563-2](https://doi.org/10.1016/S0375-9474(01)00563-2)
- [20] H. Sagawa, X.R. Zhou, X.Z. Zhang, and T. Suzuki, Phys. Rev. C, **70**, 054316 (2004), <https://doi.org/10.1103/PhysRevC.70.054316>
- [21] W.S. Hwash, R. Yahaya, S. Radiman, and A.F. Ismail, Journal of the Korean physical society, **61**, 27 (2012), <https://doi.org/10.3938/jkps.61.27>
- [22] W.S. Hwash, R. Yahaya, S. Radiman, and A.F. Ismail, International Journal of Modern Physics E, **21**, (07), 1250066 (2012).
- [23] Alzahraa Yaseen A Alsajjad, Ahmed N Abdullah, Al-Nahrain Journal of Science, **22**(3), 65 (2019), <https://doi.org/10.22401/ANJS.22.3.09>
- [24] F.M. Nunes et al. Nucl. Phys. A, **609**, 43 (1996), <https://doi.org/10.1142/S0218301312500668>
- [25] T. Tarutina, I.J. Thompson, and J.A. Tostevin, Nucl. Phys. A, **733**, 53 (2004), <https://doi.org/10.1016/j.nuclphysa.2003.12.003>
- [26] W.S. Hwash, Int. J. Mod. Phys. E, **25** No. 12, 1650105 (2016), <https://doi.org/10.1142/S0218301316501056>
- [27] W.S. Hwash, Turkish Journal of Physics, **41**, 151 (2017), <https://journals.tubitak.gov.tr/physics/vol41/iss2/8/>
- [28] W.S. Hwash, R. Yahaya, and S. Radiman, Effect of core deformation on  $^{17}\text{B}$  halo nucleus, Phys. Atom. Nuclei **77**, 275–281 (2014), <https://doi.org/10.1134/S1063778814020094>
- [29] W.S. Hwash, The beta<sup>+</sup>-decay in proton halo nucleus. Rev. Cubana Fis. **38**, 108 (2021), <https://www.revistacubanadefisica.org/RCFextradata/OldFiles/2021/RCF2021v38p108.pdf>
- [30] W.E. Hornyak, *Nuclear Structure Book*, (New York) (1975).
- [31] H. Izumi, K. Asahi, H. Ueno, H. Okuno, H. Sato, K. Nagata, Y. Hori, et al, Physics Letters B, **366**, 51 (1996), [https://doi.org/10.1016/0370-2693\(95\)01312-1](https://doi.org/10.1016/0370-2693(95)01312-1)

## РІШЕННЯ РІВНЯННЯ ШРЕДІНГЕРА З ПОЛОЖЕННЯМ НЕЙТРОНІВ ХУЛЯ ДЛЯ БЕТА (В-) РОЗПАДУ ТА ЕМІСІЇ НЕЙТРОНІВ

Валід С. Хваш

*Фізичний факультет педагогічного факультету чистих наук, Університет Анбара, Анбар, Ірак*

*Школа прикладної фізики, факультет науки і техніки, Університет Кебангсаан Малайзія, 43600 Бангі, Селангор, Малайзія*

Нинішнє дослідження стосується структури  $^{17}\text{B}$ , яка була досліджена за допомогою моделі мікроскопічного кластера. Розраховано енергію зв'язку та положення нейтронів двох валентних нейтронів бета-розпаду та нейтронного випромінювання. Кластерна конфігурація ядра Halo надихнула мене розглянути, що всі радіоізотопи мають кластерну конфігурацію до процесу розпаду. Координати Якобі були використані для дослідження ядра  $^{17}\text{B}$ . Координата Якобі є дуже вдалою технікою для опису, наприклад, системи трьох тіл або структури гало.  $^{17}\text{B}$  має властивість Борромей, тому він був визначений у T-конфігурації в цих координатах. Кут на малюнку визначає кут руху нейтронів гало навколо ядра. У дослідженні деформація ядра розглядається як так що має великий вплив на зв'язування валентних нейтронів.

**Ключові слова:**  $^{17}\text{B}$ , нейтронно-галоструктура, β-розпад, нейтронна емісія, мікроскопічна кластерна модель.

## USE OF NONLINEAR OPERATORS FOR SOLVING GEOMETRIC OPTICS PROBLEMS<sup>†</sup>

 **Ilia V. Demydenko**

*Department of Applied Physics and Plasma Physics, Education and Research Institute "School of Physics and Technology"  
V. N. Karazin Kharkiv National University  
E-mail: [ilyademidenko0003@gmail.com](mailto:ilyademidenko0003@gmail.com)*

Received April 1, 2022; revised May 20, 2022; accepted May 21, 2022

The aim of this work is to develop and apply a mathematical apparatus based on nonlinear operators for solving problems of geometric optics, namely the construction of images of objects in systems of thin lenses. The problem of constructing the image of a point in a thin lens was considered, on the basis of which the concept of the lensing operator was defined. The mathematical properties of the operator were investigated. The model problem of constructing an image in thin lenses folded together was investigated, on the basis of which it became possible to establish a physical interpretation of the previously determined properties. The problem of a system of lenses located at a distance was also considered, which resulted in the introduction of the concept of shift operator. The properties of the shift operator were studied, which together with the properties of the lens operator made it possible to determine the rules for using the created operators for solving the problems. In addition to solving the model problems, the following problems were considered: the speed of the moving point image, the magnification factor and the construction of the curve image. As an example, images of a segment and an arc of the circle were constructed. The segment was transformed into the segment, and the arc of the circle into the arc of the curve of the second order. The presented mathematical apparatus is very convenient for implementation in computer programs, as well as for the study of images of different curves.

**Keywords:** geometric optics, thin lens, nonlinear operator, lens systems.

**PACS:** 42.15.Dp, 42.30.Va

Currently, there are many different mathematical methods used to simulate the propagation of light. One of the classical methods is matrix optics [1]. Among the new methods of image modeling in lens systems are the use of ray tracing methods [2] and complex vectors [3]. Operators are also used in optics. For example, in geometric optics in the general theory of relativity bilocal operators are used [4]. The object of this work is to develop a new mathematical apparatus based on nonlinear operators, which allow to build easily images of objects in thin lens systems. In the course of the work, the following tasks were set: determination of the necessary operators and their mathematical properties; solving model problems to improve the theory; solving problems of curves images construction, etc. The idea of this work was to represent a point in the form of a radius vector and to define a reflection, i.e. an operator that transforms the radius vector of an object into the radius vector of the image. As an example, an image of the segment and an arc of the circle were constructed with a graphic demonstration of these images. The presented mathematical apparatus requires an additional study of possible areas of application, what creates some opportunities for other scientists in this area.

### RESEARCH METHODS AND PROCEDURE

#### *Lensing operator*

**Definition of the lensing operator.** Let's consider the point image, constructed using a condenser lens. We place the optical center of the thin condenser lens, whose focal length is equal to  $F$ , in the center of the coordinate system, the OX axis of which is directed along the main optical axis of the lens, and the OY axis is directed along the plane of the lens (see Fig.1). From now on we will work only in the orthonormal basis.

The position of point  $A$  will be described by the radius vector:

$$\vec{r}_A(x_A, y_A). \quad (1)$$

The lens forms an image of this point, which will be described by the radius vector:

$$\vec{r}_{A'}(x_{A'}, y_{A'}). \quad (2)$$

Since the lens converts vector  $\vec{r}_A(x_A, y_A)$  into vector  $\vec{r}_{A'}(x_{A'}, y_{A'})$ , there is an operator, which hereinafter will be called as lensing operator  $\hat{L}_+$ :

$$\vec{r}_{A'} = \hat{L}_+ \vec{r}_A. \quad (3)$$

Let's determine the expression for the lensing operator. From the formula of a thin lens we have [5]:

<sup>†</sup> Cite as: I.V. Demydenko, East Eur. J. Phys. 2, 160, 2022, <https://doi.org/10.26565/2312-4334-2022-2-20>  
© I.V. Demydenko, 2022

$$\frac{1}{F} = \frac{1}{|x_A|} + \frac{1}{|x'_A|}. \tag{4}$$

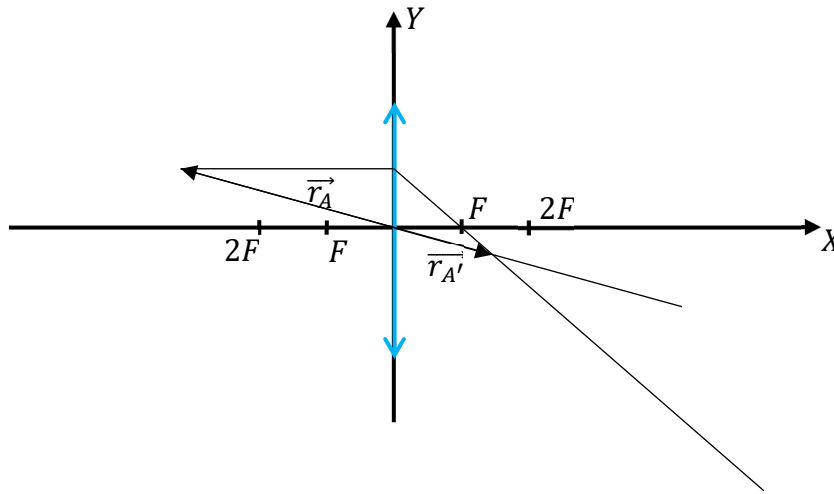


Figure 1. Image of a point in a thin lens.

Let's disclose the coordinate modules (see Fig.1):

$$\begin{cases} |x_A| = -x_A, \\ |y_A| = y_A, \\ |x'_A| = x'_A, \\ |y'_A| = -y'_A. \end{cases} \tag{5}$$

From expressions (4) and (5) we have the expression for the coordinate  $x'_A$ :

$$x'_A = x_A \frac{F}{x_A + F}. \tag{6}$$

From the similarity of triangles, we find the expression for the module of coordinate  $y'_A$ :

$$\frac{|y'_A|}{|y_A|} = \frac{|x'_A|}{|x_A|}. \tag{7}$$

From expressions (6) and 7 we get:

$$y'_A = y_A \frac{F}{x_A + F}. \tag{8}$$

Thus, the coordinates of the vector  $\vec{r}_{A'}(x'_A, y'_A)$  through the coordinates of the vector  $\vec{r}_A(x_A, y_A)$  are equal to:

$$\begin{cases} x'_A = x_A \frac{F}{x_A + F}, \\ y'_A = y_A \frac{F}{x_A + F}. \end{cases} \tag{9}$$

We can record the effect of the lensing operator as follows:

$$\hat{L}_+ \vec{r} = \frac{F}{(\vec{r}, \vec{e}_x) + F} \vec{r}. \tag{10}$$

where  $(\vec{r}, \vec{e}_x) = x, \vec{e}_x$  – orth in the direction of the OX axis.

Now, we consider an image of the point constructed using a scattering lens.

Let's place the optical center of the thin scattering lens, whose focal length is  $F$ , in the center of the coordinate system, the OX axis of which is directed along the main optical axis of the lens, and OY axis, which is perpendicular to it the main optical axis, lies in the lens plane (see Fig.2).

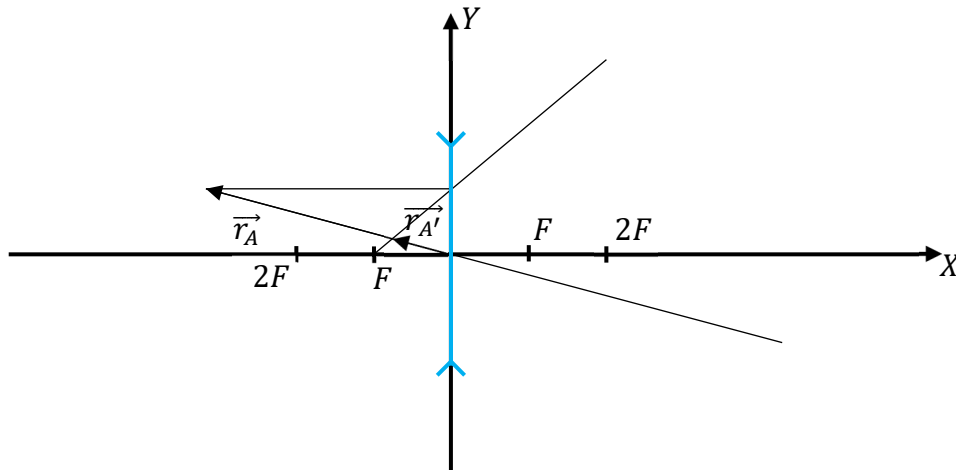


Figure 2. Image of the point in a thin scattering lens.

The position of point A will be described by the radius vector:

$$\vec{r}_A(x_A, y_A). \tag{11}$$

The lens forms an image of this point, which will be described by the radius vector:

$$\vec{r}_{A'}(x_{A'}, y_{A'}). \tag{12}$$

Since the lens converts vector  $\vec{r}_A(x_A, y_A)$  into vector  $\vec{r}_{A'}(x_{A'}, y_{A'})$ , there is an operator, which hereinafter will be called as lensing operator  $\hat{L}_-$ :

$$\vec{r}_{A'} = \hat{L}_- \vec{r}_A. \tag{13}$$

Let's determine the expression for the lensing operator  $\hat{L}_-$ . From the formula of the thin lens:

$$-\frac{1}{F} = \frac{1}{|x_A|} - \frac{1}{|x_{A'}|}. \tag{14}$$

Let's disclose the coordinate modules (see Fig.2):

$$\begin{cases} |x_A| = -x_A, \\ |y_A| = y_A, \\ |x_{A'}| = -x_{A'}, \\ |y_{A'}| = y_{A'}. \end{cases} \tag{15}$$

From expressions (14) and (15) the coordinate  $x_{A'}$  is:

$$x_{A'} = -x_A \frac{F}{x_A - F}. \tag{16}$$

Similar to the previous paragraph, we have an expression for  $y_{A'}$  coordinate:

$$y_{A'} = -y_A \frac{F}{x_A - F}. \tag{17}$$

Thus, we have the expressions of the coordinates of vector  $\vec{r}_{A'}(x_{A'}, y_{A'})$  through the coordinates of vector  $\vec{r}_A(x_A, y_A)$ :

$$\begin{cases} x_{A'} = -x_A \frac{F}{x_A - F}, \\ y_{A'} = -y_A \frac{F}{x_A - F}. \end{cases} \tag{18}$$

We can record the action of the lensing operator as follows:

$$\hat{L}_- \vec{r} = \frac{-F}{(\vec{r}, \vec{e}_x) - F} \vec{r}. \quad (19)$$

If assuming that the focal length has a sign, subject to the type of lens, one can introduce a generalized lensing operator:

$$\hat{L} \vec{r} = \frac{F}{(\vec{r}, \vec{e}_x) + F} \vec{r}. \quad (20)$$

In this case, if  $F > 0$ , then operator  $\hat{L}$  becomes operator  $\hat{L}_+$ , and if  $F < 0$ , then operator  $\hat{L}$  becomes operator  $\hat{L}_-$ .

**Properties of the lensing operator.**

1. The lensing operators are nonlinear operators.

$$\hat{L}(\alpha \vec{x} + \beta \vec{y}) \neq \alpha \hat{L} \vec{x} + \beta \hat{L} \vec{y}. \quad (21)$$

2. For different values of focal length for two operators, the equality holds:

$$[\hat{L}_1, \hat{L}_2] = 0. \quad (22)$$

Let's prove the commutativity of the lensing operators corresponding to different lenses.

$$\begin{aligned} \hat{L}_1 \hat{L}_2 \vec{r} &= \hat{L}_1 \left( \frac{F_2}{(\vec{r}, \vec{e}_x) + F_2} \vec{r} \right) = \frac{F_1}{\frac{F_2}{(\vec{r}, \vec{e}_x) + F_2} (\vec{r}, \vec{e}_x) + F_1} \left( \frac{F_2}{(\vec{r}, \vec{e}_x) + F_2} \vec{r} \right) \\ &= \frac{F_1 F_2}{F_2 (\vec{r}, \vec{e}_x) + F_1 (\vec{r}, \vec{e}_x) + F_1 F_2} \vec{r}. \end{aligned} \quad (23)$$

$$\begin{aligned} \hat{L}_2 \hat{L}_1 \vec{r} &= \hat{L}_2 \left( \frac{F_1}{(\vec{r}, \vec{e}_x) + F_1} \vec{r} \right) = \frac{F_2}{\frac{F_1}{(\vec{r}, \vec{e}_x) + F_1} (\vec{r}, \vec{e}_x) + F_2} \left( \frac{F_1}{(\vec{r}, \vec{e}_x) + F_1} \vec{r} \right) \\ &= \frac{F_1 F_2}{F_2 (\vec{r}, \vec{e}_x) + F_1 (\vec{r}, \vec{e}_x) + F_1 F_2} \vec{r}. \end{aligned} \quad (24)$$

The property of the scalar product homogeneity was used here, namely:

$$\left( \frac{F}{(\vec{r}, \vec{e}_x) + F} \vec{r}, \vec{e}_x \right) = \frac{F}{(\vec{r}, \vec{e}_x) + F} (\vec{r}, \vec{e}_x). \quad (25)$$

because the expression

$$\frac{F}{(\vec{r}, \vec{e}_x) + F} \quad (26)$$

is a scalar that we can derive from the scalar product.

As one can see, expressions (23) and (24) are equal, i.e., there is such an equality here:

$$\hat{L}_1 \hat{L}_2 \vec{r} = \hat{L}_2 \hat{L}_1 \vec{r}. \quad (27)$$

And, therefore, the operator junction is equal to 0.

3. The lensing operator is nondegenerate.

Let's consider the generalized lensing operator. By definition, a nondegenerate operator is an operator, whose kernel dimension is 0. We investigate the kernel of the generalized lensing operator.

Suppose, there exists such a nonzero vector  $\vec{r}$ , where:

$$\hat{L} \vec{r} = 0. \quad (28)$$

We describe expression (28) more specifically:

$$\hat{L} \vec{r} = \frac{F}{(\vec{r}, \vec{e}_x) + F} \vec{r} = 0. \quad (29)$$

From the fact that vector  $\vec{r}$  is nonzero it follows:

$$\frac{F}{(\vec{r}, \vec{e}_x) + F} = 0. \tag{30}$$

where the focal length is a nonzero value and  $(\vec{r}, \vec{e}_x)$  is a finite value, so we have:

$$\forall \vec{r} \neq 0, \frac{F}{(\vec{r}, \vec{e}_x) + F} \neq 0. \tag{31}$$

That is

$$\forall \vec{r} \neq 0, \hat{L}\vec{r} \neq 0 \rightarrow \dim(Ker(\hat{L})) = 0. \tag{32}$$

Thus, the generalized operator is nondegenerate.

4. The lensing operator is an injection.

We prove the injectivity of the mapping. Suppose, there are two different vectors  $\vec{r}_1$  and  $\vec{r}_2$  such that  $\hat{L}\vec{r}_1 = \hat{L}\vec{r}_2$ , then we have:

$$\hat{L}\vec{r}_1 - \hat{L}\vec{r}_2 = 0. \tag{33}$$

$$\frac{F}{(\vec{r}_1, \vec{e}_x) + F} \vec{r}_1 - \frac{F}{(\vec{r}_2, \vec{e}_x) + F} \vec{r}_2 = \frac{F\vec{r}_1(\vec{r}_2, \vec{e}_x) + F^2\vec{r}_1 - F\vec{r}_2(\vec{r}_1, \vec{e}_x) - F^2\vec{r}_2}{((\vec{r}_1, \vec{e}_x) + F)((\vec{r}_2, \vec{e}_x) + F)} = 0. \tag{34}$$

$$F\vec{r}_1(\vec{r}_2, \vec{e}_x) + F^2\vec{r}_1 - F\vec{r}_2(\vec{r}_1, \vec{e}_x) - F^2\vec{r}_2 = 0. \tag{35}$$

$$(x_1x_2 - x_2x_1, y_1x_2 - y_2x_1) + F(x_1 - x_2, y_1 - y_2) = 0. \tag{36}$$

$$(F(x_1 - x_2), y_1x_2 - y_2x_1 + Fy_1 - Fy_2) = 0. \tag{37}$$

$$\begin{cases} x_1 - x_2 = 0; \\ y_1x_2 - y_2x_1 + Fy_1 - Fy_2 = 0. \end{cases} \tag{38}$$

$$y_1x_1 - y_2x_1 + Fy_1 - Fy_2 = 0. \tag{39}$$

$$x_1(y_1 - y_2) + F(y_1 - y_2) = 0. \tag{40}$$

$$(x_1 + F)(y_1 - y_2) = 0. \tag{41}$$

We have two cases. If  $y_1 - y_2 = 0$ , then our assumption is violated. There remains the case  $x_1 + F = 0$ , which does not make sense, because in this case the expression of the operator is impossible (division by 0).

This is how we proved the injectivity of the mapping.

Note:

In the course of the analysis of the effect of lensing operators, there is a problem with the fact that this type of operator gives correct results, only if the point is located to the left of the lens. This problem can be solved in two ways:

1. We consider only the images of the points located on the left for the right orientation of the basis and on the right for the left orientation of the basis<sup>1</sup>.

2. We modify the expression of the lensing operator by introducing the concept of the focal vector that will meet the following conditions:

a) For the condenser lens the focus vector is oriented in the direction from the point, whose image we construct, and for the scattering lens – in the direction of the point.

b)

$$\begin{cases} |x| = F, \\ y = 0. \end{cases} \tag{42}$$

Then, the expression for the lensing operator will have the following form:

$$\hat{L}\vec{r} = \frac{(\vec{F}, \vec{e}_x)}{(\vec{r}, \vec{e}_x) + (\vec{F}, \vec{e}_x)} \vec{r}. \tag{43}$$

And in this case, it is easy to make sure that all the properties of this operator coincide with the previously introduced lensing operator.

However, for the convenience of calculations we use the first method.

5. Inverted operators to lensing operators.

<sup>1</sup> The following wording is stricter: for any basis orientation the following condition must be met:  $(\vec{r}, \vec{e}_x) < 0$

From the injectivity of the generalized lensing operator follows the injectivity of the operators  $\hat{L}_+$  and  $\hat{L}_-$ . The fact of the lens operators' injectivity indicates the existence of inverse lens operators [6]. Let's consider  $\hat{L}_+$  and  $\hat{L}_-$ . We return to expression (23) and make the following substitutions:

$$\begin{cases} F_1 = F; \\ F_2 = -F. \end{cases} \quad (44)$$

We get such an expression:

$$\hat{L}_+ \hat{L}_- \vec{r} = \hat{L}_+ \left( \frac{-F}{(\vec{r}, \vec{e}_x) - F} \vec{r} \right) = \frac{F}{\frac{-F}{(\vec{r}, \vec{e}_x) - F} (\vec{r}, \vec{e}_x) + F} \left( \frac{-F}{(\vec{r}, \vec{e}_x) - F} \vec{r} \right) = \frac{-F^2}{-F(\vec{r}, \vec{e}_x) + F(\vec{r}, \vec{e}_x) - F^2} \vec{r} = \vec{r}. \quad (45)$$

From expression (45) it follows that

$$\hat{L}_+ \hat{L}_- \vec{r} = \vec{r}. \quad (46)$$

That is

$$\hat{L}_+ \hat{L}_- = \hat{E}. \quad (47)$$

From the above it follows that

$$\hat{L}_+^{-1} = \hat{L}_-. \quad (48)$$

Now we enter the indication:

$$\begin{cases} \hat{L}[F] = \hat{L}_+; \\ \hat{L}[-F] = \hat{L}_-. \end{cases} \quad (49)$$

From expressions (48) and (49) it follows:

$$\hat{L}[F]^{-1} = \hat{L}[-F]. \quad (50)$$

**Systems of thin centered lenses, whose optical centers coincide.** Let's consider the construction of images using the lens operators in the system of two thin lenses folded together, so that their optical centers coincide. Assume, that the construction of images in such a complex system of lenses corresponds to the consistent use of lens operators, what is described in (23).

$$\hat{L}_1 \hat{L}_2 \vec{r} = \frac{F_1 F_2}{F_2(\vec{r}, \vec{e}_x) + F_1(\vec{r}, \vec{e}_x) + F_1 F_2} \vec{r}. \quad (51)$$

Let's make some transformations:

$$\hat{L}_1 \hat{L}_2 \vec{r} = \frac{F_1 F_2}{F_2(\vec{r}, \vec{e}_x) + F_1(\vec{r}, \vec{e}_x) + F_1 F_2} \vec{r} = \frac{\frac{F_1 F_2}{F_1 + F_2}}{(\vec{r}, \vec{e}_x) + \frac{F_1 F_2}{F_1 + F_2}} \vec{r}. \quad (52)$$

We make such a replacement:

$$\frac{F_1 F_2}{F_1 + F_2} = F_3. \quad (53)$$

Or, introducing the concept of optical power of the lens  $D_i = \frac{1}{F_i}$  from (53) we obtain:

$$D_1 + D_2 = D_3. \quad (54)$$

Thus, according to (52) - (54), the sequential use of two lens operators  $\hat{L}_1$  and  $\hat{L}_2$  is equivalent to the action of one lens operator  $\hat{L}_3 = \hat{L}_1 \hat{L}_2$ . From the physical point of view, this corresponds to the fact that the image of a point in two consecutive thin lenses with optical powers  $D_1$  and  $D_2$  coincides with its image in a thin lens with optical power  $D_3 = D_1 + D_2$ .



**Physical interpretation of lensing operator properties.** In the previous section, the concept of the lensing operator – a nonlinear operator, whose action on the radius-vector of a point gives the image of this point in a thin lens with the given optical power, was determined. Basing on of the expression for this operator, some peculiar mathematical properties were identified, which require the analysis from the physical point of view, because the mathematical apparatus, created in this work, is a method of describing physical phenomena. Therefore, this section will be devoted to the interpretation of the lens operator mathematical properties from the point of view of physics.

First of all, a very interesting feature is the commutativity of lens operators corresponding to different lenses. In the previous section, it was not defined, what the consistent action of several lens operators corresponds to. As it was shown earlier, the sequential use of two (or more) lens operators corresponds to the combination of two (or more) thin lenses. From this it follows that the commutativity of the operators means that it does not matter in what order the lenses will be used.

As well, from the fact that the sequential use of operators corresponds to several thin lens folded together, it follows a very simple explanation to the fact, that the inverse lensing operator to the given one is an operator with the opposite value of the optical power. As long as the total optical power of such a system will be zero, no lensing will occur.

The injectivity of the mapping, in its turn, corresponds to the fact that two different points cannot give the same point as an image.

It is important to check the following property: if point  $B$  is an image of point  $A$ , then point  $A$  is an image of point  $B$  [5]. Suppose, we have a lens that is specified by operator  $\hat{L}$ , then, taking into account the properties of the operator, it is necessary to check the following equality:

$$\hat{L}[-F]\vec{r}' = \vec{r}. \quad (55)$$

The sign minus before focus is due to the fact that the object, whose image we are constructing, is located to the right of the lens:

$$\hat{L}[-F]\hat{L}\vec{r} = \hat{L}^{-1}\hat{L}\vec{r} = \vec{r}. \quad (56)$$

From this, it follows that the above-mentioned property is fulfilled.

### Lensing operators' group.

#### 1. Associativity.

In terms of optical power, the lens operator can be rewritten:

$$\hat{L}\vec{r} = \frac{1}{1 + D(\vec{r}, \vec{e}_x)}\vec{r}. \quad (57)$$

Let's write the operator as follows:

$$\hat{L}[D]\vec{r} \equiv \frac{1}{1 + D(\vec{r}, \vec{e}_x)}\vec{r}. \quad (58)$$

It follows from expressions (51) and (54) that a certain operator  $\hat{L}(D_1)\hat{L}(D_2)\hat{L}(D_3)$  can be written as one operator  $\hat{L}(D_1 + D_2 + D_3)$ . Thus, from the associativity of the operation of adding real numbers (which here are optical forces) follows the associativity of lensing operators.

#### 2. Lensing operators' group.

From the existence of the internal binary operation, its associativity, commutativity, the existence of a neutral and inverse element, it follows that the lensing operators form an infinite Abelian group [7]. Let's call the group of lensing operators  $G_L$ . Thus, the properties of the lensing operator can be written as follows:

- 1)  $\forall \hat{L}[D_1], \hat{L}[D_2] \in G_L \exists \hat{L}[D_1 + D_2] \in G_L: \hat{L}[D_1]\hat{L}[D_2] = \hat{L}[D_1 + D_2]$ ,
- 2)  $\forall \hat{L}[D_1], \hat{L}[D_2] \in G_L \hat{L}[D_1]\hat{L}[D_2] = \hat{L}[D_2]\hat{L}[D_1]$ ,
- 3)  $\forall \hat{L}[D_1], \hat{L}[D_2], \hat{L}[D_3] \in G_L \hat{L}[D_1](\hat{L}[D_2]\hat{L}[D_3]) = (\hat{L}[D_1]\hat{L}[D_2])\hat{L}[D_3]$ ,
- 4)  $\exists \hat{E} = \hat{L}[0] \in G_L: \forall \hat{L}[D] \in G_L \hat{E}\hat{L}[D] = \hat{L}[D]\hat{E} = \hat{L}[D]$ ,
- 5)  $\exists \hat{L}^{-1} = \hat{L}[-D] \in G_L: \forall \hat{L}[D] \in G_L \hat{L}[D]\hat{L}[-D] = \hat{E}$ .

#### 3. Generator of $G_L$ group.

As mentioned in the previous paragraph, lensing operators form an Abelian infinite group. Let's define its generator. By definition, the following operator is called as the generator (infinitesimal operator) of the s-parametric group [7]:

$$\hat{x}_i \equiv \frac{\partial g(a_1, a_2, \dots, a_s)}{\partial a_i} \Big|_{a_i=0} . \tag{59}$$

In our case, the group is one-parametric, and the parameter itself is the optical power. Let's define the generator of  $G_L$  group:

$$\hat{x}\vec{r} = \frac{\partial}{\partial D} \left( \frac{1}{1 + D(\vec{r}, \vec{e}_x)} \right) \vec{r} \Big|_{D=0} = -(\vec{r}, \vec{e}_x) \vec{r} . \tag{60}$$

Thus, any element of the  $G_L$  group in the vicinity of zero can be decomposed as follows:

$$\hat{L}[D]\vec{r} = (\hat{E} + D\hat{x})\vec{r} = \hat{E}\vec{r} - D(\vec{r}, \vec{e}_x)\vec{r} . \tag{61}$$

**Shift operator in centered thin lens systems, whose optical centers do not coincide**

**Definition of the shift operator.** Let's consider a centered system of two lenses located at distance  $d^2$ . It is necessary to identify the lensing operator of this system from the lensing operators of the specified lenses. That is, we are looking for a lens, whose optical center is located in the coordinate center, which will replace the above-mentioned lens system.

In the course of the search for a solution to this problem, it was determined that a shift operator  $\hat{S}$  must be introduced. We determine the shift operator  $\hat{S}$  using the ratio

$$\hat{L}_2 \hat{S} \hat{L}_1 \vec{r} = \hat{L} \vec{r} . \tag{62}$$

The optical power of the system of two thin lenses under research is determined as follows [5]:

$$D = D_1 + D_2 - dD_1D_2 . \tag{63}$$

From expression (63) it follows that the lens operator of this system will have the following form:

$$\hat{L}\vec{r} = \frac{F_1F_2}{F_1F_2 + (\vec{r}, \vec{e}_x)(F_1 + F_2 - d)} . \tag{64}$$

From expression (62) follows the expression for the shift operator:

$$\hat{S}\vec{r} = \hat{L}_2^{-1} \hat{L} \hat{L}_1^{-1} \vec{r} . \tag{65}$$

Let's find the analytical expression for the shift operator:

$$\hat{L}_1^{-1} \vec{r} = \frac{-F_1}{-F_1 + (\vec{r}, \vec{e}_x)} \vec{r} . \tag{66}$$

$$\hat{L} \hat{L}_1^{-1} \vec{r} = \frac{F_1F_2 \left( \frac{-F_1}{-F_1 + (\vec{r}, \vec{e}_x)} \right)}{F_1F_2 + (F_1 + F_2 - d) \frac{-F_1}{-F_1 + (\vec{r}, \vec{e}_x)} (\vec{r}, \vec{e}_x)} \vec{r} = \frac{-F_1F_2}{-F_1F_2 + (d - F_1)(\vec{r}, \vec{e}_x)} \vec{r} . \tag{67}$$

$$\hat{L}_2^{-1} \hat{L} \hat{L}_1^{-1} \vec{r} = \frac{-F_2 \frac{-F_1F_2}{-F_1F_2 + (d - F_1)(\vec{r}, \vec{e}_x)}}{-F_2 + \frac{-F_1F_2(\vec{r}, \vec{e}_x)}{-F_1F_2 + (d - F_1)(\vec{r}, \vec{e}_x)}} \vec{r} = \frac{F_1F_2}{F_1F_2 - d(\vec{r}, \vec{e}_x)} \vec{r} . \tag{68}$$

So, the expression for the shift operator can be written as follows:

$$\hat{S}\vec{r} = \frac{1}{1 - dD_1D_2(\vec{r}, \vec{e}_x)} \vec{r} . \tag{69}$$

For certainty, we will denote the shift operator as follows:

<sup>2</sup> The optical center of one of the lenses is located at the origin.

$$\hat{S}[D_1, D_2]\vec{r} \equiv \frac{1}{1 - dD_1D_2(\vec{r}, \vec{e}_x)}\vec{r}. \tag{70}$$

Then, the solution of the problem, which we formulated at the beginning of the section, will look like this:

$$\vec{r}' = \hat{L}_2\hat{S}[D_1, D_2]\hat{L}_1\vec{r}. \tag{71}$$

In this way we obtained the coordinates of the point image in the system of centered thin lenses with optical power  $D_1$  and  $D_2$ , the distance between the optical centers of which is equal to  $d$ .

The shift operator  $\hat{S}[D_1, D_2]$  together with the lens operators  $\hat{L}_1$  and  $\hat{L}_2$  of two thin lenses allows obtaining a lensing operator  $\hat{L}_2\hat{S}[D_1, D_2]\hat{L}_1$  for the system of centered lenses, which are located at a finite distance from each other.

**Shift operator properties.**

1. The shift operator is a nonlinear operator.

$$\hat{S}(\alpha\vec{x} + \beta\vec{y}) \neq \alpha\hat{S}\vec{x} + \beta\hat{S}\vec{y}. \tag{72}$$

2. The switch of the shift operator and the lensing operator is equal to 0.

Let's prove this property:

$$\hat{L}\hat{S}\vec{r} = \hat{L} \frac{1}{1 - dD_1D_2(\vec{r}, \vec{e}_x)}\vec{r} = \frac{\frac{1}{1 - dD_1D_2(\vec{r}, \vec{e}_x)}\vec{r}}{1 + D \frac{1}{1 - dD_1D_2(\vec{r}, \vec{e}_x)}(\vec{r}, \vec{e}_x)} = \frac{1}{1 - dD_1D_2(\vec{r}, \vec{e}_x) + D(\vec{r}, \vec{e}_x)}\vec{r}. \tag{73}$$

$$\hat{S}\hat{L}\vec{r} = \hat{S} \frac{1}{1 + D(\vec{r}, \vec{e}_x)}\vec{r} = \frac{\frac{1}{1 + D(\vec{r}, \vec{e}_x)}\vec{r}}{1 - dD_1D_2 \frac{1}{1 + D(\vec{r}, \vec{e}_x)}(\vec{r}, \vec{e}_x)} = \frac{1}{1 + D(\vec{r}, \vec{e}_x) - dD_1D_2(\vec{r}, \vec{e}_x)}\vec{r}. \tag{74}$$

Expressions (74) and (75) are the same, so we have:

$$[\hat{L}, \hat{S}] = 0. \tag{75}$$

3. Shift operators for different pairs of lenses are commutative.

Prove this property:

$$\begin{aligned} \hat{S}[D_1, D_2]\hat{S}[D_3, D_4]\vec{r} &= \hat{S}[D_1, D_2] \frac{1}{1 - d_2D_3D_4(\vec{r}, \vec{e}_x)}\vec{r} = \frac{\frac{1}{1 - d_2D_3D_4(\vec{r}, \vec{e}_x)}\vec{r}}{1 - d_1D_1D_2 \frac{1}{1 - d_2D_3D_4(\vec{r}, \vec{e}_x)}(\vec{r}, \vec{e}_x)} \\ &= \frac{1}{1 - d_2D_3D_4(\vec{r}, \vec{e}_x) - d_1D_1D_2(\vec{r}, \vec{e}_x)}\vec{r}. \end{aligned} \tag{76}$$

$$\begin{aligned} \hat{S}[D_3, D_4]\hat{S}[D_1, D_2]\vec{r} &= \hat{S}[D_3, D_4] \frac{1}{1 - d_1D_1D_2(\vec{r}, \vec{e}_x)}\vec{r} = \frac{\frac{1}{1 - d_1D_1D_2(\vec{r}, \vec{e}_x)}\vec{r}}{1 - d_2D_3D_4 \frac{1}{1 - d_1D_1D_2(\vec{r}, \vec{e}_x)}(\vec{r}, \vec{e}_x)} \\ &= \frac{1}{1 - d_1D_1D_2(\vec{r}, \vec{e}_x) - d_2D_3D_4(\vec{r}, \vec{e}_x)}\vec{r}. \end{aligned} \tag{77}$$

So, we have:

$$[\hat{S}(D_1, D_2), \hat{S}(D_3, D_4)] = 0. \tag{78}$$

**Rules for the use of lensing and shift operators.** In the previous paragraphs, the definition of lensing and shift operators was formulated. Now let's outline the rules for using these operators to describe the lens system.

Suppose there is a given system of lenses with optical forces  $\{D_i\}_{i=1}^N$ , which are located at distances  $\{d_i\}_{i=1}^N$  from the origin, and  $d_1 = 0$ . Then, in order to describe this system, one must use the following rules:

1. The operators must be recorded starting with the lensing operator of the first lens.
2. If there are more than two lenses, the shift operators for the following lenses must indicate the optical power of the system of lenses, which are located before the lens under consideration, but not the optical power of the previous lens.
3. Once all the operators have been identified, they can be rearranged in any order, because all of them are commutative.

## RESULTS

The lens systems, to which operators can be applied, have previously been considered as basic problems for constructing a theory. Let's consider some other possibilities of using nonlinear operators in geometric optics.

### Speed of the moving point image

Let the point, whose image we are building, moves. Then its image will also move. We find the speed of the image movement.

By definition:

$$\vec{v} = \frac{d\vec{r}}{dt}. \quad (79)$$

$$\vec{v}' = \frac{d}{dt} \vec{r}' = \frac{d}{dt} \hat{L}\vec{r}. \quad (80)$$

$$\vec{v}' = \frac{d}{dt} \left( \frac{F}{(\vec{r}, \vec{e}_x) + F} \vec{r} \right). \quad (81)$$

$$\vec{v}' = \frac{F}{(\vec{r}, \vec{e}_x) + F} \vec{v} + \frac{F(\vec{v}, \vec{e}_x)}{((\vec{r}, \vec{e}_x) + F)^2} \vec{r}. \quad (82)$$

### Construction of the curves image

Suppose, there is a curve given in a parametric form:

$$\gamma: \vec{r} = \vec{r}(x(t), y(t)), t \in [t_1, t_2]. \quad (83)$$

Consider its image in a thin lens. To build the image, we'll use the lensing operator:

$$\gamma': \vec{r}' = \hat{L}\vec{r}(x(t), y(t)), t \in [t_1, t_2]. \quad (84)$$

$$\gamma': \vec{r}' = \left( \frac{Fx(t)}{F+x(t)}, \frac{Fy(t)}{F+x(t)} \right), t \in [t_1, t_2]. \quad (85)$$

Let's consider several examples of building the curves image in a thin lens.

#### 1. Segment

Let the segment be a part of the line given by the equation:

$$y = kx + b. \quad (86)$$

We write the equation of the line in a parametric form:

$$\begin{cases} x = t, \\ y = kt + b. \end{cases} \quad (87)$$

Then, its image will have the form:

$$\gamma': \vec{r}' = \left( \frac{Ft}{F+t}, \frac{F(kt+b)}{F+t} \right). \quad (88)$$

Let's denote the parameter  $t$  through  $x$ :

$$t = \frac{Fx}{F-x}. \quad (89)$$

Substitute (87) into the expression for the image coordinate:

$$y = \frac{Fk \frac{Fx}{F-x} + Fb}{F + \frac{Fx}{F-x}}. \quad (90)$$

After simplification, we obtain that the image of the segment is a segment:

$$y = \left( k - \frac{b}{F} \right) x + b. \quad (91)$$

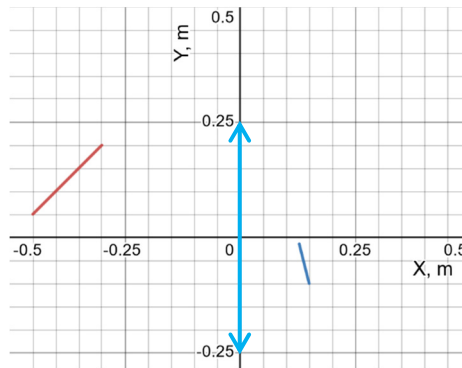


**Fig.3.** Image of a straight-line segment  $y = x + 0.5$  m when  $x \in [-0.45, -0.3]$  in a thin condenser lens with focal length  $F = 0.1$  m.

2. Arc of the circle

Consider an arc of the circle given by the equation:

$$x^2 + y^2 = R^2. \tag{92}$$

Write the equation of the circle in a parametric form:

$$\begin{cases} x = R \cos t, \\ y = R \sin t. \end{cases} \tag{93}$$

Then, the image takes the following form:

$$\gamma': \vec{r}' = \left( \frac{FR \cos t}{F + R \cos t}, \frac{FR \sin t}{F + R \cos t} \right). \tag{94}$$

Denote the trigonometric functions of the parameter  $t$  through  $x$ :

$$\cos t = \frac{Fx}{(F-x)R}, \sin t = \sqrt{1 - \frac{x^2 F^2}{(F-x)^2 R^2}}. \tag{95}$$

and substitute them into the expression for the coordinate  $y$  from (90):

$$y = \frac{FR \sqrt{1 - \frac{x^2 F^2}{(F-x)^2 R^2}}}{F + R \frac{Fx}{(F-x)R}}. \tag{96}$$

After simplification we have:

$$x^2 \left( 1 - \frac{R^2}{F^2} \right) + \frac{2R^2}{F} x + y^2 - R^2 = 0. \tag{97}$$

We obtained a second-order curve. Define its type [8]. The matrix of coefficients looks like this:

$$\begin{pmatrix} 1 - \frac{R^2}{F^2} & 0 & \frac{R^2}{F} \\ 0 & 1 & 0 \\ \frac{R^2}{F} & 0 & -R^2 \end{pmatrix}. \tag{98}$$

Let us determine the invariants of this curve. Invariants of the second order curve of the form  $a_{11}x^2 + 2a_{12}xy + a_{22}y^2 + 2a_{13}x + 2a_{23}y + a_{33} = 0$  are defined as follows [8]:

$$\begin{cases} I_1 = sp \begin{pmatrix} a_{11} & a_{12} \\ a_{12} & a_{22} \end{pmatrix}, \\ I_2 = det \begin{pmatrix} a_{11} & a_{12} \\ a_{12} & a_{22} \end{pmatrix}, \\ I_3 = det \begin{pmatrix} a_{11} & a_{12} & a_{13} \\ a_{12} & a_{22} & a_{23} \\ a_{13} & a_{23} & a_{33} \end{pmatrix}. \end{cases} \tag{99}$$

For the curve under study, the invariants have the following values:

$$\begin{cases} I_1 = 2 - \frac{R^2}{F^2}, \\ I_2 = 1 - \frac{R^2}{F^2}, \\ I_3 = -R^2. \end{cases} \tag{100}$$

The type of the second-order curve depends on the value of the circle radius and the focal length of the lens.

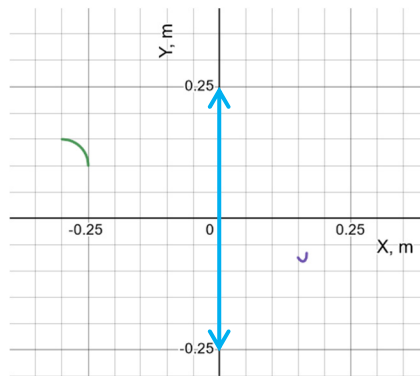


**Figure 4.** Image of the arc of the circus  $(x + 0.3 m)^2 + (y - 0.1 m)^2 = (0.05 m)^2$  with radius  $R = 0.05 m$  for angles from  $0$  to  $\frac{\pi}{2}$  in a thin condenser lens with the focal length  $F = 0.1 m$ . According to system (101) the invariants are equal to:  $I_1 = 1.75, I_2 = 0.75, I_3 = -0.0025 m^2$ . From the invariants values it follows that the image is an ellipse arc [8].

**Magnification factor**

Let’s consider how to find an expression for the coefficient of linear magnification  $\Gamma$  from the lensing operator. By definition, the coefficient of linear magnification is the ratio of the height of the image to the height of the object [5]:

$$\Gamma = \frac{|(\vec{r}', \vec{e}_y)|}{|(\vec{r}, \vec{e}_y)|}. \tag{101}$$

Let's describe it in more detail:

$$\Gamma = \frac{|(\hat{L}\vec{r}, \vec{e}_y)|}{|(\vec{r}, \vec{e}_y)|} = \left| \frac{F}{F + (\vec{r}, \vec{e}_x)} \right| |(\vec{r}, \vec{e}_y)|. \tag{102}$$

Therefore, the magnification factor can be determined as follows:

$$\Gamma = \left| \frac{F}{F + (\vec{r}, \vec{e}_x)} \right|. \tag{103}$$

**CONCLUSION**

The concept of lensing operator was introduced in the paper, its properties were investigated. A model problem of a centered system of folded thin lenses was solved, what helped to establish a physical interpretation of the properties of the lensing operator. The concept of shift operator was also introduced, what allowed considering the centered systems of thin lenses located at a certain distance, its properties were also investigated. Using the lens operator several problems were investigated, namely the speed of the moving point image, the coefficient of linear magnification of the lens and building the curves images. To solve the last problem, the general formula for the image of the curve, given in parametric form, was derived, and two examples were considered, i.e. the image of a segment and the arc of the circle in a thin lens.

ORCID ID

 Iliia Demydenko, <https://orcid.org/0000-0002-6260-0314>

Acknowledgements

Author is grateful to O. V. Gapon, Senior Lecturer of the Department of Applied Physics and Plasma Physics, V. N. Karazin Kharkiv National University, for assistance in the course of the work and evaluation of its results.

REFERENCES

- [1] B.E.A. Saleh, and M.C. Teich, *Fundamentals of photonics*, 2nd ed. (John Wiley & Sons, Inc., Hoboken, New Jersey, 2007), pp. 24-34.
- [2] N.J.G. Fonseca, Q. Liao, and O. Quevedo-Teruel, *IEEE Transactions on Antennas and Propagation*, **68**(5), 3410 (2020), <https://ieeexplore.ieee.org/abstract/document/8954908>.
- [3] C. He, J. Chang, J. Q. Hu, et al. *Nat. Commun.* **10**, 4264 (2019), <https://doi.org/10.1038/s41467-019-12286-3>
- [4] M. Grasso, M. Korzyński, and J. Serbenta, *Physical Review D*, **99**, (2019), <https://doi.org/10.1103/PhysRevD.99.064038>
- [5] D.V. Sivuhin, *Общий курс физики том 4: Оптика [General physics course Volume 4: Optics]*, 3rd ed. (Fizmatlit, Moscow, 2005), pp. 9-89. (in Russian)
- [6] A.N. Kolmogorov, and S.V. Fomin, *Элементы теории функций и функциональный анализ [Elements of the theory of functions and functional analysis]*, 4th ed. (Nauka, Moscow, 1976), pp. 16-21. (in Russian)
- [7] P. Ramond, *Group Theory: A Physicist's Survey*, 1st ed. (Cambridge University Press, Cambridge, 2010)
- [8] V.A. Il'in, and E.G. Poznyak, *Аналитическая геометрия [Analytical geometry]*, 5th ed. (Nauka, Moscow, 1999), pp. 164-184. (in Russian)

ВИКОРИСТАННЯ НЕЛІНІЙНИХ ОПЕРАТОРІВ ДЛЯ РОЗВ'ЯЗУВАННЯ ЗАДАЧ ГЕОМЕТРИЧНОЇ ОПТИКИ

I. В. Демиденко

*Харківський національний університет ім. В. Н. Каразіна, Харків, Україна*

Метою цієї роботи є розробка та застосування математичного апарату, побудованого на нелінійних операторах, для розв'язування задач геометричної оптики, а саме побудови зображень предметів у системах тонких лінз. Було розглянуто задачу про побудову зображення точки в тонкій лінзі на основі чого було визначено поняття оператора лінзування. Були досліджені математичні властивості оператора. Було досліджено модельну задачу про побудову зображення у складених разом тонких лінзах, на основі чого стало можливо встановити фізичну інтерпретацію встановленим раніше властивостям. Також була розглянута задача про систему лінз, що розташовані на відстані, результатом чого було введення поняття оператора зсуву. Були досліджені властивості оператора зсуву, які разом із властивостями оператора лінзування дали змогу визначити правила застосування створених операторів для розв'язування задач. Окрім розв'язку модельних задач були розглянуті такі задачі: швидкість зображення рухомої точки, коефіцієнт збільшення та побудова зображення кривих. Як приклад були побудовані зображення відрізка та дуги кола. Відрізок перейшов у відрізок, а дуга кола в дугу кривої другого порядку. Представлений математичний апарат є дуже зручним для реалізації у вигляді комп'ютерних програм, а також для дослідження зображень різних кривих.

**Ключові слова:** геометрична оптика; тонка лінза; нелінійний оператор; системи лінз.

# INSTRUCTIONS FOR PREPARING MANUSCRIPT IN THE EAST EUROPEAN JOURNAL OF PHYSICS

Nikita F. Author<sup>a,\*</sup>, Peter V. Co-Author(s)<sup>b,†</sup>

<sup>a</sup>Affiliation of first author

<sup>b</sup>Affiliation of second author (if different from the first Author)

\*Corresponding Author: [corresponding\\_authors@mail.com](mailto:corresponding_authors@mail.com), <sup>a</sup>ORCID ID

<sup>†</sup>E-mail: [co\\_authors@mail.com](mailto:co_authors@mail.com), <sup>b</sup>ORCID ID

Received December 25, 2021; revised January 25, 2022 accepted February 5, 2022

Each paper must begin with an abstract. The abstract should be typed in the same manner as the body text (see below). Please note that these Instructions are typed just like the manuscripts should be. The abstract must have at least **1800 phonetic symbols (about 250-300 words)**, supplying general information about the achievements, and objectives of the paper, experimental technique, methods applied, significant results and conclusions. Page layout: the text should be printed on the paper A4 format, at least **5 pages**, with margins of: **Top - 3, Bottom, Left and Right - 2 cm**. The abstract, keywords should be presented in **English** (only for foreign authors), and **Ukrainian**.

**Keywords:** there, must, be, 5-10 keywords

**PACS:** specify PACS code(s) here

This is **Introduction** section. This paper contains instructions for preparing the manuscripts. The text should be prepared in “**doc**” or “**docx**” format.

## INSTRUCTIONS

The text should be typed as follows:

- **title:** Times New Roman, 12 pt, ALL CAPS, bold, 1 spacing, centred;
- **authors:** name, initials and family names; Times New Roman, 12 pt, bold, 1 spacing, centred;
- **affiliation(s):** Times New Roman, 9 pt, italic, 1 spacing, centred;
- **abstract:** Times New Roman, 9 pt, 1 spacing, justified;
- **body text:** Times New Roman, 10 pt, 1 spacing, justified; paragraphs in sections should be indented right (tabulated) for 0.75 cm;
- **section titles:** Times New Roman, 10 pt, bold, 1 spacing, centred, without numbering, one line should be left, blank above section title;
- **subsection titles:** Times New Roman, 10 pt, bold, 1 spacing, centred, without numbering in accordance to the section (see below), one line should be left blank above subsection title;
- **figure captions:** width of the figure should be 85 or 170 mm, Figures should be numbered (**Figure 1.**) and titled below Figures using sentence format, Times New Roman, 9 pt, 1 spacing, centred (if one line) or justified (if more than one line); one line should be left blank below figure captions;
- **table captions:** width of the table should be 85 or 170 mm, tables should be numbered (**Table 1.**) and titled above tables using sentence format, Times New Roman, 10 pt, 1 spacing, justified, Tables should be formatted with a single-line box around the outside border and single ruling lines between rows and columns; one line should be left blank below tables;
- **equations:** place equations centred, numbered in Arabic: (1), the number is aligned to the right; equations should be specially prepared in **MathType** or “**Microsoft Equation**”, Times New Roman, 10 pt, one line should be left blank below and above equation.

## Additional instructions

Numerated figures and tables should be embedded in your text and placed after they are cited. Only sharp photographs and drawings are acceptable. Letters in the figures should be 3 mm high. The figures should be presented in one of the following graphic formats: jpg, gif, pcx, bmp, tif.

## REFERENCES

List of References must contain **at least 50% of articles published over the past 5 years and no more than 20% of links to their own work**. Cite References by number in AIP style (<https://aip.scitation.org/php/authors/manuscript>). Numbering in the order of referring in the text, e.g. [1], [2-5], etc. References should be listed in numerical order of citation in the text at the end of the paper (justified), Times New Roman, 9 pt, 1 spacing:

### Journal Articles

- [1] T. Mikolajick, C. Dehm, W. Hartner, I. Kasko, M.J. Kastner, N. Nagel, M. Moert, and C. Mazure, *Microelectron. Reliab.* **41**, 947 (2001), [https://doi.org/10.1016/S0026-2714\(01\)00049-X](https://doi.org/10.1016/S0026-2714(01)00049-X).
- [2] S. Bushkova, B.K. Ostafiychuk, and O.V. Copenaiev, *Physics and Chemistry of Solid State.* **15**(1), 182 (2014), <http://page.if.ua/uploads/pcss/vol15/1501-27.pdf>. (in Ukrainian)
- [3] M. Yoshimura, E. Nakai, K. Tomioka, and T. Fukui, *Appl. Phys. Lett.* **103**, 243111 (2013), <http://dx.doi.org/10.7567/APEX.6.052301>.

### E-print Resources with Collaboration Research or Preprint

- [4] M. Aaboud et al. (ATLAS Collaboration), *Eur. Phys. J. C*, **77**, 531 (2017), <http://dx.doi.org/10.1140/epjc/s10052-017-5061-9>
- [5] Sjöstrand et al., *Comput. Phys. Commun.* **191**, 159 (2015), <https://doi.org/10.1016/j.cpc.2015.01.024>.
- [6] Boudreau, C. Escobar, J. Mueller, K. Sapp, and J. Su, (2013), <http://arxiv.org/abs/1304.5639>.

### Books

- [7] S. Inoue, and K.R. Spring, *Video Microscopy: The fundamentals*, 2nd ed. (Plenum, New York, 1997), pp. 19-24.
- [8] I. Gonsky, T.P. Maksymchuk, and M.I. Kalinsky, *Біохімія Людини [Biochemistry of Man]*, (Ukrmedknyga, Ternopil, 2002), pp. 16. (in Ukrainian)

### Edited Books

- [9] Z.C. Feng, editor, *Handbook of Zinc Oxide and Related Materials: Devices and Nano Engineering, vol. 2*, (CRC Press/Taylor & Francis, Boca Raton, FL, 2012)

### Book Chapters

- [10] P. Blaha, K. Schwarz, G.K.H. Madsen, D. Kvasnicka, and J. Luitz, in: *WIEN2K, An Augmented Plane Wave Plus Local Orbitals Program for Calculating Crystal Properties*, edited by K. Schwarz (Techn. Universität Wien, Austria, 2001).
- [11] M. Gonzalez-Leal, P. Krecmer, J. Prokop, and S.R. Elliot, in: *Photo-Induced Metastability in Amorphous Semiconductors*, edited by A.V. Kolobov (Wiley-VCH, Weinheim, 2003), pp. 338-340.
- [12] A. Kochelap, and S.I. Pekar, in: *Теорія Спонтанної і Стимульованої Хемілюмінесценції Газів [Theory of Spontaneous and Stimulated Gas Chemiluminescence]* (Naukova dumka, Kyiv, 1986), pp. 16-29. (in Russian)

### Conference or Symposium Proceedings

- [13] C. Yaakov, and R. Huque, in: *Second International Telecommunications Energy Symposium Proceedings*, edited by E. Yow (IEEE, New York, 1996), pp. 17-27.
- [14] V. Nikolsky, A.K. Sandler, and M.S. Stetsenko, in: *Автоматика-2004: Матеріали 11 Міжнародної Конференції по Автоматичному Управлінню [Automation-2004: Materials of the 11th International Conference on Automated Management]* (NUHT, Kyiv, 2004), pp. 46-48. (in Ukrainian)

### Patent

- [15] I.M. Vikulin, V.I. Irha, and M.I. Panfilov, Patent Ukraine No. 26020 (27 August 2007). (in Ukrainian)

### Thesis / Dissertation

- [16] R.E. Teodorescu, Ph.D. dissertation, The George Washington University, 2009.

### Special Notes

1. Use International System of Units (SI system). 2. It is undesirable to use acronyms in the titles. Please define the acronym on its first use in the paper. 3. Refer to isotopes as <sup>14</sup>C, <sup>3</sup>H, <sup>60</sup>Co, etc.



Наукове видання

**СХІДНО-ЄВРОПЕЙСЬКИЙ ФІЗИЧНИЙ ЖУРНАЛ**

**Номер 2, 2022**

**EAST EUROPEAN JOURNAL OF PHYSICS**

**No 2, 2022**

Збірник наукових праць  
англійською та українською мовами

Коректор – Коваленко Т.О.  
Технічний редактор – Гірник С.А.  
Комп'ютерне верстання – Гірник С.А.

Підписано до друку 30.05.2022. Формат 60×84/8. Папір офсетний.

Друк цифровий.

Ум. друк. арк. 14,7. Обл.-вид. арк. 15,3

Тираж 50 пр. Зам. № 60/2021. Ціна договірна

Видавець і виготовлювач

Харківський національний університет імені В.Н. Каразіна

61022, Харків, майдан Свободи, 4

Свідоцтво суб'єкта видавничої справи ДК № 3367 від 13.01.09

Видавництво Харківський національний університет імені В.Н. Каразіна  
тел. +380-057-705-24-32